HIGH-TEMPERATURE PIEZOELECTRIC BULK ACOUSTIC WAVE SENSORS BASED ON $Ca_3TaGa_3Si_2O_{14}$ AND $YCa_4O(BO_3)_3$ SINGLE CRYSTALS

by

Hongfei Zu

B. E., Xi'an Jiaotong University, Xi'an, 2009

M. E., Xi'an Jiaotong University, Xi'an, 2012

Submitted to the Graduate Faculty of

Swanson School of Engineering in partial fulfillment

of the requirements for the degree of

Doctor of Philosophy

University of Pittsburgh

2017

UNIVERSITY OF PITTSBURGH

SWANSON SCHOOL OF ENGINEERING

This dissertation was presented

by

Hongfei Zu

It was defended on

June 12, 2017

and approved by

Minking K. Chyu, PhD, Professor
Department of Mechanical Engineering and Materials Science

William S. Slaughter, PhD, Associate Professor
Department of Mechanical Engineering and Materials Science

Nettleship Ian, PhD, Associate Professor
Department of Mechanical Engineering and Materials Science

Dissertation Director: Qing-Ming Wang, PhD, Professor
Department of Mechanical Engineering and Materials Science

HIGH-TEMPERATURE PIEZOELECTRIC BULK ACOUSTIC WAVE SENSORS BASED ON $Ca_3TaGa_3Si_2O_{14}$ AND $YCa_4O(BO_3)_3$ SINGLE CRYSTALS

Hongfei Zu, PhD

University of Pittsburgh, 2017

In this dissertation, the basic properties and advanced sensor applications of two novel high-temperature piezoelectric single crystals-CTGS and YCOB are investigated. The real and complex dielectric, elastic, and piezoelectric constants, as well as their temperature dependence are fully characterized over the temperature range of 21 to 800°C, which not only provides the significant basic information of the crystals, but also demonstrates that they are capable of sensing at 800°C or even higher temperatures because of their stable performance and low dissipations under elevated temperatures. Through the comprehensive study of the stability, linearity, and sensitivity of the samples, CTGS Y-cut TSM resonators are considered to be the optimal choice for the high-temperature sensing applications because of their overall best performance.

Furthermore, the high-temperature temperature senor, mass sensor, and pressure sensor based on CTGS Y-cut TSM resonators are studied sequentially: the temperature sensor shows a perfect linear (R^2>0.999) relationship between the resonant frequency and the temperature up to 1000°C; the mass sensor is proved to be able to accurately monitor the mass change of micro-

and nano-scale polymer layers up to 800°C with the sensitivity of 24 Hz/μg; the test system for high-temperature pressure sensor is designed and processed, and the theoretical model is derived. The pressure sensor shows a purely linear relationship between the frequency variation and the pressure difference in the test temperature (21 to 300°C) and pressure (0 to 45 PSI) ranges. Additionally, the non-linear effects under DC bias fields and stress fields are studied and the following higher order dielectric and elastic coefficients are determined accordingly:s_{166}^{*}, s_{366}^{*}, ε_{2222}, c_{6666}^{D}, and $h_{22,66}^{*}$.

TABLE OF CONTENTS

LIST OF TABLES

LIST OF FIGURES

PREFACE

Five years ago, after I completed my master's degree in Xi'an Jiaotong University, China, I once again bid farewell to my hometown and my family, and boarded the plane to study in the United States. At that moment, my heart was full of excitement, curiosity, and a little bit of unease about the unknown future environment. But now, at this moment when I'm about to finish my dissertation and Ph.D. degree in University of Pittsburgh, I feel the joy of harvest. In these five years, there has been hard work and pleasant times, and I have gained knowledge and broadened my horizons. But the most important thing for me is the concern and help from both the new and old friends. This dissertation could not have been completed without the great support that I have received from so many people over these years. I'd like to convey my warmest thanks to all of them.

To my advisor and mentor, Professor Qing-Ming Wang. I would like to express my heartfelt thanks and the sincerest respect to Dr. Wang, who has the keen thinking, board horizons, and folksy manner. Dr. Wang has great enthusiasm for the work and great patience with the students. I thank him for introducing me into a field of research, not only a hot topic, and thank him for the guidance, encouragement and support over these years. I thank him for letting me learn how to write scientific papers, manage a lab, and get along with people around. Also, I thank him for teaching me how to live a happy life in the United States and for sparing no

effort to help me in my job searching. Without his guidance and persistent help this dissertation would not have been possible.

To my committee member, Professor Minking K. Chyu. I thank him for the advice on my research and for the recommendation letter. I also thank him for enthusiastically recommending me to the job opening and for squeezing time out of a busy schedule to participate in my defense. To my committee member, Professor William S. Slaughter. I thank him for teaching me the "Elasticity" and writing me the recommendation letter. To my committee member, Professor Nettleship Ian. I thank him for the help and suggestions on my research.

To my parents. I thank them for their unconditional and unrequited concern and love. You are always there for me and sharing all the good and bad things in my life with me. Although in the past five years we have met only for three times and have stayed together for no more than sixty days, your understanding and support for me have always been with me and encouraged me. To my two elder sisters and their families. Thank you for caring and supporting me all the time, and for taking care of our parents while I'm away from home.

To our cooperative partner, Professor Shujun Zhang. I thank him for taking the trouble to answer my questions at the beginning of my research. And I thank him for writing me the recommendation letter and introducing me as the reviewer. To our cooperative partners, Professor Yanqing Zheng and his master students Quanming Lin and Bohan Jiang. I thank them for patiently preparing samples for us and helping me to revise the manuscripts.

To my girlfriend, Xuwen Chen, who always encourages me with an optimistic attitude. She has been with me to share the joy and confront the difficulties in the life. All along, she respects and supports my decisions and makes my life more colorful. I would like to express my

deepest gratitude to her. I thank her for all the concern, encouragement, understanding, and support.

To the technical staff in NFCF, Matthew France. I thank him for training me the NFCF instruments and helping me repair our laboratory apparatus. To the staff in machine shop, James Scott Macpherson. I thank him for helping me design, improve, and process the pressure tubing used in my research.

Last, but not least, I want to thank the previous and current laboratory members: Yizhong Wang, Huiyan Wu, Qiuyan Li, Wenbin Luo, Shijing Luo, Rongjie Liang, Zheng Min, Xuande Zhang, Yongsen Rong, Xiaotian Li, Jiemin Xie, Peiyuan Xiao, Chenglong Ji, and Xueqi Li. I thank them for the help in my work and life. Special thanks go to Huiyan Wu, who came to Dr. Wang's lab and will graduate at the same time with me. I thank her for all the practical help and spiritual encouragement. I also want to thank all the good friends who helped me during this period: Xuefeng Bao, Ziyue Sun, Rongxin Zhang, Lina Xu, Teng Han, Chen Mao, Liang Chen, Bo Jiang, and Zhibo Tian.

To anyone that I forgot to mention above. Thank you as well.

1.0 INTRODUCTION

1.1 BACKGROUND

According to Cady's [1] definition, piezoelectricity is "electric polarization produced by mechanical strain in crystals belonging to certain classes, the polarization being proportional to the strain and changing sign with it". It takes a long time for human beings to discover, comprehend and make use of piezoelectricity: As early as 1703, it was found that tourmaline crystals could attract and repel hot ashes. And in 1842, Brewster observed the same phenomenon with various other kinds of crystals and introduced the name "pyroelectricity". Haüy and Becquerel did lots of experiments to determine whether electricity could be generated by pressure as well as temperature, however, their results were inconclusive [2]. In 1880, when studying the relation between pyroelectricity and crystal symmetry, the brothers Pierre and Jacques Curie discovered the phenomenon of piezoelectricity. Moreover, they predicted successfully in which types of crystals the phenomenon could be observed and along which directions the force should be applied. By applying pressure to properly cut plates, they observed the related deflections in zinc blende, sodium chlorate, boracite, tourmaline, quartz, calamine, topaz, tartaric acid, cane sugar and Rochelle salt. More importantly, they obtained the quantitative result that the generated charge was proportional to the applied pressure. Then, in 1881, W. Hankel first proposed the name "piezoelectricity", which was soon widely accepted.

The effect described above is now known as “direct piezoelectric effect”. There is also “converse (or inverse) piezoelectric effect” which is associated with the mechanical displacement generated by the applied electrical field [3]. The “converse piezoelectric effect” was first predicted by Lippmann [4] in 1881 and demonstrated by Curie brothers later. Curie brothers also pointed out that the magnitude of converse piezoelectric effect constant of quartz was the same with that of direct piezoelectric effect.

Piezoelectricity only could be observed in anisotropic dielectric materials whose structures should not possess a center of symmetry. The basic relation between piezoelectricity and the crystal symmetry was established by Voigt [5] who clearly showed in which of the 32 crystal classes piezoelectric effects might exist, and he presented which of the possible 18 piezoelectric coefficients might have non-zero values for each class [1]. Of the 32 crystal classes, 21 do not possess a center of symmetry, and 20 classes of them (the 20 classes and the related crystal systems are as following: 1, Triclinic; 2 and m, Monoclinic; 222 and mm2, Orthorhombic; 4, $\bar{4}$, 422, 4mm and $\bar{4}$2m, Tetragonal; 3, 32 and 3m, Trigonal; 6, $\bar{6}$, 622, 6mm and $\bar{6}$m2, Hexagonal; 23 and $\bar{4}$3m, Cubic) exhibit the piezoelectric effect (crystal class 432 has no center of symmetry, but its piezoelectric effect degenerates because of its high symmetry). The “crystallography applied to piezoelectric crystals” has been laid down conventionally by the IEEE [6].

Both direct and converse piezoelectric effects are widely used and a series of applications could be found in present-day devices. The success of piezoelectric materials’ applications highly results from the fact that these materials can be easily adapted to useful and reliable devices [3]. According to which type of physical effect is used, the piezoelectric devices could be divided into four general categories: generators, sensors, actuators and transducers.

Generators and sensors make use of the direct piezoelectric effect, which means that they transform the mechanical energy into electric signals, while actuators work based on the converse effect by transforming electrical energy into mechanical energy. And in transducers, both effects are utilized within the same device [7, 8]. The specific applications and the related effects are summarized in Table 1-1.

Table 1-1. Specific applications and related effects of piezoelectric materials.

Devices categories	Piezoelectric effect	Principles of the work	Specific applications
Generator	Direct	Generate voltages when mechanically activated	Spark igniter, energy harvesting, gas stove, welding equipment, etc.
Sensor	Direct	Convert a physical parameter into an electrical signal	Accelerometer, hydrophone, flaw detector, auto diagnostic, etc.
Actuator	Converse	Convert an electrical signal into a physical displacement	Ultrasonic motor, finely adjust machining tools, etc.
Transducer	Both	Convert energy between electrical and mechanical	Ultrasonic sonar devices, antenna, magnetic cartridge, etc.

This work focuses on sensor applications of high-temperature piezoelectric crystals. Here crystals mean single crystals, so the piezoelectric polycrystalline materials, like ceramics, will not be included. Compared to polycrystalline materials, piezoelectric single crystals can avoid domain-related aging behavior, while possessing high electrical resistivity, low losses and excellent thermal property stability [9]. Sensors that could function at high temperatures without failure play a significant role and are in great demand in many industrial and scientific fields. In the aircraft and aerospace industries, where high temperature actuators and sensors used for structural control and health monitoring would allow development of safer, less weight, more

fuel efficient and reliable vehicles, the high temperature sensors are urgently needed and irreplaceable [9-11]. Also, energy industry, including coal-fired electric generation plants, nuclear plants, wind power and geothermal power plants, is another beneficiary of high-temperature sensors for the health monitoring of furnace components and reactor systems [10, 12]. Furthermore, in automotive electronics and some other engine-related fields, high-temperature sensors would help to improve engine efficiency and reliability as well as reduce the maintaining cost [9, 13].

To date, extensive effort has been carried out and many kinds of piezoelectric crystal materials have been investigated for the high-temperature sensor applications. Quartz, with the α-β phase transition temperature at 573°C, is the best known and most widely used piezoelectric crystals in electronic devices, such as oscillators, resonators and filters, because of its ultralow mechanical loss (high mechanical Q_M), narrow bandwidth [9, 14]. Some quartz analogues, represented by $GaPO_4$, are reported to have higher phase transition temperatures than quartz (970°C for $GaPO_4$) while exhibiting high resistivities, low dielectric losses and high mechanical quality factors [15, 16]. Recently, langasite family crystals, especially the ordered ones, such as $Ca_3TaGa_3Si_2O_{14}$ (CTGS), have been considered one of the most promising candidates for high temperature sensors for their high piezoelectric coefficients, electromechanical coupling factors, resistivities and thermal stability of dielectric properties [17, 18]. Besides the materials mentioned above, there are many other important piezoelectric crystal materials, such as the tourmalines, lithium niobate (LN), lithium tetraborate (LTB), oxyborate crystals and PMN-PT crystals, etc. And all of them will be discussed in details later.

In this chapter, the basic parameters and properties of the piezoelectric crystals which are critical to the high temperature sensor applications will be discussed first, including the different

analyzing and calculating methods. Furthermore, various types of piezoelectric crystals which are used for high-temperature sensors will be overviewed, together with the preparation methods, structures, properties, applications and so on. Finally, the specific applications of high-temperature sensors, such as the surface acoustic wave (SAW) sensors, bulk acoustic wave (BAW) sensors, accelerometers, cantilever sensors, acoustic emission sensors will be summarized by category.

1.2 BASIC PROPERTIES OF PIEZOELECTRIC CRYSTALS AND THE DETERMINATION METHODS

"Piezoelectricity", "Pyroelectricity" and "Ferroelectricity", should be distinguished firstly in order to realize and analyze material properties further. The definition of "piezoelectricity" has already been given. Pyroelectricity is the ability of the spontaneous polarization of certain solids which may be either single crystals or polycrystalline aggregates, when they are heated or cooled [19]. The solids with spontaneous polarization are pyroelectric materials and 10 of the 21 crystal classes which are without a center of symmetry may generate spontaneous polarization (the 10 classes are: 1, m, mm2, 2, 3, 3m, 4, 4mm, 6, 6mm). Ferroelectricity is defined as a physical phenomenon in which a spontaneous electric dipole moment can be reoriented from one crystallographic direction to another by an applied electric field [20]. Therefore, all ferroelectrics are pyroelectric materials while all pyroelectric crystals have piezoelectric effect, not vice versa [8, 21]. Some relevant properties and parameters will be discussed later in details.

1.2.1 Dielectric, elastic, and piezoelectric constants

The dielectric, elastic and piezoelectric constants are the most important parameters for the piezoelectric crystals and should be taken into serious consideration when choosing proper crystals for sensor fabrication. In this section, the linear piezoelectricity, which means the dielectric, elastic and piezoelectric coefficients are treated as constants independent of the magnitude and frequency of applied mechanical stresses and electric field will be adopted [6].

1.2.1.1 Dielectric constant

A dielectric material is an electrical insulator which can be polarized by an external electric field. It has the ability to store energy in response to the applied field. The electric susceptibility χ_e (dimensionless) reflects how easily the dielectric material polarizes under the electric field:

$$P_i = \varepsilon_0 \chi_{eij} E_j \quad \textbf{(1-1)}$$

where P (C/m^2) is the polarization density, E (V/m) is the electric field, and ε_0 (=8.85×10^{-12} F/m) is the electric permittivity of free space. In the case of a vacuum, χ_e=0. The electric displacement D (C/m^2) is related to the polarization density P by

$$D_i = \varepsilon_0 E_j + P_i = \varepsilon_0 (1 + \chi_{eij}) E_j = \varepsilon_0 \varepsilon_{rij} E_j = \varepsilon_{ij} E_j \quad \textbf{(1-2)}$$

where ε_r (dimensionless) is the relative permittivity (or dielectric constant), which is the ratio of the electrical energy stored in a certain material and in vacuum by the same applied voltage; ε (F/m) is the permittivity, which is a quantity measuring the ability of a substance to store electrical energy under an electric field [22]. ε_r and ε are the most commonly used parameters to describe the dielectric properties of materials, but in a few cases, the dielectric impermeability β (m/F) is employed [23].

The dielectric constant ε_r differs a lot among different crystals, e.g., it is 4.65 for quartz [24] while it could be as high as 8783 for PMN-30%PT [25]. For sensors, a large dielectric constant is desirable to overcome the losses associated with the electrical circuit, however, it leads to the decrease of piezoelectric voltage coefficient [9, 26]. Thus, for specific applications, comprehensive consideration should be taken. The temperature dependence of the dielectric constant for non-ferroelectric piezoelectric crystals is dominated by three factors: a direct volume expansion effect, the influences of volume expansion and of temperature on polarizability, which follows the Clausius-Mosotti equation [27]:

$$\frac{\varepsilon-1}{\varepsilon+2}=\frac{4\pi\alpha_m}{3V} \quad \textbf{(1-3)}$$

where α_m is the polarizability of a macroscopic small sphere with a volume *V*, which sphere is large in comparison with the lattice dimensions. The differentiation of (1-3) with respect to temperature shows that the temperature coefficient of dielectric permittivity could be evaluated by the following equation:

$$TC\varepsilon=\frac{(\varepsilon-1)(\varepsilon+2)}{\varepsilon}(A+B+C)+0.05\tan\delta \quad \textbf{(1-4)}$$

where *(A+B)*, *C* and *tanδ* are the effective volume expansion, temperature dependence of polarizability of the intrinsic ions and electrons, and dielectric loss related to inhomogeneity, respectively. For ferroelectric crystals, some others factors, such as the phase transitions, polarization rotation, and domain wall mobility, play a dominant role [9].

1.2.1.2 Elastic constant

The stresses applied on any elementary cube of material whose edges are along the three orthogonal axes x, y and z (right-handed orthogonal coordinate system, also could be denoted as

axes 1, 2 and 3, respectively) can be decomposed into stresses exerted on each face [28]. And, the stresses could be denoted as T_{ij} (N/m^2, i = 1, 2, 3; j = 1, 2, 3), where the subscript i designates the direction of the stress component and j denotes the face of the cubic normal to the axis of j. According to the balance of moment, it could be known that:

$$T_{ij} = T_{ji} \tag{1-5}$$

And there is a short-hand method for reducing the number of indices in the stress tensor. The reduced indices 1 to 6, correspond to the tensor indices if we replace: 11 by 1, 22 by 2, 33 by 3, 23 by 4, 13 by 5 and 12 by 6.

$$\begin{bmatrix} T_{11} & T_{12} & T_{13} \\ T_{21} & T_{22} & T_{23} \\ T_{31} & T_{32} & T_{33} \end{bmatrix} = \begin{bmatrix} T_1 & T_6 & T_5 \\ T_6 & T_2 & T_4 \\ T_5 & T_4 & T_3 \end{bmatrix} \tag{1-6}$$

Similarly, the strain components could be expressed in the form:

$$\begin{bmatrix} S_{11} & S_{12} & S_{13} \\ S_{21} & S_{22} & S_{23} \\ S_{31} & S_{32} & S_{33} \end{bmatrix} = \begin{bmatrix} S_1 & \frac{S_6}{2} & \frac{S_5}{2} \\ \frac{S_6}{2} & S_2 & \frac{S_4}{2} \\ \frac{S_5}{2} & \frac{S_4}{2} & S_3 \end{bmatrix} \tag{1-7}$$

For small displacements, Hooke's Law illustrates that the stresses are proportional to the strains:

$$T_i = c_{ij} S_j \tag{1-8}$$

It is sometimes advantageous to express the strains in terms of the stresses:

$$S_{ji} = s_{ji} T_i \tag{1-9}$$

where c_{ij} (N/m^2) and s_{ji} (m^2/N) (i, j = 1 to 6) are elastic stiffness constant and elastic compliance constant, respectively.

For different crystals, the elastic constants vary greatly, and even for the same crystal, the values of each component could be quite different. For example, for Rochelle salt, s_{23} = -10.3 while s_{55} = 328 (pm^2/N) [28]. Therefore, the material types, orientations and vibration modes are significant factors which should be paid attention to in the sensor design. The temperature dependent elastic constants (TDEC) could be studied by the method of combining continuum elasticity theory and first principles calculations in which the strain derivatives of the Helmholtz free energy are needed and could be expressed formally as follows:

$$\begin{cases} F_1(D_1^{P,T}, C_{11}^{P,T}, \cdots, C_{ij}^{P,T}, \cdots C_{66}^{P,T}) = 0 \\ \vdots \\ F_i(D_i^{P,T}, C_{11}^{P,T}, \cdots, C_{ij}^{P,T}, \cdots C_{66}^{P,T}) = 0 \\ \vdots \\ F_{21}(D_{21}^{P,T}, \underbrace{C_{11}^{P,T}, \cdots, C_{ij}^{P,T}, \cdots C_{66}^{P,T}}_{21}) = 0 \end{cases} \quad \textbf{(1-10)}$$

where $D_1^{P,T} \cdots D_i^{P,T} \cdots\cdots D_{21}^{P,T} \cdots$ and $D_{11}^{P,T} \cdots\cdots D_{ij}^{P,T} \cdots\cdots D_{66}^{P,T} \cdots$ represent the second-order strain derivatives of the Helmholtz free energy under different deformation modes, and the elastic constants at given temperature and pressure, respectively [29, 30].

1.2.1.3 Piezoelectric constant

Piezoelectric properties are described in terms of the parameters *D* (electric displacement), *E* (electric field), *T* (stress), and *S* (strain). The electrical response due to the direct effect can be expressed in terms of stain by

$$\begin{cases} D_i = e_{ip} S_p \\ E_i = h_{ip} S_p \end{cases} \quad \textbf{(1-11)}$$

And the converse effect can be expressed by

$$\begin{cases} S_i = g_{ip} D_p \\ S_i = d_{ip} E_p \end{cases} \tag{1-12}$$

where e_{ip}, h_{ip}, g_{ip}, and d_{ip} (i = 1 to 3, p = 1 to 6) are four types of piezoelectric coefficients and their definitions are as follows [31]:

$$\begin{cases} d_{ip} = \dfrac{\partial D_i}{\partial T_p} = \dfrac{\partial S_p}{\partial E_i} (C/N) \\ g_{ip} = -\dfrac{\partial E_i}{\partial T_p} = \dfrac{\partial S_p}{\partial D_i} (m^2/C) \\ h_{ip} = -\dfrac{\partial E_i}{\partial S_p} = -\dfrac{\partial T_p}{\partial D_i} (N/C) \\ e_{ip} = \dfrac{\partial D_i}{\partial S_p} = -\dfrac{\partial T_p}{\partial E_i} (C/m^2) \end{cases} \tag{1-13}$$

Each coefficient of the four has its specific application conditions which could be known from their definitions. The most commonly used constant is d_{33}, which represents the electric displacement or field in 3 (or z) direction related to the stress or strain applied in the same direction. Similar with the elastic constants, piezoelectric constants vary largely for different crystals and components. For example, d_{11} of quartz is about -2.25 (pC/N) [28] while d_{33} of 70PMN-30PT single crystals is about 1500 [32]. Piezoelectric coefficients reflect the materials sensitivity of the piezoelectric effect. For most sensor applications, such as the pressure sensor, the piezoelectric coefficients should be sufficiently high so that the generated signal could be detected easily. The temperature dependent piezoelectric constants for many crystals have been studied, such as the Lithium Tantalate and Lithium Niobate [33], YCOB [18], and NdCOB [34]. Some materials perform a positive variation while some others possess a negative one.

1.2.1.4 Relations of the materials constant tensors

Dielectric constants relate the two first-order tensors: Electric field and electric displacement; elastic constants reflect the relations between the two second-order tensors: Stress and Strain; piezoelectric coefficients present the association of one first-order tensor: Electric field or electric displacement and one second-order tensor: Stress or Strain. Correspondingly, they are second-order, fourth-order, and third-order tensors, and generally possess 9, 81, and 27 components, respectively. And:

$$\begin{cases} \varepsilon_{ij} = \varepsilon_{ji} \\ S_{ijkl} = S_{jikl} = S_{ijlk} = S_{jilk} = S_{klij} = S_{lkij} = S_{klji} = S_{lkji} \\ d_{ijk} = d_{ikj} \end{cases} \quad \textbf{(1-14)}$$

where i, j = 1, 2, 3. Hence, for the most unsymmetrical medium (crystal class 1), the number of independent dielectric, elastic, and piezoelectric constants are 6, 21 and 18, respectively. With the improvement of the symmetry, the numbers will reduce correspondingly. Crystals with the highest symmetry (class 432, $2/m\bar{3}$, and $4/m\bar{3}2/m$) have 1, 3 and 0 components, respectively. The components for all the crystal classes could be found in Table VIII of IEEE Std 176-1987 [6].

The dielectric, elastic and piezoelectric constants are related by the constitutive equations. Depending on which two of the four parameters: *E* or *D*, *T* or *S* are considered as the independent variables, there are four types of constitutive equations [6].

1.2.1.5 Determination of the constants

The earliest method for determining the elastic and piezoelectric constants of piezoelectric materials was static measurement. However, it is seldom used now except for determining the positive sense of coordinate axes, because it is difficult to control the electrical boundary

conditions [6]. Quasistatic measurement, which is made by applying an alternating stress or electric field to the samples, is an effective improvement of static techniques, for the alternating electric signals are easier to measure and could avoid the influence of pyroelectric effects [35]. The static and quasistatic methods are useful for testing poled ferroelectric ceramics, while they are not suggested for the study of new crystals, especially the crystals with low symmetry, where a more accurate technique—dynamic method should be applied. The electrical properties of a piezoelectric vibrator are associated with the dielectric, elastic, and piezoelectric constants. Thus, by measuring the properties (resonance and anti-resonance frequencies, the capacitance, and sometimes the dissipation factor) of a specified number of crystal plates at various orientations, the constants could be obtained [6], [28], [36, 37].

The dielectric constants could be evaluated from measurements of the capacitance of the samples provided with electrodes covering the major surfaces. In order to ensure the accuracy of the measurements, they are best made at a frequency significantly lower than the lowest resonance frequency of the crystal samples ($\leqslant 0.01 \times f_r$, and the most commonly used measurement frequency is 1 kHz), in which case the dielectric permittivities are obtained at constant stress and called "free" dielectric permittivities ε_{ij}^{T}. As discussed in last part, for the most unsymmetrical crystals, there are 6 independent dielectric constants: ε_{11}^{T}, ε_{12}^{T}, ε_{13}^{T}, ε_{22}^{T}, ε_{23}^{T}, and ε_{33}^{T}. The three dielectric permittivities ε_{11}^{T}, ε_{22}^{T}, and ε_{33}^{T} could be determined directly through measuring the capacitances and the dimensions of the square samples of X-cut, Y-cut and Z-cut, respectively (the notation for designating the orientation of crystals follows the rules formulated in part 3.6 of IEEE Std 176-1987), by

$$\varepsilon_{ii}^{T} = \frac{C_{ii} \cdot t}{A}, (i = 1, 2, 3) \qquad \textbf{(1-15)}$$

where C_{ii}, t and A are the capacitance, thickness and area with electrode of the samples. The other three constants could be obtained from the rotated cut samples according to the transformation of the coordinate system (refer chapter 5 of [28]), and all the cuts and equations used for determining all the dielectric constants will be summarized later in Table 1-2. Besides the "free" dielectric permittivities ε_{ij}^{T}, there is another type of dielectric constants-"ε_{ij}^{S}", which are measured corresponding to the constant strain and called "clamped" dielectric permittivities. The relations between the two types of dielectric constants are as follows:

$$\varepsilon_{ij}^{T} - \varepsilon_{ij}^{S} = d_{iq} e_{jq} = e_{ip} S_{pq}^{E} e_{jq} \tag{1-16}$$

Hence, the "clamped" dielectric constants could be calculated from the related "free" dielectric, elastic, and piezoelectric constants (the determination of elastic and piezoelectric constants will be discussed later). Moreover, the dielectric impermeability β_{ij} can be obtained from the permittivities by

$$\beta_{ij} = \frac{(-1)^{i+j} \Delta^{i,j}}{\Delta} \tag{1-17}$$

where Δ is the determinate of the dielectric constants matrix, and $\Delta^{i,j}$ is the minor obtained by suppressing the i th row and j th column. So far, all the dielectric permitivities and impermeabilities could be determined and the results are summarized in Table 1-2.

Table 1-2. Determination of the dielectric permittivities and impermeabilities.

Dielectric Parameters	Sample-cuts	Calculation Formulas	Comment
ε_{11}^{T}	X-cut	$\varepsilon_{ii}^{T} = C_{ii} \cdot t / A$	$i = 1, 2, 3$
ε_{22}^{T}	Y-cut		
ε_{33}^{T}	Y-cut		
ε_{12}^{T}	(XYω)θ	$\varepsilon_{11}^{T'} = \varepsilon_{11}^{T}\cos^2\theta + 2\varepsilon_{12}^{T}\cos\theta\sin\theta + \varepsilon_{22}^{T}\sin^2\theta$	$\varepsilon_{ii}^{T'} = C_{ii}' \cdot t' / A'$ The sample-cuts and formulas used are not unique.
ε_{13}^{T}	(XZω)θ	$\varepsilon_{11}^{T'} = \varepsilon_{11}^{T}\cos^2\theta - 2\varepsilon_{13}^{T}\cos\theta\sin\theta + \varepsilon_{33}^{T}\sin^2\theta$	
ε_{23}^{T}	(YZω)θ	$\varepsilon_{22}^{T'} = \varepsilon_{22}^{T}\cos^2\theta + 2\varepsilon_{23}^{T}\cos\theta\sin\theta + \varepsilon_{33}^{T}\sin^2\theta$	
ε_{ij}^{S}		$\varepsilon_{ij}^{T} - \varepsilon_{ij}^{S} = d_{iq}e_{jq} = e_{ip}S_{pq}^{E}e_{jq}$	Ref [28]
β_{ij}		$\beta_{ij} = \dfrac{(-1)^{i+j}\Delta^{i,j}}{\Delta}$	$\Delta = \begin{vmatrix} \varepsilon_{11} & \varepsilon_{12} & \varepsilon_{13} \\ \varepsilon_{12} & \varepsilon_{22} & \varepsilon_{23} \\ \varepsilon_{13} & \varepsilon_{23} & \varepsilon_{33} \end{vmatrix}$ Ref [28]

In order to determine the 21 elastic constants s_{ij} and c_{ij}, the dynamic method could be applied, in which the resonance and anti-resonance frequencies are obtained from the measurement of the impedance of piezoelectric crystal vibrators first. Then, the elastic constants can be calculated from the resonance and anti-resonance frequencies together with the densities and dimensions of the vibrators. The longitudinal mode of motion is the easiest one that could be related to the fundamental elastic constants of the crystal. Flexure modes and torsional modes are another two simple modes, however, complicated plating arrangements are required to drive them, which restricts their applications [28]. With 15 independently oriented bars cut from an asymmetric material, 9 elastic compliances (s_{11}, s_{22}, s_{33}, s_{15}, s_{16}, s_{24}, s_{26}, s_{34}, and s_{35}) and 6 combinations of the remaining twelve compliances (s_{44}+2s_{23}, s_{55}+2s_{13}, s_{66}+2s_{12}, s_{14}+s_{56}, s_{25}+s_{46}, s_{36}+s_{45}) could be determined. The remaining 12 constants couldn't be obtained from the longitudinal mode vibrators, the determination of which requires other 6 independently

oriented samples of face-shear modes or thickness-shear modes [6, 28]. Table 1-3 presents the sample-cuts and formulas used to determine the elastic constants. For example, s_{11}^E can be got from the ZX-cut bar with the electrodes are at the faces which are perpendicular to the Z direction by

$$f_r = \frac{1}{2l\sqrt{\rho s_{11}^E}} \tag{1-18}$$

where f_r, l, and ρ and are the resonance frequency, length, and density of the vibrator, respectively. Here, the s_{ij}^E means the compliances are measured when the electric field is applied perpendicular to the length of the bar. And there is another type of elastic constants—s_{ij}^D, which indicates the electric field is parallel to the length. The relation between the two types of compliances is

$$\frac{s^E}{s^D} = \frac{\varepsilon^T}{\varepsilon^S} = \frac{1}{1-k^2} \tag{1-19}$$

where k is the electromechanical coupling factor, which will be discussed later. The elastic stiffness constants c_{ij} are related to s_{ij} by

$$c_{ij} = \frac{(-1)^{i+j}\Delta^{i,j}}{\Delta} \tag{1-20}$$

where Δ is the determinate of the elastic compliance constants matrix, and $\Delta^{i,j}$ is the minor obtained by suppressing the i th row and j th column. So far, all the elastic constants could be determined and the results are summarized in Table 1-3.

Table 1-3. Determination of the elastic constants.

Elastic Parameters	Sample-cuts	Calculation Formulas	Comment
s_{11}^E, s_{22}^E, s_{33}^E, s_{15}^E, s_{16}^E, s_{24}^E, s_{26}^E, s_{34}^E, s_{35}^E	15 arbitrary independent orientations	$s_{11}^{E'} = s_{11}^E l_1^4 + (2s_{12}^E + s_{66}^E) l_1^2 m_1^2 + (2s_{13}^E + s_{55}^E) l_1^2 n_1^2$ $+(2s_{14}^E + 2s_{56}^E) l_1^2 m_1 n_1 + 2s_{15}^E l_1^3 n_1 + 2s_{16}^E l_1^3 m_1 + s_{22}^E m_1^4$ $+(2s_{23}^E + s_{44}^E) m_1^2 n_1^2 + 2s_{24}^E m_1^3 n_1 + (2s_{25}^E + 2s_{46}^E) m_1^2 l_1 n_1$ $+2s_{26}^E m_1^3 l_1 + s_{33}^E n_1^4 + 2s_{34}^E n_1^3 m_1 + 2s_{35}^E n_1^3 l_1 + 2(s_{36}^E + s_{45}^E) n_1^2 l_1 m_1$	9 elastic compliances and 6 combinations could be obtained Ref [6, 28]
s_{44}^E, s_{23}^E	XY-cut or (XYt)θ	$s_{66}^{E'} = s_{44}^E$ or $s_{66}^{E'} = 4s_{22}^E m_1^2 m_2^2 + 8s_{23}^E m_1 m_2 n_1 n_2 + 4s_{24}^E m_1 m_2 (m_1 n_2 + m_2 n_1)$ $+4s_{33}^E n_1^2 n_2^2 + 4s_{34}^E n_1 n_2 (m_1 n_2 + m_2 n_1) + s_{44}^E (m_1 n_2 + m_2 n_1)^2$	The method of calculating s_{66}^E and $s_{66}^{E'}$ follows that in chapter 5 of Ref [28], l_i, m_i and n_i are direction cosines of two related coordinate system, Ref (5.65) of [28], The sample-cuts and formulas used are not unique and may not be the best choices for specific crystals
s_{55}^E, s_{13}^E	YZ-cut or (YZt)θ	$s_{66}^{E'} = s_{55}^E$ or $s_{66}^{E'} = 4s_{11}^E l_1^2 l_2^2 + 8s_{13}^E l_1 l_2 n_1 n_2 + 4s_{15}^E l_1 l_2 (l_1 n_2 + l_2 n_1)$ $+4s_{33}^E n_1^2 n_2^2 + 4s_{35}^E n_1 n_2 (l_1 n_2 + l_2 n_1) + s_{44}^E (l_1 n_2 + l_2 n_1)^2$	
s_{66}^E, s_{12}^E	ZX-cut or (ZXt)θ	$s_{66}^{E'} = s_{66}^E$ or $s_{66}^{E'} = 4s_{11}^E l_1^2 l_2^2 + 8s_{12}^E l_1 l_2 m_1 m_2 + 4s_{16}^E l_1 l_2 (l_1 m_2 + l_2 m_1)$ $+4s_{22}^E m_1^2 m_2^2 + 4s_{26}^E m_1 m_2 (l_1 m_2 + l_2 m_1) + s_{66}^E (l_1 m_2 + l_2 m_1)^2$	
s_{14}^E, s_{56}^E	(ZXl)θ	$s_{66}^{E'} = s_{55}^E (l_1 n_2 + l_2 n_1)^2 + s_{66}^E (l_1 m_2 + l_2 m_1)^2$ $+2s_{56}^E (l_1 m_2 + l_2 m_1)(l_1 n_2 + l_2 n_1)$	
s_{46}^E, s_{25}^E	(ZYl)θ	$s_{66}^{E'} = s_{44}^E (m_1 n_2 + m_2 n_1)^2 + s_{66}^E (l_1 m_2 + l_2 m_1)^2$ $+2s_{46}^E (l_1 m_2 + l_2 m_1)(m_1 n_2 + m_2 n_1)$	
s_{36}^E, s_{45}^E	(ZXlw)θφ	Equation 5.72 in Ref [28]	
s_{ij}^D		$s_{ij}^D = (1-k^2) s_{ij}^E$	Ref [28]
c_{ij}		$c_{ij} = \frac{(-1)^{i+j} \Delta^{i,j}}{\Delta}$	Ref [28]

The piezoelectric constants d_{31} could be calculated from ε_{33}^T, s_{11}^E, resonance and anti-resonance frequency by

$$d_{31} = k\sqrt{\frac{\varepsilon_{33}^T}{4\pi} s_{11}^E} \cong \frac{\pi}{2}\sqrt{\frac{\Delta f}{f_r}}\sqrt{\frac{\varepsilon_{33}^T}{4\pi} s_{11}^E} \qquad \textbf{(1-21)}$$

where

$$\Delta f = f_a - f_r \qquad \textbf{(1-22)}$$

With the same coordinate transformation method as the determination of the elastic constants, the relation between d'_{31} and the 18 piezoelectric constants could be acquired (the equation will be showed in Table 1-4). Thus, all the 18 d_{ip} could be obtained by measuring 18 crystals with independent direction cosines. It is worth mentioning that longitudinal mode vibrators are enough to determine the piezoelectric constants and the 15 sample-cuts used for calculating the elastic constants could be used here. With the dielectric constants, elastic constants and piezoelectric constants *d*, the other three types of piezoelectric constants *e*, *g* and *h* could be obtained. The formulas will also be showed in Table 1-4.

Table 1-4. Determination of the elastic constants.

Dielectric Parameters	Sample-cuts	Calculation Formulas	Comment
d_{nj}	18 arbitrary independent orientations	$d_{31}{}' = d_{11}l_3l_1^2 + d_{12}l_3m_1^2 + d_{13}l_3n_1^2 + d_{14}l_3m_1n_1 + d_{15}l_3l_1n_1 + d_{16}l_3l_1m_1 + d_{21}m_3l_1^2 + d_{22}m_3m_1^2 + d_{23}m_3n_1^2 + d_{24}m_3m_1n_1 + d_{25}m_3l_1n_1 + d_{26}m_3l_1m_1 + d_{31}n_3l_1^2 + d_{32}n_3m_1^2 + d_{33}n_3n_1^2 + d_{34}n_3m_1n_1 + d_{35}n_3l_1n_1 + d_{36}n_3l_1m_1$	l_i, m_i and n_i are direction cosines of two related coordinate system, Ref (5.65) of [28], The sample-cuts and formulas used are not unique
e_{nj}		$e_{nj} = \frac{\varepsilon^S_{mn}}{4\pi} h_{mj} = d_{ni} c^E_{ij}$	$m, n = 1, 2, 3$ $i, j = 1, 2, 3, 4, 5, 6$
g_{nj}		$g_{nj} = 4\pi\beta^T_{mn} d_{mj} = h_{ni} s^D_{ij}$	
h_{nj}		$h_{nj} = 4\pi\beta^S_{mn} e_{mj} = g_{ni} c^D_{ij}$	

Up to now, the determination of all the dielectric, elastic and piezoelectric constants have been presented. It should be noted that this is one of the general methods and the sample-cuts and equations used are not unique for the determination of the related parameters. With the increase of the crystal symmetry, the number of non-zero parameters will reduce correspondingly.

1.2.2 Other crucial parameters

1.2.2.1 Electromechanical coupling factors

The electromechanical coupling factors k_{ij} (the first subscript represents the direction of the applied electrodes and the second one denotes the direction of the applied or developed mechanical energy) are defined as "non-dimensional coefficients which characterize the efficiency of transforming the stored energy into mechanical or electric work of a particular piezoelectric material under a specific stress and electric field configuration" by IEEE Std 176-1987 [6]. The coefficients here are known as static or quasistatic material coupling factors $k_{mat}(k_{ij}^{l}, k_{ij}^{w}, k_{ij}^{t}$ or$k_p)$, for they refer to a static or quasisitatic lossless energy transformation cycle of a piezoelectric specimen [38] and could be expressed as follows:

$$k_{mat}^2 = \frac{W_c}{W} \tag{1-23}$$

where W_c and W are the converted energy and the total stored energy, respectively.

Similarly, in dynamic conditions, the coupling factors are defined as follows [38, 39]:

$$k_w^2 = \frac{E_c}{E_{tot}} \tag{1-24}$$

where E_c and E_{tot} are the converted energy and the total energy involved in the vibration cycle, respectively. And k_w is proportional to k_{mat} by

$$k_w^2 = \frac{8}{\pi^2} k_{mat}^2 \tag{1-25}$$

From the piezoelectric constitutive equation:

$$\begin{aligned} S_i &= s_{ij}^E T_j + d_{mi} E_m \\ D_m &= d_{mi} T_i + \varepsilon_{mk}^T E_k \\ (i, j &= 1, 2, \ldots 6;\ m, k = 1, 2, 3) \end{aligned} \tag{1-26}$$

The internal energy U of a piezoelectric device could be obtained:

$$\begin{aligned} U &= \int SdT + \int DdE \\ &= [\frac{1}{2} S_{ij}^{E} T_j T_i + \frac{1}{2} d_{mi} E_m T_i] + [\frac{1}{2} d_{mi} T_i E_m + \frac{1}{2} \varepsilon_{mk}^{T} E_k E_m] \end{aligned} \quad \textbf{(1-27)}$$

where, the $1/2 s_{ij}^{E} T_j T_i$, $1/2 \varepsilon_{mk}^{T} E_k E_m$, and $1/2 d_{mi} E_m T_i$ (or $1/2 d_{mi} T_i E_m$) represent the purely mechanical energy U_m, purely electrical energy U_e and the energy transduction from electrical to mechanical or *vice versa* U_{em} through the piezoelectric effect, respectively. The coupling coefficient can also be defined as

$$k^2 = \frac{U_{em}^2}{U_e U_m} \quad \textbf{(1-28)}$$

There is a very commonly used coupling factor-"effective coupling factor", which could be easily obtained from the electrical impedance

$$k_{eff}^2 = \frac{f_p^2 - f_s^2}{f_p^2} = \frac{f_a^2 - f_r^2}{f_a^2} \quad \textbf{(1-29)}$$

where f_p is the frequency of maximum resistance and f_s is the frequency of maximum conductance, and the second relation works for the lossless piezoelectric specimens.

The determination of some important static and quasistatic coupling factors are shown in Table X of IEEE Std 176-1987 [6]. The electromechanical coupling factors for different crystals have great discrepancies, e.g., they could be smaller than 1% for quartz, while for some relaxor based ferroelectric single crystals, such as $Pb(Zn_{1/3}Nb_{2/3})O_3$-$PbTiO_3$, the k_{33} is larger than 90% [40]. The coupling factors are less sensitive to temperature than the dielectric and piezoelectric constants [9, 41].

1.2.2.2 Mechanical quality factor

The mechanical quality factor (Q factor) is a dimensionless parameter which reflects a resonator's bandwidth relative to its center frequency and shows how under-damped the resonator is [42, 43]. It presents the relationship between stored and dissipated energy of an oscillatory system and could be expressed by the following equation:

$$Q = 2\pi \times \frac{Energy\ Stored}{Energy\ Dissipated\ Per\ Cycle} \tag{1-30}$$

There are two types of Q factors: electrical quality factor Q_E and mechanical quality factor Q_M. The former one is related to off resonance devices where the dielectric loss generates most of the heat, while the latter one which determines whether the peak is narrow and sharp enough is pivotal for resonance devices [9]. Q_M is more commonly used and high Q_M which means high sensing precision is desirable for sensors. It is related to the frequency by

$$Q_M = \frac{f_r}{\Delta f} = \frac{f_r}{f_2 - f_1} \tag{1-31}$$

where f_2 and f_1 are the frequencies at -3 dB of the maximum admittance. In many cases, especially for the MEMS devices, the quality factor-frequency product $Q \times f$ is used to evaluate the performance of the resonators [44, 45].

The mechanical quality factor could be as large as 10^5-10^8 for AT-cut quartz [46], while it is as small as 20 for lead metaniobate [47]. Piezoelectric crystals usually show high mechanical quality factor, but exhibit low piezoelectric coefficients and coupling factors at the same time. Therefore, for specific sensor applications, some compromise should be made. And generally, due to the damping or phonon scattering, the quality factors are found to decrease with the increasing temperature [9].

1.2.2.3 Complex dielectric, elastic, and piezoelectric constants

The methods stated in part **1.2.1.5** for determining the dielectric, elastic and piezoelectric constants are for lossless or low loss materials, such as Alpha-Quartz, lithium niobate and barium titanate single crystals. However, when they are directly applied to lossy materials, serious errors would be introduced [48-50]. From the general acoustic field equations and piezoelectric constitutive equations, Du, Wang, and Uchino deduced the impedance and admittance equations for a thin bar and a thin plate which could be used to determine the complex coefficients

$$Z(\omega)=\frac{1}{j\omega C}\left\{1-\sum_{i=1}^{3}k_i^2\frac{\tan(\omega\Lambda_i a)}{\omega\Lambda_i a}\right\} \quad \textbf{(1-32)}$$

And

$$Y(\omega)=\frac{1}{j\omega C}\left\{1+\sum_{i=1}^{3}k_i^2\frac{\tan(\omega\Lambda_i a)}{\omega\Lambda_i a}\right\} \quad \textbf{(1-33)}$$

where a is half of the thickness for a plate or half of the length for a bar, and C, k_i and Λ_i are complex constants which are known functions of the materials coefficients for a specified vibration mode as described in [50].

1.3 GENERAL SURVEY OF HIGH-TEMPERATURE PIEZOELECTRIC CRYSTALS

In this section, various high-temperature piezoelectric crystals are discussed from their structures, preparation methods, properties to the applications. This section is divided into three parts: The first part presents some classic piezoelectric crystals, which have been widely studied, however, whose temperature ranges are restricted by certain factors; the second area details three

types of new crystals which could be used up to 1000°C or more; the final section introduces some other particular piezoelectric crystals, which have specific applications.

1.3.1 Classic high-temperature piezoelectric crystals

1.3.1.1 Quartz

Quartz (silicon dioxide SiO_2) is the second most abundant mineral in the earth's crust and is the earliest and most widely used piezoelectric crystal. It undergoes the α-β phase transition at about 573 °C [51], at which temperature the α or low-temperature quartz (belongs to the trigonal crystal system) transforms into the β or high-temperature quartz (belongs to the hexagonal crystal system) and the piezoelectric constant d11 vanishes [52]. Quartz in the earth's crust is usually found in the polycrystalline state or small crystals, however, for piezoelectric applications, the large crystals reasonably free from twinning and flaws are needed. The hydrothermal synthesis method is developed and successfully used to synthesize the large quartz crystals [53] and even quartz nanocrystals [54].

Extensive studies about the properties of quartz crystals have been done [24, 28, 46, 55-59]. Quartz possesses excellent properties: high Q_M (10^5-10^8), high electrical resistivity (>10^{17} Ω·cm at room temperature) and low-temperature coefficient, which make it widely used in the control of the frequency of oscillators and very selective filters [9, 28, 60]. Different cuts of quartz crystals have their specific characteristics and applications, which are summarized in Table 1-5.

Table 1-5. Characteristics and applications of principal cuts of quartz crystals.

Sample-cuts	Characteristics	Applications	Ref
X-cut	High frequency but poor temperature coefficient	Produce ultra-sonic vibration	[28]
Y-cut	High frequency but poor temperature coefficient	Generate shear vibration	
AT and BT-cut	High frequency with zero temperature coefficient	Control of high frequency oscillator	
CT and DT-cut	zero temperature coefficient	Frequency modulated oscillator	
GT-cut	Both positive and negative temperature coefficient	Stable oscillators with little aging	
ST-cut	Narrow band	Narrow band SAW filter/resonator/oscillator	[60]
SC-cut	low phase noise and good aging characteristics	Oven-controlled crystal oscillator	
K-cut	Good 2nd order temperature coefficient	100-150 MHz fixed frequency SAW oscillator	
LST-cut	Good frequency-temperature performance	High frequency oscillator with stable frequency-temperature performance	

However, the drawbacks of quartz crystals: small dielectric (relative permittivity is about 4.65 [24]) and piezoelectric coefficients (d_{11} is about -2.25 (pC/N) [28]), low α-β phase transition temperature (573ºC) and even lower mechanical twinning temperature (300°C) restrict their applications [9].

1.3.1.2 Tourmaline

Tourmaline belongs to the trigonal crystal system, 3m crystal class and is a complex and even Byzantine mineral with the general chemical formula [61-63]

$$XY_3Z_6[T_6O_{18}][BO_3]V_3W \quad \textbf{(1-34)}$$

where

$$
\begin{aligned}
&X = \square\,(vacancy), Na, K, Ca, Pb^{2+},\\
&Y = Li, Mg, Fe^{2+}, Mn^{2+}, Cu^{2+}, Al, V^{3+}, Cr^{3+},\\
&Fe^{3+}, Mn^{3+}, Ti^{4+},\\
&Z = Mg, Fe^{2+}, Al, V^{3+}, Cr^{3+}, Fe^{3+},\\
&T = Si, B, Al,\\
&B = B,\\
&V = OH, O,\\
&W = OH, F, O.
\end{aligned}
\qquad \textbf{(1-35)}
$$

And most of the compositional variability takes place at the X, Y, Z, W and V sites. There are about 27 minerals in the tourmaline group recognized by the International Mineralogical Association. The diversity of the components results in tourmaline crystals having a variety of colors and a large range of the electrical resistivity. In the laboratories, tourmaline could grow from specific hydrothermal solutions at a range of temperatures 350-750°C depending on the solutions and pressures [64-66]. The properties of tourmaline crystals have been widely studied and some results are reported as follows: dielectric constants ε_{r11} and ε_{r33} are about 7-8 and 6, respectively [67]; elastic constants c_{11}^{E} and c_{33}^{E} are around 300 and 160-180 Gpa, respectively; piezoelectric constants e_{33} is about 30 ($\times 10^{-2}$ C·m^{-2}) [68]; pyroelectric coefficients p_3^{σ} range between 1.8 and 5.4 (μC/(m^2·K)) [69]. Moreover, there is no signature of any phase transition up to 1400 K [68], however, the resistivity limitation restricts its applied temperature range. It was found that tourmaline could be used as shock wave and blast pressure sensor up to 700°C.

1.3.1.3 Lithium niobate, lithium tantalite, and lithium tetraborate

Both Lithium Niobate ($LiNbO_3$, LN) and Lithium Tantalate ($LiTaO_3$, LT) belong to the trigonal crystal system, 3m crystal class and they are the ABO_3-type ferroelectrics with oxygen octahedral like Barium Titanate ($BaTiO_3$, BT). In addition, their crystals are colorless, insoluble

in water and organic solvents with high melting points [70]. As for Lithium Tetraborate (also named Lithium Borate, $Li_2B_4O_7$, LTB), it belongs to tetragonal system, 4mm crystal class and unlike LN and LT crystals, the LTB crystals don't display ferroelectricity. They could be grown by Czochralski, Bridgman-Stockbarger or Stepanov techniques and the growth rates depend on the methods and temperatures applied [71-75].

Table 1-6. General properties of LN, LT, and LTB crystals.

Crystals	Density (gcm^{-1})	Melting point(°C)	Curie point(°C)	$\varepsilon_{11}^T / \varepsilon_0$	$\varepsilon_{33}^T / \varepsilon_0$	s_{11}^E (pm^2/N)	s_{33}^E (pm^2/N)	d_{33} (pC/N)	Ref
LN	4.647	1255	1140	85.2	28.7	5.831	5.026	6.0	[70, 74]
LT	7.456	1650	605	53.6	43.4	4.93	4.317	5.7	[70, 74]
LTB	2.439	849	--	9.33	9.93	8.81	24.6	19.4	[73, 75]

LN and LT crystals exhibit excellent optical, piezoelectric and pyroelectric properties, and LTB crystals possess zero temperature coefficients of resonance frequency and some other superior piezoelectric properties. A selection of essential properties relative to piezoelectric applications is given in Table 1-6.

LN crystals have a broad homogeneity range with various compositions from congruent to stoichiometric and the electrical and electromechanical properties of related Z-cut and X-cut crystals have been investigated by A. Weidenfelder *et al*. [76]. Figure 1-1 shows the bulk conductivities of three types of Z-cut LN samples as a function of temperature, which illustrates that the conductivities decrease with the increase of the Li_2O concentration and they possess linear relationships with temperature from 500 to 900°C. The total conductivity is composed of the ionic conductivity and electronic conductivity, and the increase of the concentration of Li_2O will lead to the decrease of the lithium vacancy concentration, which would certainly result in the

decrease of the ionic conductivity. In the meanwhile, the electronic conductivity also shows a dependence on the lithium vacancy concentration ($\sigma_e \sim ([V_{Li'}])^n$, with n$\leqslant$0.31), which means the electronic conductivity also decreases with the increase of the concentration of Li_2O. Therefore, the total conductivity decreases with the increase of Li_2O concentration. The temperature dependent resonance frequency and the inverse *Qf* product for X-cut and Z-cut LN crystals could be found from Figure 1-2, which indicates a material dependent loss at about 700°C. Samples 1 to 3 are all Z-cut crystals with the Li_2O concentration 48.3, 49.5 and 50.0 mol.%, respectively and sample 4 is X-cut with 49.5 mol.% Li_2O concentration [76].

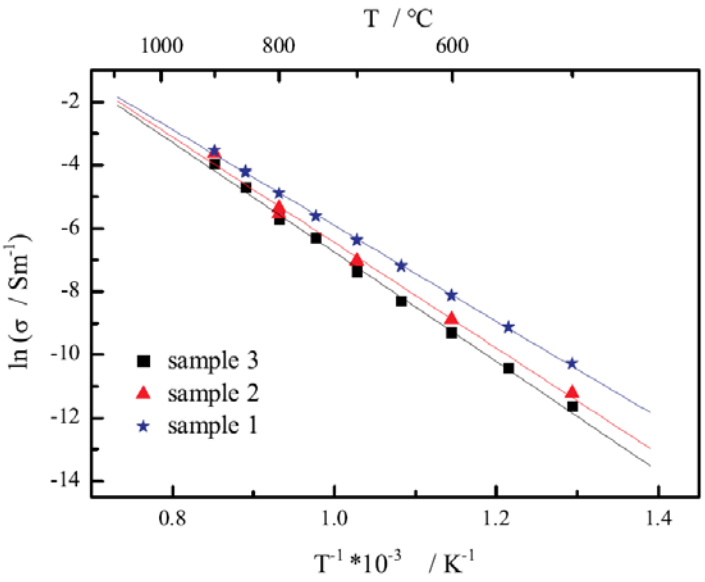

Figure 1-1. Arrhenius diagram of the total electrical conductivities of LN samples with different lithium content in the temperature range from 500 to 900 °C [76] (copyright 2012 by the ELSEVIER).

LN and LT crystals are excellent materials for mobile phones, piezoelectric sensors and optical applications. Especially, they are widely used in surface acoustic wave (SAW) devices

for their low acoustic losses. However, the temperature range of their applications is limited by their phase transitions. Compared to LN and LT, LTB crystals have no phase transition prior to their melting point and own better piezoelectric properties, but the poor levels of ionic conductivity restrict their high temperature applications [13, 70].

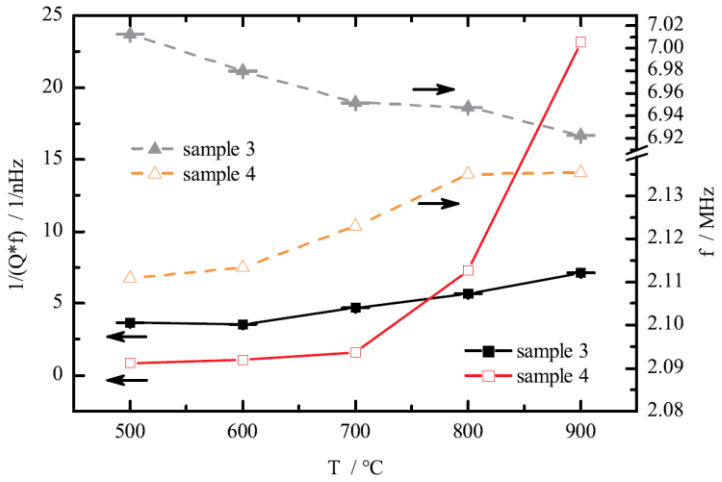

Figure 1-2. Temperature dependent frequency and inverse *Qf* product of sample 3 and 4 [76] (copyright 2012 by the ELSEVIER).

The full squares and the full triangles present sample 3; the blank squares and the blank triangles present sample 4.

1.3.2 New high-temperature piezoelectric crystals

1.3.2.1 Quartz analogs

Quartz-like materials with the structure MXO_4 (M=B, Al, Ga, Fe, Mn and X=P, As) have been extensively studied for applications supplementary to quartz [77]. Among these materials, Boron phosphate (BPO_4) and arsenate ($BAsO_4$) are “isostructural with quartz” and belong to tetragonal

crystal system; Aluminum arsenate ($AlAsO_4$) is reported in tetragonal system and in α-quartz forms; Gallium orthophosphate ($GaPO_4$), Berlinite ($AlPO_4$) and Gallium arsenate ($GaAsO_4$) are in the trigonal crystal system as α-quartz and Gallium arsenate is reported only in the α-quartz form, while Berlinite possess α-β phase transition and Gallium orthophosphate transforms into another structure similar with cristobalite at about 970°C [78].

The M-X distance, which is defined as the non-bonded radius sum, is the most important factor in controlling the structure packing [79, 80]. The *M-O-X* angle (θ) will decrease and the tilt angle (δ) will increase with the *M-O* and *X-O* distances increase, which will result in the increase of the distortion of the tetrahedral chain [81]. And the energy needed for the α-β phase transition increases with the increased distortion, and when $\theta \leqslant 136^o$ or $\delta \geqslant 22^o$ the transition will not occur, which is reflected in Figure 1-3 [79]. Also, the distortion could be indicated by the *c/a* ratio as shown in Figure 1-4. It is found that the ratio ranges from 2.20 (SiO_2) to 2.28 ($GaAsO_4$) for the quartz-like structures, and more importantly, the larger the ratio, the more the distortions [77].

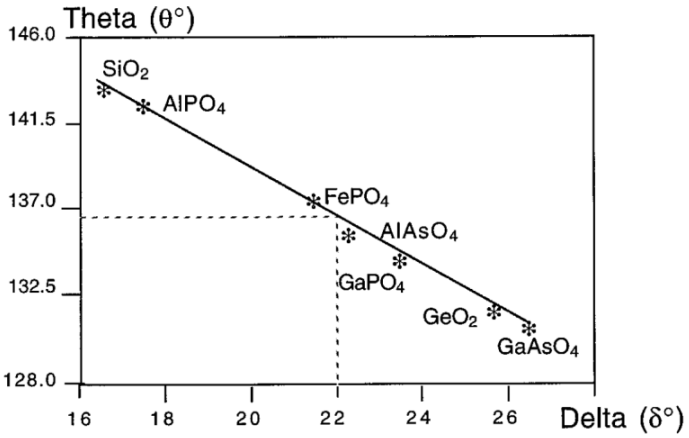

Figure 1-3. Evolution of the bridging angle *M–O–X*, θ, in terms of the mean value of the tilt angle, δ, of MO_4 and XO_4 tetrahedra [79] (copyright 1994 by the ELSEVIER).

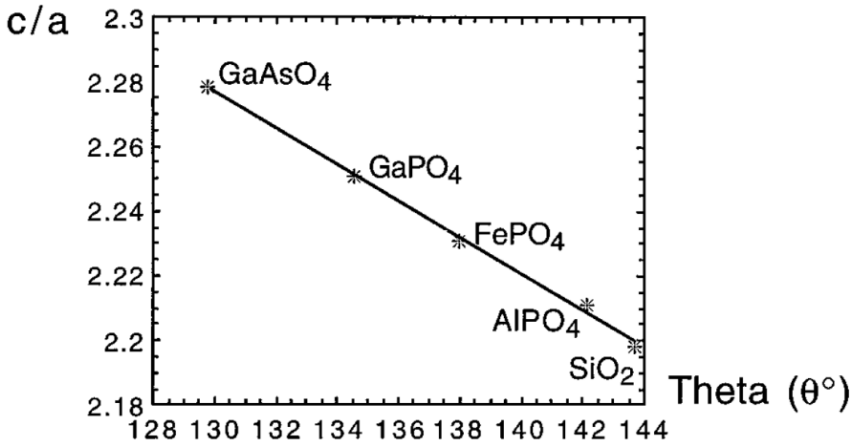

Figure 1-4. Evolution of the *c/a* ratio in terms of the bridging angle *M–O–X*, θ, [77] (copyright 1996 by the ELSEVIER).

Some significant properties for high-temperature sensor applications of SiO_2 and quartz-like crystals have been summarized by Shujun Zhang *et al*. [9]. Among the quartz analogues, $GaPO_4$, which could be grown by hydrothermal method [15, 82] or flux method [83], possesses most of the excellent performances of quartz, such as high electric resistivity (ρ>10^{17} Ω·cm at room temperature and >10^{7} Ω·cm at 900°C [84]) and high mechanical quality factor (~20000 [85]), while exhibiting stronger piezoelectric effect (d_{11} = 4.5 pC/N [86]), higher thermal stability, larger dielectric constants (ε_{r33}^{T}=6.6 [87]) and larger electromechanical coupling factor (k~16% [85]). The variations of quality factor and coupling factor of an AT-cut resonator with temperature could be seen from Figure 1-5. $GaPO_4$ crystals have been widely used for sensors up to 900°C in some harsh environments, and the temperature is restricted by the phase transition.

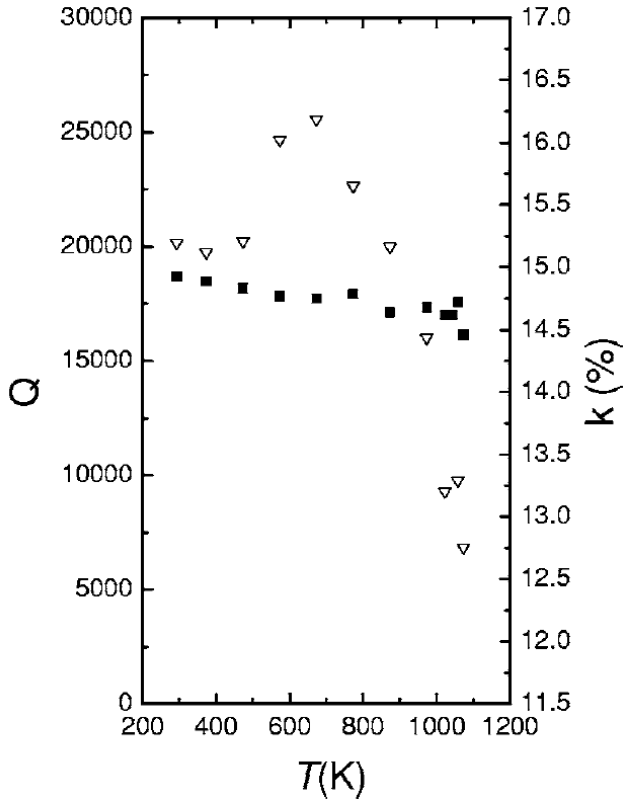

Figure 1-5. Quality factor *Q* (hollow triangles) and coupling factor *k* (solid squares) of an AT-cut $GaPO_4$ resonator as a function of temperature [85] (copyright 2006 by the APS Physics).

1.3.2.2 Langasite family crystals

Since the synthesis of $Ca_3Ga_2Ge_4O_{14}$ (CGG) in 1979 [88], which served as the starting point of the langasite ($La_3Ga_5SiO_{14}$) family crystals, the langasite family crystals have attracted great attention for their promising piezoelectric, luminescent, laser and photorefractive properties [89-91]. To date, about 180 compounds in the family are known [89, 92]. Langasite family crystals belong to the trigonal crystal system, 32 crystal class with the chemical formula as $\{E\}_3[A](F)_3<D>_2O_{14}$ (using the modified Wyckoff letter notation), whose crystal structure is schematically shown in Figure 1-6 [93]. Where, the notations {E} and [A] represent a decahedral

site coordinated by eight oxygen and an octahedral site coordinated by six oxygen, respectively. (F) and <D> represent two types of tetrahedral sites coordinated by four oxygen and the size of (F) site is larger than that of <D> site. In $La_3Ga_5SiO_{14}$ (LGS) and $La_3Ga_5GeO_{14}$ (LGG) crystals, La^{3+} occupies the {E} sites, Ga^{3+} occupies [A], (F) and part of <D> sites, and Si^{4+}/ Ge^{4+} occupies the remaining of [D] sites; while in its isomorphs, such as langanite ($La_3Ga_{5.5}Nb_{0.5}O_{14}$, LGN or LNG) and langatate ($La_3Ga_{5.5}Ta_{0.5}O_{14}$, LGT or LTG) crystals, La^{3+} occupies the {E} sites, Ga^{3+} occupies (F), <D> and half of the [A] sites, and Nb^{5+} or Ta^{5+} occupies the other half of the [A] sites [92, 93]. The langasite family crystals have been widely exploited as surface acoustic wave (SAW) and bulk acoustic wave (BAW) devices, for their brilliant properties, such as large electromechanical coupling factor, large quality factor, high resistivity, wide pass-band, temperature stability, low acoustic loss and no phase transition prior to their melting points (~1500°C) [91, 94-97]. Czochralski method [95], [98, 99] and the modified Bridgman method [100] are found to be two effective ways to grow langasite family crystals.

Many substitutions of langasite-type crystals have been investigated, such as incorporation Na^{+}, K^{+}, Ba^{2+}, Sr^{2+}, Ca^{2+}, Pb^{2+}, Bi^{3+}, Pr^{3+}, Nd^{3+} into the {E} sites and Li^{+}, Mg^{2+}, Zn^{2+}, Ga^{3+}, Al^{3+}, In^{3+}, Ti^{4+}, Zr^{4+}, Hf^{4+}, Nb^{5+}, Ta^{5+}, Sb^{5+}, Mo^{6+}, W^{6+} into [A] sites [95, 101]. Among these tries, Al^{3+} modified crystals are found to exhibit larger coupling factors (k_{12}, k_{25}, k_{26}), lower temperature dependence and higher value of piezoelectric constant d_{11} and higher electric resistivity ρ, for the smaller Al^{3+} ions replace larger Ga^{3+} ions and results in the increasing of {E}–O distance [93, 102, 103]. Figure 1-7 shows the temperature dependences of the electric resistivity of Y-cut LGS, LGAS0.9, LTG and LTGA0.5 crystals, which illustrates that compared to LGS and LTG, the LGAS0.9 and LTGA0.5 crystals exhibit high ρ values of one order of magnitude [93].

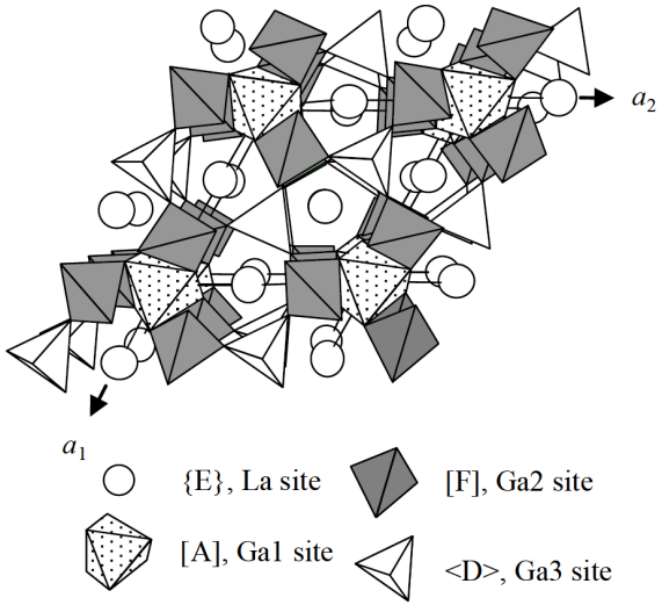

Figure 1-6. Schematic illustration of the langasite crystal structure viewed along [001] direction [93] (copyright 2011 by the Authors).

As in the LGS, LGG, LGN, and LGT crystals discussed above, Ga^{3+} could occupy (F), <D> and [A] sites. Then, those kinds of langasite-type crystals are so called "disordered" langasite crystals and the disorder structure leads to higher acoustic losses, lower acoustic velocity and non-uniform mechanical properties [104]. Recently, a few "ordered" langasite-type crystals have been studied and 4 compositions are identified based on the structural analysis and the stability constraints: $Ca_3NbGa_3Si_2O_{14}$ (CNGS), $Ca_3TaGa_3Si_2O_{14}$ (CTGS), $Sr_3NbGa_3Si_2O_{14}$ (SNGS) and $Sr_3TaGa_3Si_2O_{14}$ (STGS), in which Ca^{2+}/Sr^{2+}, Nb^{5+}/Ta^{5+}, Ga^{3+}, and Si^{4+} occupy the {E}, [A], (F), and <D> sites, respectively [18, 104-108]. Additionally, Al^{3+} modified crystals $Ca_3TaAl_3Si_2O_{14}$ (CTAS) were grown successfully by Czochralski method, which possesses similar piezoelectric performance with STGS, SNGS and CTGS, and reduce the cost [109]. Figure 1-8 presents the dielectric loss of SNGS, STGS, CTGS and CTAS as a function of temperature, from which it could be obtained that the losses of the "ordered" langasite-type

crystals are very small (<0.001) when temperature is below 500°C [18]. The main properties of 10 kinds of commonly used langasite-type crystal could reference Table I in [18].

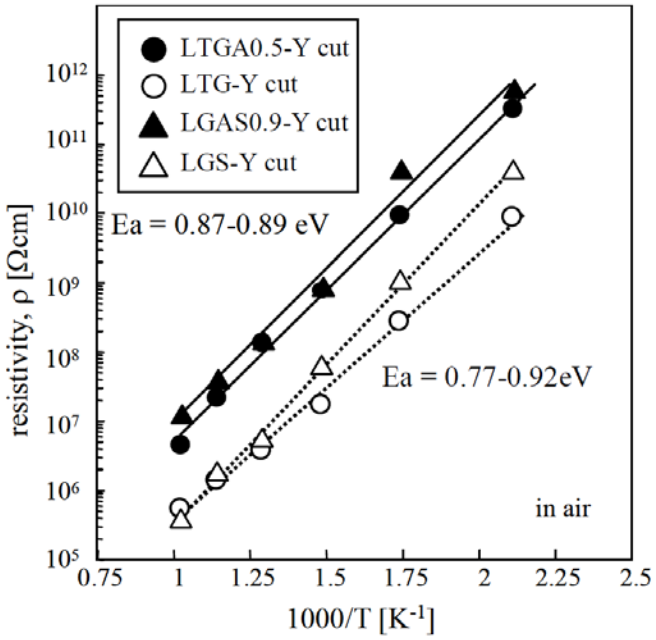

Figure 1-7. Resistivity ρ as a function of temperature for pure and Al-substituted crystals [93] (copyright 2011 by the Authors).

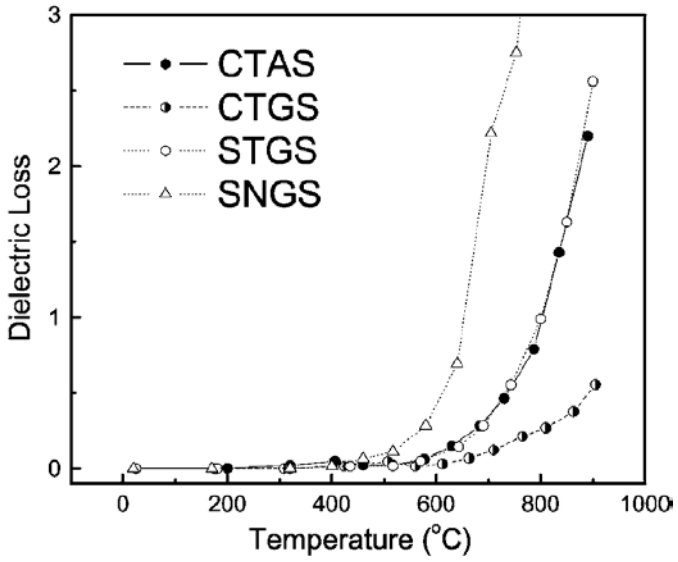

Figure 1-8. Dielectric loss as a function of temperature for ordered langasite-type piezoelectric crystals [18] (copyright 2009 by the AIP Publishing).

1.3.2.3 Rare earth (Re)-calcium oxyborate crystals

Rare Earth (Re)-Calcium oxyborate crystals belong to the monoclinic crystal system, m crystal class, with the chemical formula $ReCa_4O(BO_3)_3$ (ReCOB, Re are rare earth elements, such as Er, Y, Gd, Sm, Nd, Pr and La) and they were first reported in 1992 [110]. The ReCOB crystals possess the same crystal structure, in which there are three types of distorted octahedral sites: Ca(1), Ca(2)) and Re(1) and they are occupied by two kinds of Ca^{2+} and one kind of Re^{3+}, respectively. In each octahedron sites, there are six O^{2-}, two of which occupy the vertex angles of the octahedron, while the other four O^{2-} form a parallelogram as shown in Figure 1-9 [111]. Similar to langasite family crystals, ReCOB crystals could be grown by the Czochralski method and the Bridgman method [112-115].

ReCOB crystals are considered as excellent nonlinear optical materials, for they have lots of wonderful laser and other optical-related performance. For instance, GdCOB crystals are easy to grow and absolutely non-hygroscopic, and YCOB crystals possess large birefringence [116]. Meanwhile, ReCOB family crystals exhibit exceptional piezoelectric properties, especially at elevated temperatures: ε_{22}^{T} is about 15.5 for NdCOB, k_{26} is about 31.5% for PrCOB, and d_{26} is about 15.8 pC/N for PrCOB; of particularly significance, they have no phase transformations prior to their melting points (~1500°C) and the electric resistivity is ultrahigh (~10^8 Ω·cm at 1000°C for ErCOB) [111, 117-120]. Figure 1-10 gives the electrical resistivities of Y-cut ReCOB samples as a function of temperature and the extrapolated room-temperature resistivities are shown in the inset. It could be seen that with the increasing of the Re^{3+}, the electrical resistivities decrease (except for the LaCOB). And the values of the resistivity go from 10^6 to 10^8 Ω·cm for different ReCOB crystals at 1000°C [120].

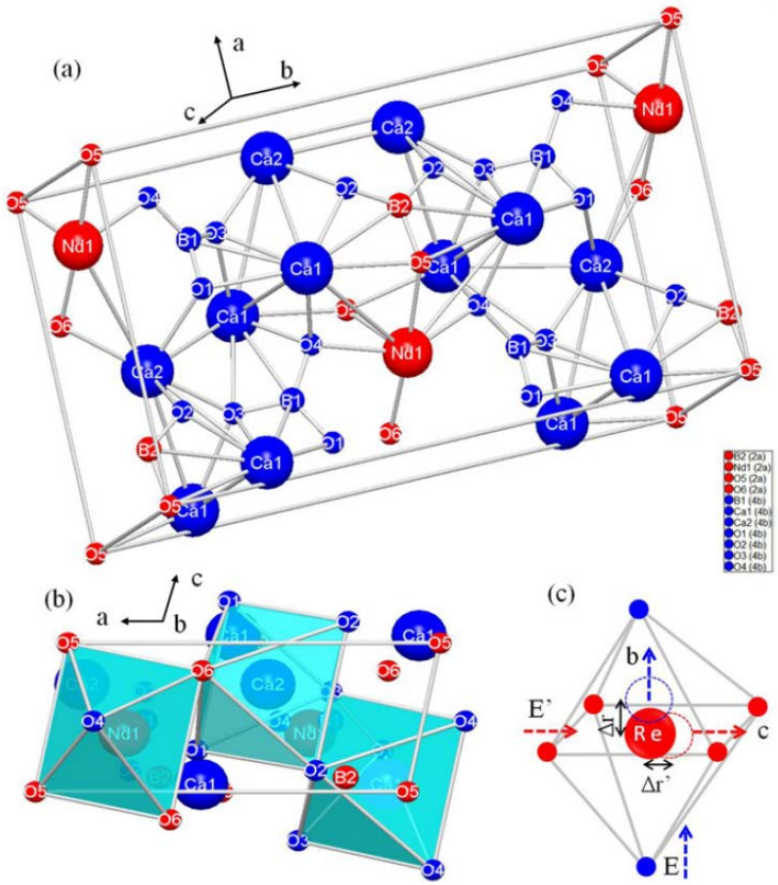

Figure 1-9. Schematic crystal structure of ReCOB crystals [111] (copyright 2011 by the IOP Science). (from ICDD database; Nd could be replaced by other Re elements, (a) observed from the a-axis, (b) observed from the b-axis and (c) schematic of ionic displacement movement).

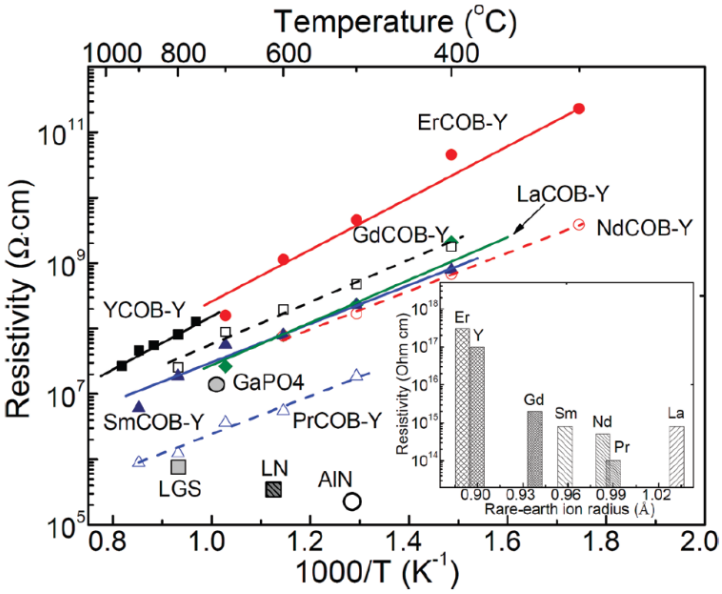

Figure 1-10. Electrical resistivity (ρ) of Y-cut ReCOB (Re = Er, Y, Gd, Sm, Nd, Pr, and La) crystals at room temperature (inset) and elevated temperatures [120] (copyright 2014 by the IEEE).

Together with the electrical resistivity (ρ), the dielectric permittivity $\varepsilon_{22}^{T}/\varepsilon_0$, elastic compliance s_{66}^{E}, the piezoelectric coefficient d_{26}, the electromechanical coupling factor k_{26} and the mechanical quality factor Q_{26} of the ReCOB family crystals are affected by two factors: the Re^{3+} ion radius and the disorder distribution of Re^{3+} and Ca^{3+}. The former factor could change the length of Re-O bond, the volume of the Re-O oxygen octahedron and further the S_6 strain, while the latter one would result in the phonon scattering like the defects [120]. Figure 1-11.(a) shows the $\varepsilon_{22}^{T}/\varepsilon_0$ and d_{26} as a function of the absolute value of the radius difference between the Re^{3+} ion and the Ca^{2+} ion ($|R(Re^{3+})-R(Ca^{2+})|$) and Figure 1-11.(b) presents the k_{26} and Q_{26} as a function of that value. It could be seen that with the increasing of the value, $\varepsilon_{22}^{T}/\varepsilon_0$, d_{26} and k_{26} decrease and Q_{26} increase. It is worth mentioning that the radius of La^{3+} is larger than that of Ca^{2+} (1.00 Angstrom) and the radii of Pr^{3+}, Nd^{3+}, Sm^{3+}, Gd^{3+}, Y^{3+}, Er^{3+} are smaller than Ca^{2+}

ion's. That's why the four parameters ($\varepsilon_{22}^{T}/\varepsilon_0$, d_{26}, k_{26} and Q_{26}) of LaCOB are a little unsocial [111, 120].

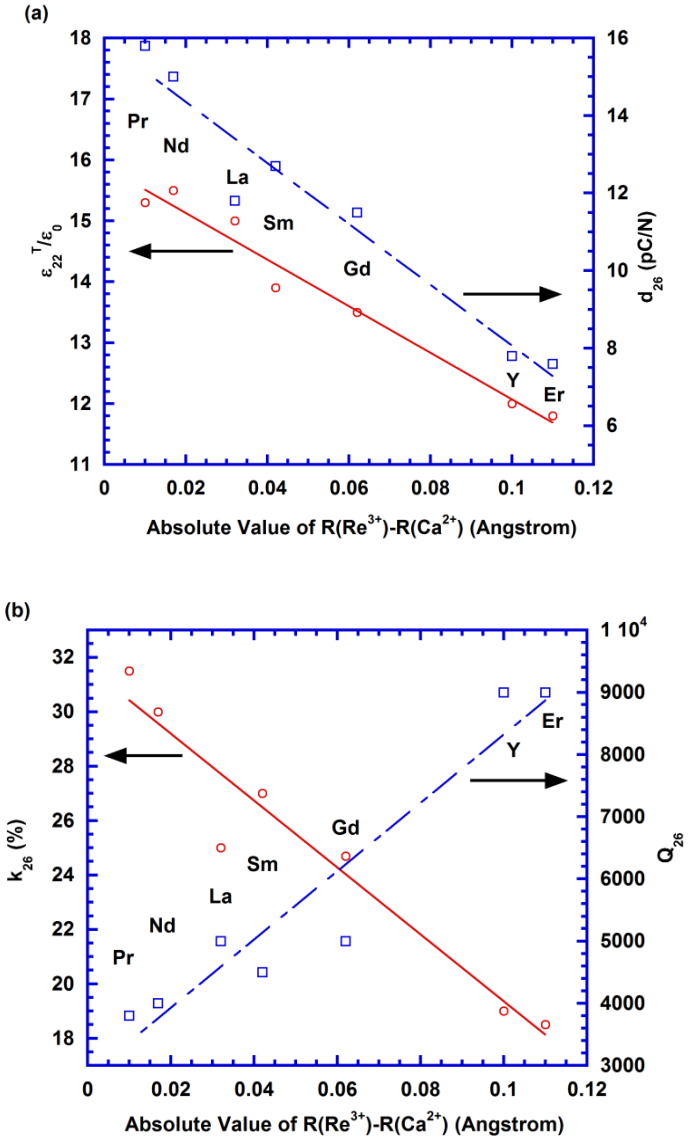

Figure 1-11. (a) The dielectric/piezoelectric constants and (b) the electromechanical coupling/mechanical quality factors of the ReCOB family crystals, as a function of the absolute value of the radius difference between the Re^{3+} ion and the Ca^{2+} ion ($\left|R(Re^{3+})-R(Ca^{2+})\right|$) (data obtained from reference [111, 120]).

1.3.3 Some other high-temperature piezoelectric crystals

AlN (Aluminum nitride) was first synthesized in 1877 and found the application in microelectronics in the middle of 1980s for its high thermal conductivity (200 W/(m·K) for AlN ceramic [121, 122], and about 319 W/(m·K) for single crystal [123]. Also, AlN exhibits high electrical resistivity, low density and matches well with silicon, which make it attract lots of attention. It is reported that the surface oxidation occurs above 700°C in air [124] and AlN stays stable in hydrogen and carbon dioxide atmospheres up to 980°C [125]. AlN single crystal could be grown by the sublimation technique at about 2300°C [126] or physical vapor transport (PVD) [127]. AlN bulk single crystals are promising candidate for UV applications [128], while its thin films are widely used in surface acoustic wave (SAW) devices and thin film bulk acoustic resonator (FBAR) [129].

Relaxor based ferroelectric single crystals, such as $Pb(Zn_{1/3}Nb_{2/3})O_3$-$PbTiO_3$ (PZNT) and $Pb(Mg_{1/3}Nb_{2/3})O_3$-$PbTiO_3$ (PMNT), are investigated for electromechanical actuators results from their low dielectric loss (<1%), ultra-high piezoelectric coefficient (d_{33}>2500 pC/N), and large electromechanical coupling factor (k_{33}>90%) [32, 40, 41]. However, the low Curie temperature (~170°C) and even low rhombohedral to tetragonal phase transition temperate (~120°C) restrict their high-temperature applications [41]. The crystals could be grown from flux growth technique and modified Bridgman technique [130-132].

The general properties of 9 kinds of representative single crystals are summarized in Table 1-7 (only ferroelectrics have the Curie point).

Table 1-7. General properties of 9 kinds of representative piezoelectric single crystals.

Crystals	Melting point (°C)	Curie point (°C)	$\varepsilon_{r,eff}$	c_{eff} (GPa)	d_{eff} (pC/N)	k_{eff} (%)	Q_{eff}	ρ (Ω·cm)	Temp range (°C)	Ref
Quartz	1670	--	4.65	6~106	2.25	<1	10^5~10^8	$>10^{17}$	~300	[23,28, 55-59]
Tourmaline	1102	--	6-8	160~300	1.8~3.6	~10	--	--	~700	[64-69]
LN	1255	1140	28~85	53~245	1~69	~60	10^2~10^4	~10^{10}	~700	[70-76]
$GaPO_4$	1670	--	6.6	4.6~67	4.5	~16	~10^4	~10^{17}	~900	[82-86]
LGS	1470	--	19	14~268	6	~16	~10^4	~10^{15}	~1100	[89-104]
CTGS	1350	--	18.2	0.4~178	4.6	~12	~10^4	~10^{17}	~1100	[105-109]
YCOB	1510	--	12	0.7~155	3~10	~22	~10^4	~10^{17}	~1250	[117-120]
AlN	2200	--	9	~330	--	~7	~10^4	$>10^{14}$	~500	[120-129]
PMNT	1270	170	~5000	3~16	>2500	>90	~10^2	~10^9	~120	[129-132]

1.4 SENSING APPLICATIONS OF HIGH-TEMPERATURE PIEZOELECTRIC CRYSTALS

It was in the 1950s that the piezoelectric effect began to be considered for sensing applications. Compared to other types of sensing techniques, such as piezoresistive, capacitive and fiber optic sensors, piezoelectric sensors exhibit higher resolution of strain, larger frequency range, better temperature stability, shorter response times, easier to integrate and lower cost [133]. Moreover, piezoelectric crystals have a higher long-term stability and lower loss than the piezoelectric ceramics and the high-temperature sensors are in great demand in aircraft, aerospace, energy and automotive industries [9-13]. High-temperature piezoelectric crystals are therefore extensively studied and widely used. According to whether the acoustic waves are applied to sense the physical or chemical changes, the piezoelectric sensors could be divided into Acoustic Wave (AW) sensors and Non-Acoustic Wave sensors. Among the AW sensors, Surface Acoustic Wave (SAW) sensors and Bulk Acoustic Wave (BAW) sensors are resonant-based sensors and have been most extensively investigated and applied. On the other hand, in the light of the functions, the piezoelectric sensors could be classified as temperature sensors, pressure sensors, mass sensors, gas sensors, flow sensors, chemical sensors, bio-sensors and so on. In this section, high-

temperature piezoelectric crystal sensors are discussed on the basis of the principals, especially the SAW and BAW sensors, and certain corresponding functional sensors will be described.

1.4.1 Surface AW sensor

Surface acoustic wave (SAW) is an acoustic wave propagating along the surface of materials exhibiting elasticity, which was first described by Lord Rayleigh in 1885 [134]. SAWs have a longitudinal and a vertical shear components coupling with any media on the surfaces, which would change the amplitude and velocity of the SAWs and make the SAW sensors could sense the temperature, pressure, mass and other properties accordingly. The SAW sensors transduce an input electrical signal into a mechanical wave by the input interdigitated transducers (IDTs) [135], and the wave, which could be affected in amplitude, phase or frequency by the physical parameters to be detected, could be transduced back into the electrical signal by the output IDTs. Then, the changes between the input and output signals could reflect the desired physical parameters [136-138]. Concretely, through the IDTs fabricated on the surface of the substrate, the SAW devices could generate Rayleigh waves, which consist of two particle displacement components: surface particles move in paths with the surface parallel or normal to the direction of the propagation. The energies of the waves are confined into the area within several wavelengths depth from the surface. Two sets of IDTs are needed: one to launch the SAW, while the other one to detect it. All the physical or chemical changes loaded between the two sets of IDTs would be reacted by the differences between the launched and detected waves [136]. Depending on the line-width of the IDTs, the frequency range of the SAWs could cover 50 MHz to a few GHz [139] and the IDTs are usually fabricated by the lithography technique [140]. The decisive advantage of the SAW sensors is the possibility of processing wireless without using

cables and energy sources, even in the harsh environments [141-143]. Thus, piezoelectric crystal SAW sensors are suitable for high-temperature measurement and have been found a wide range of applications.

R. Hauser *et al*. have investigated the acoustic attenuation loss and the aging of the $LiNbO_3$ SAW devices up to 450 °C for more than 10 days [144]. As shown in Figure 1-12.(a), the aging of $LiNbO_3$ exhibits a continuous decrease below 450°C, which maybe resulted from the decomposition over the congruent melting point (300°C). Furthermore, the tested economic life-time at 400°C is more than 10 days and the predicted lift-time at 300°C based on ARHENIUS equation is as long as 10000 days, which are given in Figure 1-12.(b) [144].

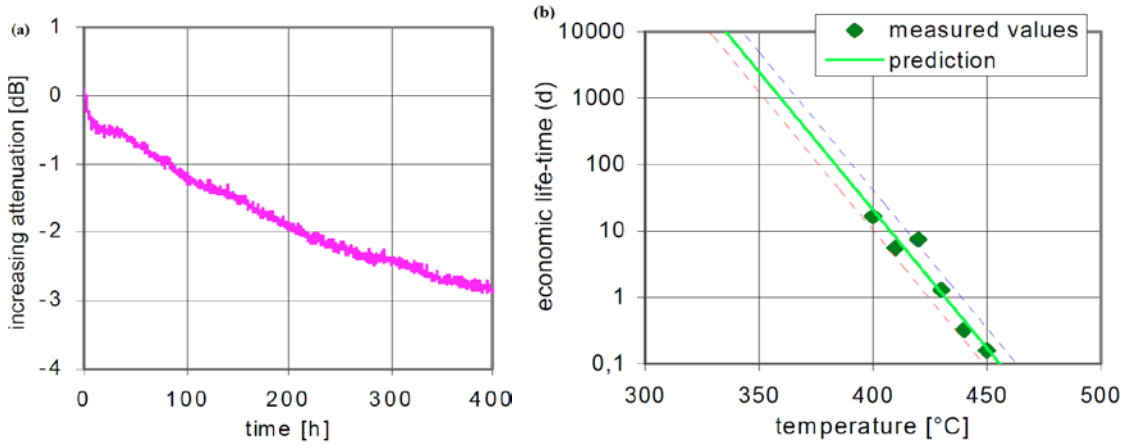

Figure 1-12. (a) Long time ageing of the investigated ID-tag at 400°C (b) Measurements of the long-time thermal stability of LiNbO3 SAW devices up to 450°C and the predicted lift-time at 300 °C [144] (copyright 2003 by the IEEE).

M.N. Hamidon *et al*. have successfully fabricated a kind of SAW sensor based on $GaPO_4$, which could be operated up to 600°C inside the ISM-band (around 434 MHz) [145, 146]. The

IDTs of their devices were fabricated according to the e-beam lithography with lift-off technique and have 50 fingers, 50 wavelength aperture, 200 strips short circuit reflectors and 1.4 μm finger width with the 1:1 finger to space ratio. The Y-Boule orientations with a 5° cut with the dimension of 3.5 cm × 4.5 cm $GaPO_4$ crystal wafers were used. And the electrode metallization was platinum (Pt) with titanium (Ti) or zirconium (Zr) as the adhesion layer [145]. They reported that for the devices with Zr adhesion layer and 82 nm Pt electrode there was no oxidation at 600°C and the resonate frequencies were stable for more than 3500 hours with a small drift 0.03 ppm/h [146]. These gratifying results provide evidences for the conclusion that $GaPO_4$ based SAW sensors could be used up to 600°C for a long time.

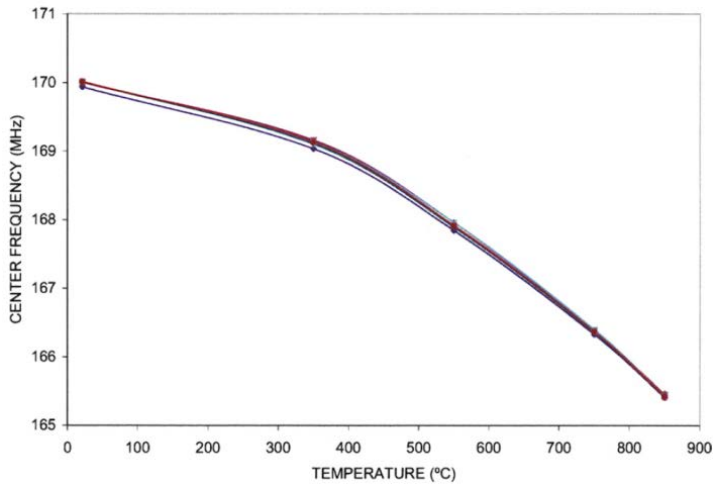

Figure 1-13. Measured center frequency for a Pt/10%Rh/ZrO_2 deposited two-port LGS SAW sensor while being cycled from room temperature to 850°C six times [147] (copyright 2008 by the IEEE).

LGS crystals based high-temperature SAW sensors also have been widely investigated. Cunha et al. have studied the two-port LGS SAW sensors up to 850°C [147]. The Pt/10%Rh/ZrO_2 electrode which was deposited through the e-beam evaporation method was

used. And the IDTs fabricated by the lift-off techniques possessed 80 fingers, 50 wavelength aperture, 500 electrode short circuit reflectors, 4 μm finger width with 1:1 finger to space ratio. The center frequency response of this type sensor cycled six times between room temperature and 850°C was measured and the result is shown in Figure 1-13 [147]. As could be seen, the center frequency stays relatively stable from room temperature to 850°C (less than 5 MHz drift occurred compared to the 170 MHz center frequency) and the major changes take place in the 550-850°C. Also, long term (4080 hours) operation for this kind device at 800°C was taken and the results support its stability. Thiele *et al*. have made detecting the H_2 and C_2H_4 in N_2 up to 250°C and 450°C, respectively, by the LGS SAW gas sensor to be a reality [148].

1.4.2 Bulk AW sensors

Analogously, bulk acoustic wave (BAW) sensors also utilize the acoustic waves as the sensing mechanisms to detect the physical or chemical quantities (mass, gas, chemical, viscosity *et al*.) by measuring the changes of the velocity, frequency, phase or amplitude of the acoustic waves. Unlike the surface acoustic waves, the bulk acoustic waves propagate through the entire devices [149]. In general, according to the structures, orientations of the substrate materials, and the directions of the applied electrical excitations, the substrates would be excited to lots of different vibration modes (usually, thickness shear mode and shear-horizontal mode are utilized). With certain vibration modes, the basic parameters of the BAW would be determined. Once the physical or chemical quantities are loaded to the substrates, the parameters would change, and the parameters change of the wave could be used to determine the loaded quantities. There are many different types of BAW sensors with a variety of vibration modes. For example, the piezoelectric plate sensors could be excited to several extensional modes, face-shear modes,

thickness shear modes, flexural modes and twist modes; the long thin rod sensors can be exploited as the extensional, bending or torsional modes [139]. The most commonly used BAW sensors are the thickness shear mode (TSM) and the shear-horizontal acoustic plate mode (SH-APM) sensors [149]. The TSM sensors, usually referred to as the quartz crystal microbalance (QCM), are the earliest and most extensively used BAW sensors since they do not generate compressive waves in the surrounding medium [17, 150]. QCM has lots of chemistry and electrochemistry applications for its large detection range (from monolayer surface to large masses), high mass sensitivity (measurable mass density down to 1 $\mu g/cm^2$) and wide applicable environment (gas and liquid phases) [151-153]. SH-APM sensors utilize a thin piezoelectric plate to confine the energy between the two surfaces, which results in that both surfaces undergo displacement and are detectable [149]. In addition, thin film bulk acoustic resonator (FBAR or TFBAR) is widely investigated for its small size, high quality factor and high targeted frequency (radio frequency 1~10 GHz) [154].

In 1959, QCM was first reported in the sensing mode in one paper of Sauerbrey, where he obtained the linear relationship between the mass of deposited metal on quartz crystal and its frequency decrease [155]. Seh *et al*. from MIT developed high sensitive NO_x gas sensor (up to 400°C) by exploiting QCM and the schematic of the sensor is shown in Figure 1-14.(a) [156]. Through the PMMA templating technique, $BaCO_3$ films (800 nm or 400 nm in diameter) were deposited on one gold electrode of the QCM (5 MHz, AT-cut). $BaCO_3$ was selected as the active film for it reacts with NO_2 to form $Ba(NO_3)_2$ with the mass change. The mass sensitivity of this QCM sensor was found to be 1 ng/(cm_2·Hz) and the largest change in Δf_0 was -2000 Hz (at 400°C and 100 ppm NO_2) which is shown in Figure 1-14.(b) [156]. $GaPO_4$ and LGS are investigated as alternatives to quartz, which could be used at higher temperatures and are also

called QCM even though they are not made of quartz. Thanner *et al*. reported that they used Y-11° cut $GaPO_4$ (diameter 7.4 mm, resonant frequency near 6.2 MHz) as the QCM mass sensor and measured the mass change of lube oil deposited on its surface up to 720°C [157]. Seh *et al.* also investigated the 1%Sr-LGS, 5%Nb-LGS and updoped LGS BAW gas sensors' performance from 700 to 1000°C and presented their bulk conductivities as functions of temperature and oxygen partial pressure, from which they demonstrated that the LGS BAW sensors were possible to operate to 800ºC from oxygen partial pressures of 1 atm down to 10-12 atm with Q≥500 [158, 159].

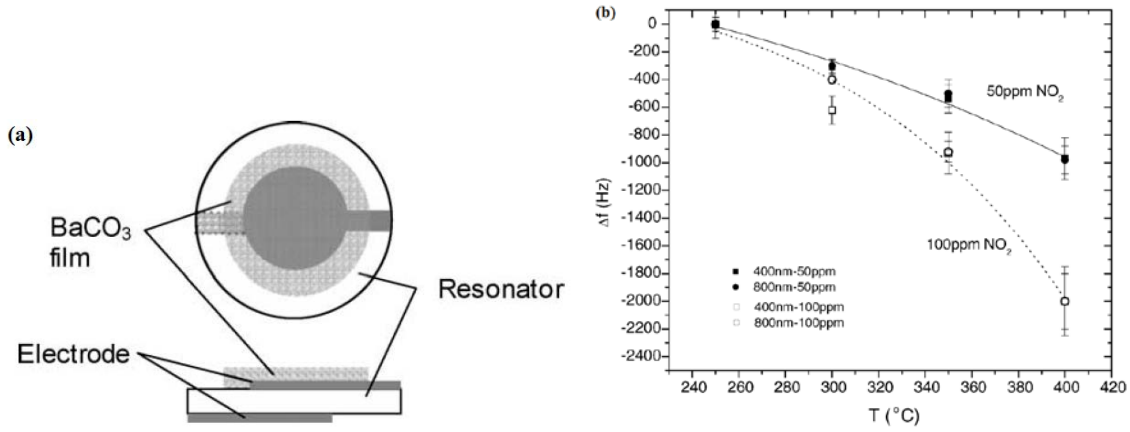

Figure 1-14. (a) Schematic of NO2 QCM sensor, (b) Comparing responses to NO_2 at different temperatures and two different $BaCO_3$ microstructures [156] (copyright 2005 by the ELSEVIER).

SH-APM devices possess two major advantages: they could work in a liquid medium without excessive acoustic loss and could work in an aggressive medium [160]. Déjous *et al.* studied the temperature-compensated properties of ST-cut quartz SH-APM sensors up to 200°C and showed their performance in biological media (sodium chloride and

tris(hydroxymethyl)aminomethane) [160, 161]. FBARs are extensively used as filters in cell phones and other wireless applications and the common materials for FBARs are AlN [162-164] and ZnO [165-167]. As for single crystal FBARS, Osugi *et al*. studied the LN FBARs (45° Y-cut, 1μm thickness) with the resonance frequency at 2.12 GHz and Δf of 159 MHz and presented that they had higher coupling factor and $\Delta f / f_r$ (30.6% and 12.4%, respectively) than AlN (6.54~7% and 2.7~2.8%, respectively) [168]. However, few reports about the applications of high temperature crystal FBARs.

1.4.3 Non-resonant piezoelectric crystal sensors

Piezoelectric accelerometers employ the piezoelectric effect of some piezo-materials and first convert the acceleration into a force or displacement through a seismic mass and then convert them into an electrical quantity. Piezoelectric accelerometers are widely used in industry and science to measure the dynamic changes in the vibration and shock. High-temperature piezoelectric crystal acceleration with high sensitivity and stability are in great demand in the engine field where the accelerometers should work in the harsh environments with high temperature, high pressure and high oscillation [169, 170]. Tian *et al*. designed and developed a quartz-flexure accelerometer operating in low frequency range based on the capacitive sensing and electrostatic control technology and the results showed that the resolution was about 8 ng/$Hz^{1/2}$ [171]. Zhang *et al*. fabricated and tested the accelerometer made by thickness mode (XY*lw*)-15°/45° cut YCOB crystals up to 1000°C and over a frequency range of 100-600 Hz [172]. It was found that, the accelerometer possessed a high sensitivity (2.4±0.4 pC/g) across the temperature and frequency range, which is shown in Figure 1-15, and it could stay stable at 900°C for more than 3 hours.

Cantilever which has been extensively used for energy harvesting [173, 174], or as biosensors and chemical sensors is a common structure in microelectromechanical systems (MEMS). Cantilevers are often made from silicon, silicon nitride or polymers, and PMN-PT is the widely used piezoelectric single crystal for cantilevers for its high coupling coefficient and piezoelectric constant [174-176]. In addition, unimorphs [177] and bimorphs [178] cantilevers are also commonly used. Acoustic emissions (AE) are the sound waves generated by dynamic stress in a material and the AE sensors play a significant role in the non-destructive inspection field [179]. Kirt *et al*. developed the lithium niobate 1-3 piezocomposites (with high-temperature-resistant cement) acoustic emission sensors by using the dice and fill method [180]. According to their test, the 4 mm thick sensor with 45% volume fraction of y/36° cut presented the best results and could work over the temperature range from room temperature to 400°C. Johnson *et al*. designed, fabricated and tested the YCOB single crystal AE sensors and acquired the following result: the sensitivity of the sensor had small to no degradation with the increasing temperature, which demonstrated the ability of YCOB crystal AE sensors to detect zero symmetric and antisymmetric modes up to 1000°C [181, 182].

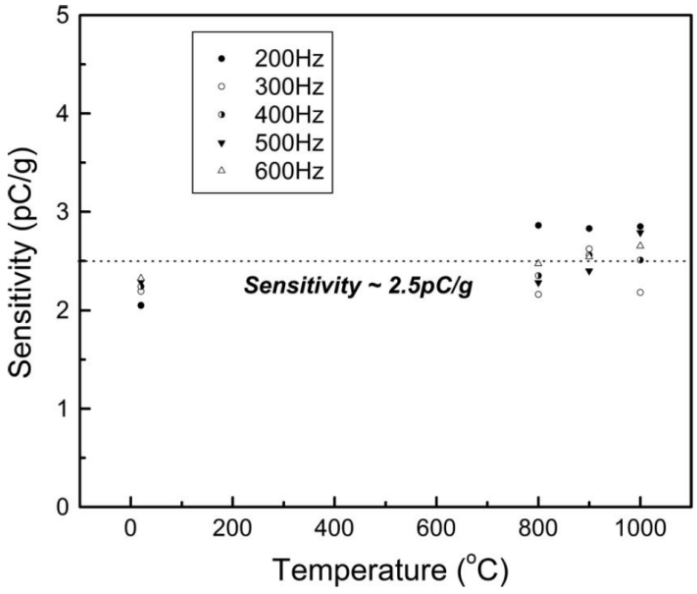

Figure 1-15. Sensitivity of the YCOB accelerometer as function of temperature up to 1000°C at different frequencies [172] (copyright 2010 by the AIP).

1.5 MOTIVATIONS AND OBJECTIVES OF THIS WORK

1.5.1 Motivations

The industrial and scientific communities have expressed an urgent need for the robust pressure, gas, vibration sensors capable of operation in harsh environments, e.g. high-temperatures, aggressive media, intense shocks, and radiation exposure, in order to meet the growing requirements of some modern industrial fields, including oil and gas extraction, power plants, and aerospace. Many initial efforts have been made on searching novel materials and

investigating the state-of-the-art sensing technologies for the development of the reliable sensors used in these hazardous conditions, especially high-temperatures [183-186].

The piezoelectric crystal sensors applied in these areas serve both as the internal components of the systems (should be able to work availably and stably for a long term under the corresponding harsh conditions), and as the external detectors (should be able to timely and effectively provide the desired information, such as the temperature, pressure, acceleration and so on). Thus, the selection of the sensor materials is extremely critical. According to the survey of high-temperature piezoelectric crystals in part **1.3**, the ordered langasite family crystals and Rare Earth (Re)-Calcium oxyborate crystals are the most promising materials for high-temperature sensing for the absence of phase transition prior to their melting points (~1500ºC) and the excellent electromechanical performance. Among the two groups of crystals, CTGS and YCOB should be at the very top of the candidates list, because they possess the highest electric resistivity (10^7~10^8 Ω·cm at 1000ºC) and stability, and lowest loss at elevated temperatures.

As for the sensing techniques, the piezoelectric sensors have been demonstrated to have many advantages over other types of sensors, such as piezoresistive, capacitive and fiber optic sensors, because they exhibit higher resolution of strain, larger frequency range, better temperature stability, shorter response times, easier to integrate and lower cost. In addition, among the piezoelectric sensors, the resonant-based AW sensors, including SAW sensors and BAW sensors, have been most extensively investigated and applied, owning to their high stability and sensitivity. Furthermore, the BAW sensors are with the property of simple preparation process, easy to use, high temperature-tolerance, high repeatability and durability, and little damping, because neither the interdigitated transducers (IDTs) nor the functional piezoelectric thin film is needed.

Therefore, the study of BAW sensors based on CTGS and YCOB crystals is very promising and will bring revolutionary breakthroughs and developments in robust high-temperature sensors to meet the urgent demands of multiple modern industrial fields. However, the basic properties of CTGS and YCOB crystals, especially their temperature dependence, haven't been fully characterized, and the research on their practical applications is very limited.

1.5.2 Objectives

The overall goal of this study is to fist fully characterize the basic properties of CTGS and YCOB crystals, especially the real and complex dielectric, elastic, and piezoelectric constants, from room temperature to high temperatures, and then develop robust and reliable BAW temperature, mass, and pressure sensors that can be used at elevated temperatures accordingly.

Chapter 2 and 3 will sequentially present the full characterization of the basic properties of CTGS and YCOB crystals from room temperature to 800ºC. Chapter 4 to 6 will show the studies on BAW sensor applications under high temperatures based on CTGS and YCOB: Chapter 4 will discuss the optimal temperature sensors which are functional up to 1000ºC; Chapter 5 will exhibit the high-temperature mass sensors for thermogravimetric analysis; Chapter 6 will investigate the high-temperature pressure sensors, as well as the non-linearity effects. Finally, Chapter 7 will be the conclusion and prospect.

This chapter includes materials excerpted from the following publication of the author:

Zu, Hongfei, Huiyan Wu, and Qing-Ming Wang. "High-Temperature Piezoelectric Crystals for Acoustic Wave Sensor Applications." IEEE transactions on ultrasonics, ferroelectrics, and frequency control 63.3 (2016): 486-505.

2.0 FULL CHARACTERIZATION OF THE BASIC PROPERTIES OF $CA_3TAGA_3SI_2O_{14}$ CRYSTALS UP TO 800ºC

In the past decades, a number of methods have been developed to characterize the electromechanical properties of piezoelectric materials. The widely accepted measurement procedures and parameter extraction methods for linear (dielectric, piezoelectric and elastic coefficients are considered as constants independent of the applied electric fields and mechanical stresses) and low loss (electrical and mechanical dissipations could be neglected) piezoelectric materials have been stated in the "IEEE Standard on Piezoelectricity" [6]. Based on the applied electric excitations, direct current (DC) or alternating current (AC), the earliest techniques could be divided into static and quasi-static measurements [35]. However, they were rapidly replaced by the dynamic methods, since the dynamic methods are with greater accuracy and much wider range of applications. Dynamic methods are also called "resonator methods", because they take advantage of the principle that the electrical properties (impedance or admittance) of a piezoelectric resonator are dependent on the dielectric, piezoelectric, and elastic coefficients of the materials. Thus, by measuring the electrical impedance or admittance of a series of resonator specimens with various crystalline orientations and shapes as a function of frequency, those coefficients could be determined [6, 35].

For lossy materials, if the IEEE standards are directly employed to determine the electromechanical properties, significant errors would be introduced, because the electrical and

mechanical dissipations are significant and cannot be ignored. The non-negligible dissipations could be incarnated by expressing the properties with complex coefficients [187]. And even for the low loss materials, the complex coefficients could further improve the accuracy of the expression compared to the real ones obtained through IEEE dynamic methods. Several methods have been proposed to acquire the complex dielectric, piezoelectric, and elastic coefficients of piezoelectric materials: Smits [188] reported an iterative method which compels the admittance or impedance to satisfy the experimental results at three chosen frequencies. This method is accurate for the chosen frequencies, however, for other data points, the errors are often uncontrollable, and the results are over-reliance on the selected points which makes it lack of universality. Kwok *et al*. [189] developed a curve fitting method to obtain the complex coefficients, however, similar to the iterative method, this method has a certain degree of randomness, because the data exploited dominates the outcome of the fitting. To overcome the weaknesses of the previous methods, Du *et al*. [49, 50, 190] introduced a new approach which deduces the complex coefficients from the admittance or impedance information near the resonant frequency: the maximum and minimum normalized susceptance $\overline{B}$, (or reactance $\overline{X}$), and the maximum normalized conductance $\overline{G}$ (or resistance $\overline{R}$). The information is sensitive to the desired coefficients and the method has been successfully applied to the complete characterization of materials properties of piezoelectric Lead Zirconate Titanate (PZT) ceramics and Lithium Niobate ($LiNbO_3$) single crystals.

For CTGS crystals, Shi *et al*. [191] reported all its dielectric, piezoelectric, and elastic properties at ambient temperature; Yu *et al*. [192] studied some of the dielectric and electromechanical properties over the temperature range of -60~700°C. However, to the best of our knowledge, the temperature behaviors of all dielectric, piezoelectric, and elastic constants of

CTGS have not been completely reported yet. A systematic study is therefore needed to fully characterize all the constants over a wide temperature range for the device development and applications.

In this chapter, we will characterize all the real and complex dielectric, piezoelectric, and elastic constants of CTGS single crystals over a wide temperature range (from ambient temperature to 800°C) using the IEEE dynamic methods and the techniques developed by Du *et al*, respectively. And the temperature dependence of the materials properties will be discussed. The results will provide a more comprehensive understanding of the material electromechanical behavior in a wide temperature range and assist further development of device applications using this novel piezoelectric crystal.

2.1 EXPERIMNTAL DETAILS

As one may know, for a single crystal, the material growth, post-processing, or measurement system differences will more or less result in the discrepancies in the measurement results. Therefore, it is necessary to clarify the entire process of the sample processing and experimental preparation in detail, including the crystal growth, sample cutting and polishing, electrode deposition, sample mounting, measurement system settings, and so on, in order for the future reference and comparison.

2.1.1 Sample processing

The CTGS crystals were grown by the Czochralski (CZ) pulling technique using an automatic diameter control (ADC) CZ furnace, and high purity raw materials: $CaCO_3$, Ta_2O_5, Ga_2O_3, and SiO_2. The powders of these four raw materials were first mixed in stoichiometric ratio and sintered at 1250°C for 24 h. And then, the sintered polycrystalline materials were loaded into an iridium (Ir) crucible and melted at 1350°C. Subsequently, a CTGS crystal with ⟨110⟩ direction was used as the seed to pull the melted materials to form the single crystals at a rate of 0.5-1 mm/h with the rotation of 5-15 rpm. During the crystal growth processing, the N_2 plus 1 vol % O_2 atmosphere was employed to protect the Ir crucibles and prevent the generation of the oxygen defects in the crystals [18]. Finally, the as-grown crystals were slowly cooled down to room temperature at a rate of 30 °C/h to avoid the possible cracking.

As indicated above, samples of various orientations and shapes are needed to completely determine the elastic, dielectric, and piezoelectric coefficients, no matter which method is going to be applied. According to our calculation for crystal resonator design, seven crystal resonator samples with the specific crystal cuts shown in Figure 2-1 are sufficient for the determination of both real and complex coefficients of the CTGS crystals. The crystal resonator samples can be divided into two categories: square plates (X-cut, Y-cut, and Z-cut), and rectangular bars (XY-cut, (XY*t*)45°, (XY*t*)-30°, and (XY*t*)-85°), and the photographs of one bar and one plate samples are shown in Figure 2-2. The notations of the sample-cuts follow the IEEE standard [6]: for square plates, the only uppercase letter (X, Y, or Z) represents the initial principal direction of the thickness of the samples; for rectangular bars, the first two uppercase letters (XY) successively indicate the initial principal directions of their thickness and length, and the lowercase letter (*t*, if present) denotes that the direction of the thickness (X) is the axis of the

rotation. The positive angle means the rotation is counterclockwise looking down the positive end of the axis toward the origin, and the negative ones illustrate the rotations are clockwise. The selection of these seven cuts for crystal resonator fabrication will be explained in detail later.

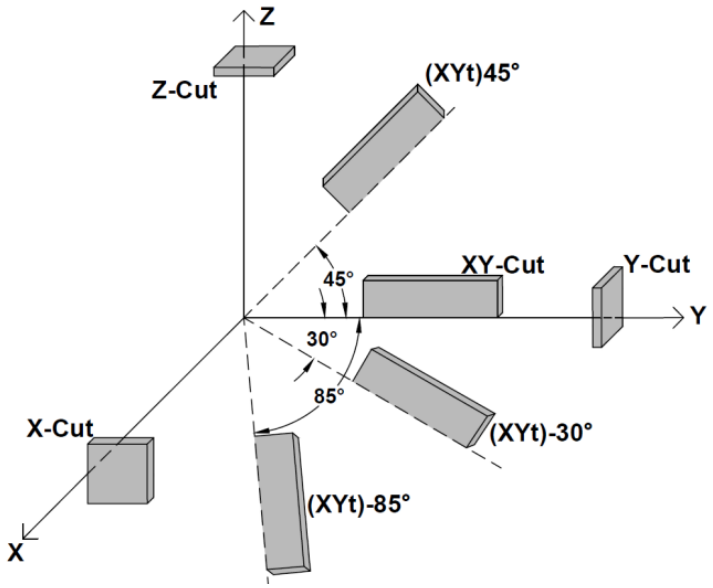

Figure 2-1. Schematic of the CTGS sample-cuts required for the complete determination of the dielectric, piezoelectric, and elastic constants.

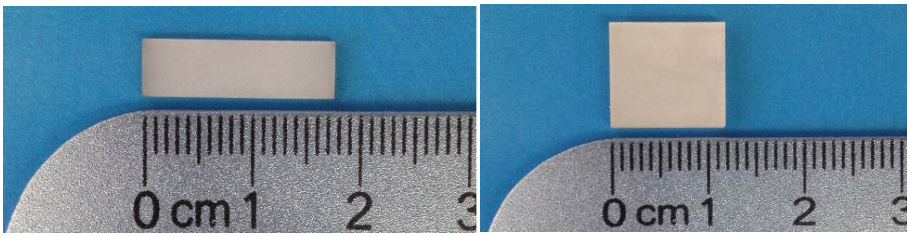

Figure 2-2. Photographs of the rectangular bar and square plate samples.

Next, the desired samples were cut from the crystal blocks with pre-designed orientations and dimensions. The CTGS samples were then pre-ultrasonically cleaned, polished by sandpaper (P2000 grit), polished by alumina powder (1-μm), and post-ultrasonically cleaned, consecutively. Afterwards, 50 nm chrome (Cr) and 150 nm gold (Au) films were deposited sequentially on the target surfaces by the sputtering system (ATC 1300-F, AJA International, Inc.) to serve as the electrodes, which were proved to be able to maintain good electrical conductivity after several rounds of high-temperature (800°C) test.

2.1.2 Experimental preparation

Figure 2-3.(a) schematically shows the measurement system used in this work, while Figure 2-3.(b) exhibits the photograph of the actual system, and Figure 2-3.(c) specifically presents the sample fixture. The samples were put on the sample holder, which can be hung right in the center of the tube furnace (④, Thermo Scientific 79300) through the fixing of the end of the sample fixture. The two electrode surfaces of the sample were connected to the Nichrome wires by fine platinum wires, and then connected to the impedance analyzer (⑤, Agilent 4294A) for further signal acquisition and analysis. The data were extracted and saved through the Labview program installed in the PC (⑥), which were connected to the impedance analyzer. During the measurements, the samples were heated from room temperature to 800ºC with the heating rate of 3-5ºC/min, and the signals at each desired point were recorded after the temperature had stabilized for 10-20 min. The temperature controller (③, Eurotherm 3216) was used for the precise control of the temperature. Throughout the process, the dry N_2 atmosphere was introduced from the gas tank (①) and controlled by the flow controller (②, TEK-VAC

Industries, INC.) to prevent the oxidation of the metals, and the exhaust gas was discharged into the fume hood (⑦).

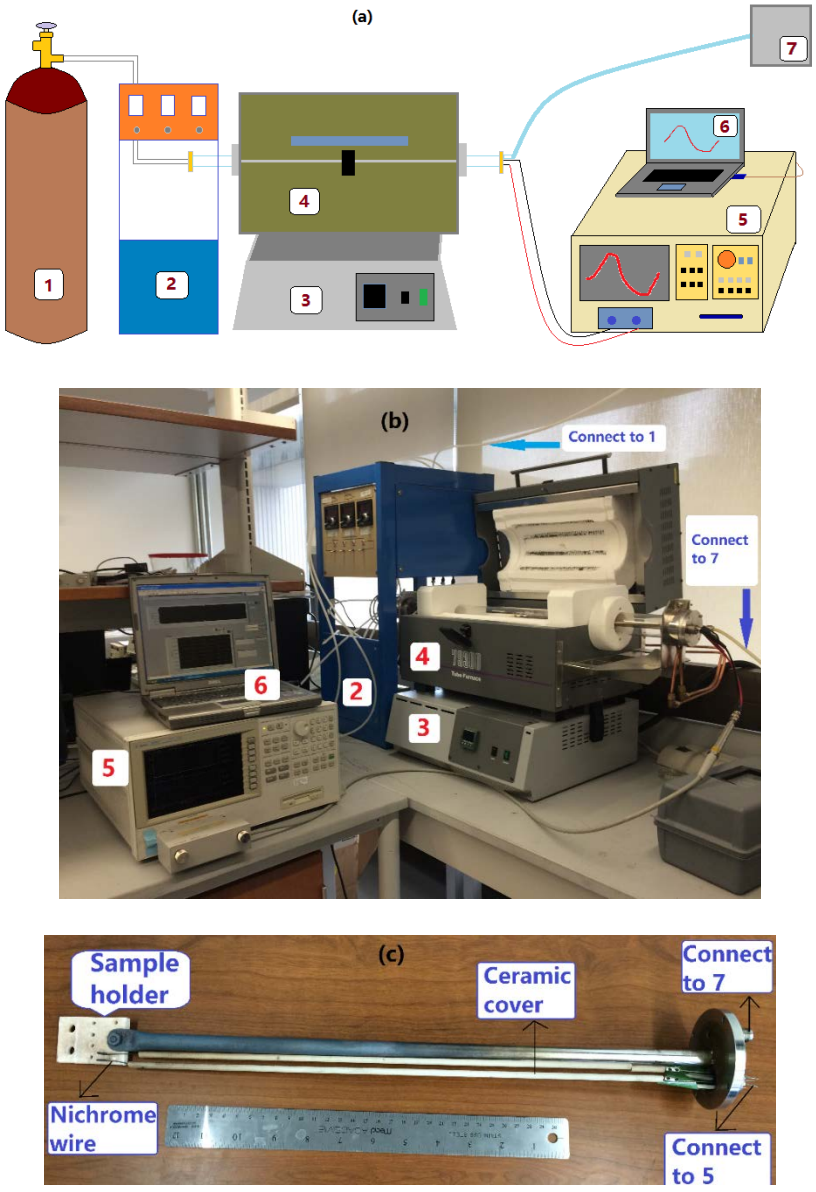

Figure 2-3. (a) Schematic diagram of the measurement system, (b) photograph of the actual system, and (c) sample fixture.

(① N2 gas tank, ② flow controller, ③ temperature controller, ④ tube furnace, ⑤ impedance analyzer, ⑥ PC, ⑦ chemical fume hood).

Sample mounting sometimes can be a very fatal issue, because the improper installation may severely inhibit the vibration of the resonator, resulting in the signals are difficult to detect. In order to minimize this adverse effect, it's necessary to locate the supporting points as close as possible to the nodes, where the displacements of the resonator are zero. However, for some vibration modes, e.g., thickness shear mode, it's hard to fix the sample through the nodes (the middle line) because the thickness is usually too small to leave enough space for the accurate and stable support. To overcome this problem, an alternative approach was designed. As shown in Figure 2-4.(a), both of the two target surfaces of the sample are only partially covered by electrodes, and according to the "energy trapping theory" [193-195], most of the vibration occurs in the area where both of the surfaces are with electrodes. Then, we can open four small grooves at two ends where only one side is deposited with electrode, and wrap the platinum wires through the grooves. In this case, the electrodes can be extracted without any suppression of the vibration. Figure 2-4.(b) exhibits two plate samples processed in this way. In this work, this approach was adopted when the samples are hard to mount through the nodes.

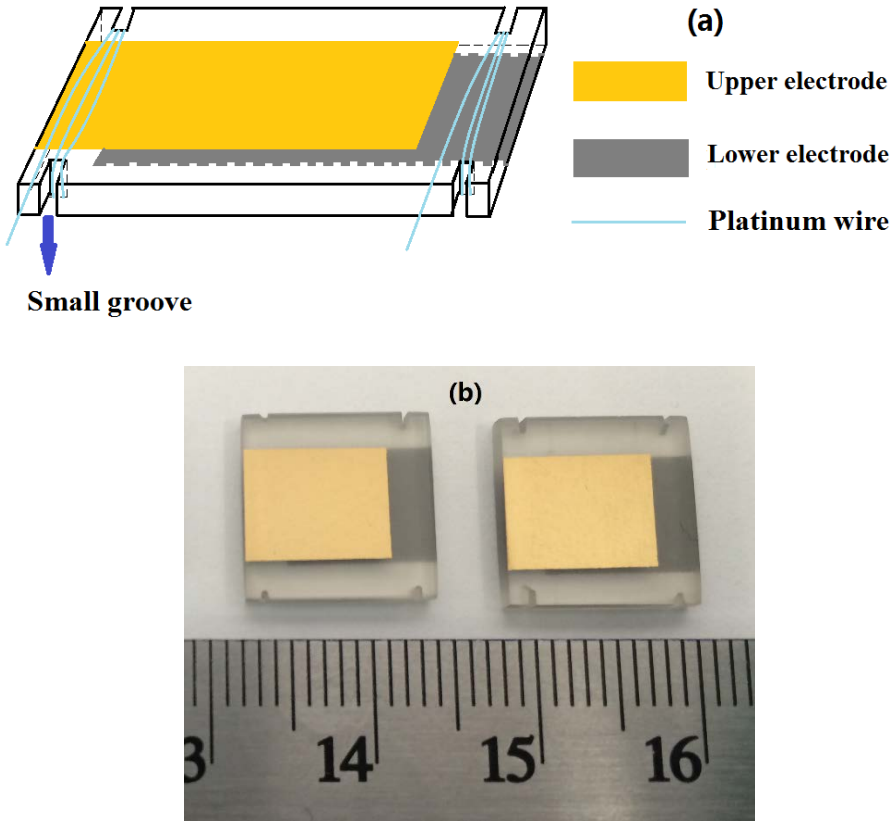

Figure 2-4. (a) Schematic diagram of the grooved sample, (b) photograph of two grooved plate samples.

2.2 METHODS FOR THE DETERMINATION OF THE BASIC PROPERTIES OF CTGS CRYSTALS

2.2.1 General

CTGS crystals belong to the trigonal crystal system and the point group 32, and according to Mason's definition and deduction [28], the dielectric, piezoelectric, and elastic coefficients matrices are as follows:

$$\varepsilon_{ij} = \begin{bmatrix} \varepsilon_{11} & 0 & 0 \\ 0 & \varepsilon_{11} & 0 \\ 0 & 0 & \varepsilon_{33} \end{bmatrix} \tag{2-1}$$

$$d_{ij} = \begin{bmatrix} d_{11} & -d_{11} & 0 & d_{14} & 0 & 0 \\ 0 & 0 & 0 & 0 & -d_{14} & -2d_{11} \\ 0 & 0 & 0 & 0 & 0 & 0 \end{bmatrix} \text{ or } e_{ij} = \begin{bmatrix} e_{11} & -e_{11} & 0 & e_{14} & 0 & 0 \\ 0 & 0 & 0 & 0 & -e_{14} & -e_{11} \\ 0 & 0 & 0 & 0 & 0 & 0 \end{bmatrix} \tag{2-2}$$

$$s_{ij} = \begin{bmatrix} s_{11} & s_{12} & s_{13} & s_{14} & 0 & 0 \\ s_{12} & s_{11} & s_{13} & -s_{14} & 0 & 0 \\ s_{13} & s_{13} & s_{33} & 0 & 0 & 0 \\ s_{14} & -s_{14} & 0 & s_{44} & 0 & 0 \\ 0 & 0 & 0 & 0 & s_{44} & 2s_{14} \\ 0 & 0 & 0 & 0 & 2s_{14} & 2(s_{11}-s_{12}) \end{bmatrix} \text{ or } c_{ij} = \begin{bmatrix} c_{11} & c_{12} & c_{13} & c_{14} & 0 & 0 \\ c_{12} & c_{11} & c_{13} & -c_{14} & 0 & 0 \\ c_{13} & c_{13} & c_{33} & 0 & 0 & 0 \\ c_{14} & -c_{14} & 0 & c_{44} & 0 & 0 \\ 0 & 0 & 0 & 0 & c_{44} & c_{14} \\ 0 & 0 & 0 & 0 & c_{14} & \frac{c_{11}-c_{12}}{2} \end{bmatrix} \tag{2-3}$$

As can be seen above, the d_{ij} and s_{ij} matrix are somewhat different from the e_{ij} and c_{ij} matrix, respectively, because of the definition of the shearing strain adopted. Obviously, the independent dielectric, piezoelectric, and elastic coefficients to be determined are 2, 2 and 6, respectively. Next, the two methods for the determination of these coefficients will be described and explained in detail: one is in the light of the IEEE dynamic methods, while the other is according to Du, Wang, and Uchino's methods.

2.2.2 IEEE dynamic methods for the determination of the real constants

To apply the dynamic methods for crystal resonator characterization, piezoelectric resonators with desirable vibration modes that can be excited by electrical field should be designed and prepared. For the design of the resonators, two basic principles should be followed: the crystal sample-cuts should be as simple as possible to ensure their availability and accuracy; and the electrically excitable vibration modes should be as pure as possible to avoid the coupling and

complexity. Thus, the length-extensional modes of bar resonators have particular significance for the coefficients' determination, due to their simplicity and purity.

For crystals in point group 32, with the four kinds of rectangular bars shown in Figure 2-1: XY, (XY*t*)45°, (XY*t*)-30°, and (XY*t*)-85° cuts, three elastic compliances: s_{11}^E, s_{33}^E, s_{14}^E, and the combination $2s_{13}^E+s_{44}^E$, could be obtained. The specific procedures are as follows: firstly, measuring the electrical admittance (*Y*-θ) of the XY-Cut bars to extract the resonance frequencies (f_r); and then calculating the s_{11}^E according to the following equation:

$$s_{11}^E = s_{22}^E = \frac{1}{4\rho(lf_r)^2} \tag{2-4}$$

where ρ (= 4.61 g/cm^3) is the density of CTGS crystals and *l* is the length of the bars.

Secondly, measuring the *Y*-θ of (XY*t*)45°, (XY*t*)-30°, and (XY*t*)-85° bars and using (2-4) to acquire the $s_{22}^E(45°)$, $s_{22}^E(-30°)$, and $s_{22}^E(-85°)$, respectively. Finally, solving the aforementioned three elastic compliances and one combination through the following equation:

$$s_{22}^E(\theta) = s_{11}^E\cos^4\theta + s_{33}^E\sin^4\theta - 2s_{14}^E\cos^3\theta\sin\theta + (2s_{13}^E + s_{44}^E)\cos^2\theta\sin^2\theta \tag{2-5}$$

In this case, only two elastic compliances are left to be determined: s_{12}^E and s_{13}^E. However, these two elastic compliances couldn't be directly reflected by any pure mode of vibrator and they are relatively small compared to most of others according to Shi's [8] report. Therefore, some indirect methods should be exploited. As we know, the elastic compliance coefficient matrix *s* and the elastic stiffness coefficient matrix *c* are reciprocal:

$$c_{ij} = s_{ij}^{-1} \tag{2-6}$$

So, the following relations could be obtained [22]:

$$2c_{11}=\frac{s_{33}}{\alpha}+\frac{s_{44}}{\beta},\ 2c_{12}=\frac{s_{33}}{\alpha}-\frac{s_{44}}{\beta},\ c_{13}=-\frac{s_{13}}{\alpha},\ c_{14}=-\frac{s_{14}}{\beta},$$
$$c_{33}=\frac{s_{11}+s_{12}}{\alpha},\ c_{44}=\frac{s_{11}-s_{12}}{\beta},\ c_{66}=\frac{c_{11}-c_{12}}{2}=\frac{s_{44}}{2\beta};\quad \textbf{(2-7)}$$
$$where\ \alpha=s_{33}(s_{11}+s_{12})-2s_{13}^2;\ \beta=s_{44}(s_{11}-s_{12})-2s_{14}^2$$

And because $2s_{13}^E+s_{44}^E$ is a known constant, if we gain c_{44}^E and c_{66}^E, s_{12}^E and s_{13}^E would be easily got. The thickness shear mode of Y-cut and Z-cut square-plate resonators could be used to determine c_{66}^E and c_{44}^E, respectively. As long as we measure the impedance (*Z*-θ) or admittance (*Y*-θ) of the plates, extract their resonance frequencies (f_r), and follow the equations:

$$c_{66}^E=4\rho(tf_{r-Y})^2,\ c_{44}^E=4\rho(tf_{r-Z})^2 \quad \textbf{(2-8)}$$

where *t* is the thickness of the plates, and f_{r-Y} and f_{r-Z} are resonant frequencies of Y-cut and Z-cut square-plate vibrators. Thus, all the six elastic compliances coefficients s_{ij}^E have been obtained so far. And all the six elastic stiffness coefficients c_{ij}^E could also be acquired by simply applying (2-7).

The two dielectric coefficients (ε_{11}^T and ε_{33}^T) and the relative ones (ε_{r11}^T and ε_{r33}^T) could be obtained from the capacitances of X-cut and Z-cut square plates by

$$\varepsilon_{11,33}^T=\frac{C_{11,33}\cdot t}{A},\ \varepsilon_{r11,33}^T=\frac{\varepsilon_{11,33}^T}{\varepsilon_0},\ \varepsilon_0\approx 8.85\times10^{-12}\ F/m \quad \textbf{(2-9)}$$

where *C*, *t* and *A* are the low frequency capacitances (measured at 2 kHz), thicknesses, and effective areas of the plates.

The two piezoelectric coefficients (d_{11} and d_{14}, or e_{11} and e_{14}) could be obtained through the admittance measurements of any two kinds of the four rectangular bars shown in Figure 2-1 (here XY, and (XY*t*)45° bars were selected). The relative equations are as follows:

$$\frac{k_{12}^2(\theta)-1}{k_{12}^2(\theta)}=\frac{\tan[\frac{\pi}{2}(f_a(\theta)/f_r(\theta))]}{\frac{\pi}{2}(f_a(\theta)/f_r(\theta))},\quad d_{12}^2(\theta)=k_{12}^2(\theta)\varepsilon_{11}^T s_{22}^E$$
$$d_{12}(\theta)=\frac{-d_{11}(1+\cos 2\theta)+d_{14}\sin 2\theta}{2},\quad e_{nj}=d_{ni}c_{ij}^E \qquad \textbf{(2-10)}$$

where k_{12} is the electromechanical coupling coefficient, and f_r and f_a are the corresponding resonant and anti-resonant frequencies, respectively.

So far, the IEEE dynamic methods for determining all the real dielectric, piezoelectric, and elastic coefficients of CTGS crystals have been fully explained, and the information of the samples and measurements will be summarized in Table 2-1.

Table 2-1. Information of samples and measurements for IEEE dynamic methods.

Sample-cuts	Electric field direction (**n**)	Sample dimension	Measured parameters	Directly related coefficients
X-cut plate	**n**∥x	*l*×*w*×*t*= 12×12×2 mm^3	*C*	ε_{11}^T
Y-cut plate	**n**∥y		*Z-θ*	c_{66}^E
Z-cut plate	**n**⊥z, and **n**∥z		*Y-θ*, *C*	c_{44}^E, ε_{33}^T
XY-cut bar	**n**∥x	*l*×*w*×*t*= 18×5×1 mm^3	*Y-θ*	s_{11}^E, s_{33}^E, s_{14}^E, s_{13}^E, s_{44}^E, d_{11}, and d_{14}
(XY*t*)45° bar				
(XY*t*)-30° bar				
(XY*t*)-85° bar				

a) l,w, and t mean the length, width, and thickness of the samples, respectively.
b) The sample dimensions here are only for reference, and in the calculation processes, the actually measured values were applied.
c) C, Z-θ, and Y-θ represent the capacitance, impedance, and admittance, respectively.
d) Other coefficients which are not included in the "Directly related coefficients" column could be calculated from the included ones.

2.2.3 The methods of Du *et al*. for the determination of the complex coefficients

2.2.3.1 General

Compared to the real parts of the complex coefficients, the imaginary parts are much more difficult to determine, because they are much smaller than the real parts and may be in the same

order as the random errors, and there is little information which is only sensitive to them. Du *et al*. developed an effective method which could subtly extract the complex coefficients from the dynamic behaviors of the impedance or admittance near the resonance, where the information is more dominant than the random errors and with high sensitivity to the desired coefficients [49]. It's worth noting here that the impedance should be measured in the form of resistance (*R*) and reactance (*X*), and the admittance in the form of conductance (*G*) and susceptance (*B*).

The selection of the impedance or admittance measurement is not arbitrary, and it depends on the relationship between the cutting orientation and the electric field direction of the samples. To clear this question, the two directions should be defined first: the cutting orientation is represented by the unit vector **l**, and **l** is along the length direction of the bars and thickness direction of the plates; the electric field direction is denoted by another unit vector **n**, and **n** is perpendicular to the electrode surfaces. Whether the samples are bars or plates, the admittance (*G*-*B*) should be measured when **n** is perpendicular to **l**, and the selection should be the impedance (*R*-*X*) when **n** is parallel to **l** [50].

2.2.3.2 The basic procedure

The complex dielectric coefficients could be expressed by the following equation:

$$\varepsilon_r = \varepsilon_r^{'} - i\varepsilon_r^{''} \qquad \textbf{(2-11)}$$

where ε_r, ε_r', and $\varepsilon_r^{''}$ are the complex dielectric coefficient, its real part, and imaginary part, respectively. The two complex dielectric coefficients could be obtained through the measurement of the capacitances and the dissipations (C_p-D) of X-Cut and Z-cut square plates: the real parts (ε_r') are the same with the real dielectric coefficients acquired through the IEEE dynamic

methods and could be calculated by (2-9), and the imaginary parts ($\varepsilon_r^{''}$) are the products of the real parts and corresponding dissipations:

$$\varepsilon_r^{''} = \varepsilon_r^{'} \cdot D \tag{2-12}$$

And if the capacitances and the dissipations are measured at a low frequency (2 kHz), the complex dielectric coefficients under constant stress (ε_r^T) could be got; if they are measured at a high frequency (20 MHz), the coefficients under constant strain (ε_r^S) would be obtained.

In order to determine the complex piezoelectric and elastic coefficients, Du *et al*. developed their methods based on the general acoustic field equations, piezoelectric constitutive equations, and some necessary mathematical manipulations [50]. Here we will not repeat the derivation process, but will summarize the significant conclusions and clear the specific usage of the methods. According to the electrical conditions and shapes, there are four types of samples: bars with $\mathbf{n} \perp \mathbf{l}$, bars with $\mathbf{n} // \mathbf{l}$, plates with $\mathbf{n} \perp \mathbf{l}$, and plates with $\mathbf{n} // \mathbf{l}$. The equations specifically employed and the parameters finally obtained of these four types of samples are very similar, but with slightly difference. We will elaborate on the method for the first type (bars with $\mathbf{n} \perp \mathbf{l}$), and describe the other three kinds on the basis of it.

Bars with n⊥l:

As previously described, when $\mathbf{n} \perp \mathbf{l}$, the admittance (*G*-*B*) should be measured

$$Y(\omega) = j\omega C \left\{ 1 + k^2 \frac{\tan(\omega \Lambda a)}{\omega \Lambda a} \right\} \tag{2-13}$$

where *k* and *Λ* are some complex constants which are functions of the desired coefficients, and *a* is half of the length of the bars (for plates, *a* is half of the thickness). And to eliminate the frequency dependence of the first term of (2-13), the admittance should be normalized by ω

$$\overline{Y}(\omega)=\frac{Y(\omega)}{\omega}=jC+j\eta\frac{\tan(\omega\Lambda a)}{\omega\Lambda a} \tag{2-14}$$

where

$$\begin{aligned}&\eta=C\cdot k^2,\quad k^2=\frac{d^2}{\varepsilon^T\cdot s^E}\\&A=\frac{\eta}{\omega\Lambda a}=A'+jA'',\quad \Lambda=\sqrt{\rho\cdot s^E}=\Lambda'+j\Lambda''\end{aligned} \tag{2-15}$$

Thus, once the Λ and A are known, the complex elastic and piezoelectric coefficients would be obtained according to (2-15). According to Du's derivation, the ways to solve Λ', Λ'', A' and A'' are as follows:

$$\Lambda'=\frac{1}{4f_{\overline{G}\max}a} \tag{2-16}$$

where $f_{\overline{G}\max}$ is the frequency of the maximum normalized conductance.

$$\begin{aligned}&\frac{\cosh(\pi/q_m)-1}{(1+1/q_m^2)\cosh(\pi/q_m)}-\frac{\pi^2}{8}\left(\frac{f_{\overline{B}\max}-f_{\overline{B}\min}}{f_{\overline{G}\max}}\right)^2=0\\&\Lambda''=sign(f_{\overline{B}\max}-f_{\overline{B}\min})\frac{\Lambda'}{q_m}\end{aligned} \tag{2-17}$$

where $f_{\overline{B}\max}$ and $f_{\overline{B}\min}$ are the frequencies of the maximum and minimum normalized susceptance, and the "$sign(f_{\overline{B}\max}-f_{\overline{B}\min})$" means the sign (plus or minus) of "$(f_{\overline{B}\max}-f_{\overline{B}\min})$". q_m is an intermediate variable which is related to the effective mechanical quality factor and could be solved from (2-17).

$$A'=\frac{1-\cosh(\pi/q_m)}{4\pi\Lambda' a}\frac{\partial\overline{B}}{\partial f}\Big|_{f=f_{\overline{G}\max}}\approx-\frac{\pi}{8a\Lambda' q_m^2}\frac{\partial\overline{B}}{\partial f}\Big|_{f=f_{\overline{G}\max}} \tag{2-18}$$

The determination of A'' is much more difficult and is based on the following complex mathematical operation:

$$\sum_{k=1}^{N}\left(\frac{\partial\overline{G}}{\partial f}(-k)\cdot\alpha(-k)+\frac{\partial\overline{G}}{\partial f}(k)\cdot\alpha(k)\right)=-4\pi a(\Lambda^{'}A^{''}+\Lambda^{''}A^{'})\sum_{K=1}^{N}(\beta(-k)+\beta(-k)) \tag{2-19}$$

where

$$\begin{aligned}&\frac{\partial\overline{G}}{\partial f}(k)=\frac{\partial\overline{G}}{\partial f}(f_{\overline{G}\max}+k\cdot\Delta f)\\&\alpha(k)=[\cos(4\pi(f_{\overline{G}\max}+k\cdot\Delta f)\Lambda^{'}a)+\cosh(4\pi(f_{\overline{G}\max}+k\cdot\Delta f)\Lambda^{''}a)]^2\\&\beta(k)=1+\cos(4\pi(f_{\overline{G}\max}+k\cdot\Delta f)\Lambda^{'}a)\cdot\cosh(4\pi(f_{\overline{G}\max}+k\cdot\Delta f)\Lambda^{''}a)\end{aligned} \tag{2-20}$$

where Δf is the measurement increment step of frequency.

In a word, through the measurements of the capacitance (C), and admittance (G-B), the Λ', $\Lambda^{''}$, A' and $A^{''}$ could be got according to (2-16), (2-17), (2-18), (2-19), and (2-20). And then the complex elastic and piezoelectric coefficients could be obtained through (2-15).

Bars with n//l:

When **n** // **l**, the impedance (R-X) should be measured and normalized by $1/\omega$

$$\begin{aligned}&Z(\omega)=\frac{1}{j\omega C}\left\{1-k^2\frac{\tan(\omega\Lambda a)}{\omega\Lambda a}\right\}\\&\overline{Z}(\omega)=\omega\cdot Z(\omega)=\frac{1}{jC}+j\eta\frac{\tan(\omega\Lambda a)}{\omega\Lambda a}\end{aligned} \tag{2-21}$$

In this case, the definition of the complex constant A is the same with that shown in (2-15), however, the η, k, and Λ will be slightly different:

$$\eta=k^2/C,\quad k^2=\frac{d^2}{\varepsilon^T\cdot s^D},\quad \Lambda=\sqrt{\rho\cdot s^D}=\Lambda^{'}+j\Lambda^{''} \tag{2-22}$$

And by simply substituting the $f_{\overline{G}\max}$, $f_{\overline{B}\max}$ and $f_{\overline{B}\min}$ in (2-16), (2-17), (2-18), (2-19), and (2-20) with $f_{\overline{R}\max}$, $f_{\overline{X}\max}$ and $f_{\overline{X}\min}$, respectively, the new Λ', $\Lambda^{''}$, A' and $A^{''}$ could be obtained. Thus, the complex elastic and piezoelectric coefficients could be got through (2-15) and (2-22).

Plates with n⊥l:

The methods for the determination of the complex elastic and piezoelectric coefficients of plate-samples with $\mathbf{n} \perp \mathbf{l}$ are almost the same with those of bar-samples with $\mathbf{n} \perp \mathbf{l}$, except the definitions of k and Λ:

$$k^2 = \frac{e^2}{\varepsilon^S \cdot c^E}, \quad \Lambda = \sqrt{\rho / c^E} = \Lambda' + j\Lambda'' \tag{2-23}$$

Plates with n//l:

Similarly, by following the methods developed for bar-samples with $\mathbf{n} // \mathbf{l}$, we could determine the desired complex coefficients under this situation, and only need to employ the new expressions of k and Λ:

$$k^2 = \frac{e^2}{\varepsilon^S \cdot c^D}, \quad \Lambda = \sqrt{\rho / c^D} = \Lambda' + j\Lambda'' \tag{2-24}$$

To make the procedure clearer, the relationships between the sample types and the expressions of related parameters will be summarized in Table 2-2.

Table 2-2. The relationships between sample types and complex parameters.

Electrical condition	Sample type	Measured parameters	Λ	k^2	η	A	Related coefficients
n⊥l	Bar	C_p-D, G-B	$\Lambda = \sqrt{\rho \cdot s^E}$	$k^2 = \frac{d^2}{\varepsilon^T \cdot s^E}$	$\eta = C \cdot k^2$	$A = \frac{\eta}{\omega \Lambda a}$	ε^T, s^E and d
	Plate		$\Lambda = \sqrt{\rho / c^E}$	$k^2 = \frac{e^2}{\varepsilon^S \cdot c^E}$			ε^S, c^E and e
n‖l	Bar	C_p-D, R-X	$\Lambda = \sqrt{\rho \cdot s^D}$	$k^2 = \frac{d^2}{\varepsilon^T \cdot s^D}$	$\eta = k^2 / C$		ε^T, s^D and d
	Plate		$\Lambda = \sqrt{\rho / c^D}$	$k^2 = \frac{e^2}{\varepsilon^S \cdot c^D}$			ε^S, c^D and e

a) C_p, D, G, B, R, and X represent the capacitance, dissipations, conductance, susceptance, resistance, and reactance, respectively.
b) Λ, k^2, η, and A are complex constants which are known functions of the desired coefficients.
c) The superscripts T, S, E and D denote that the coefficients are obtained at constant stress, strain, electric field, and electric displacement, respectively.

2.2.3.3 The specific design

The foregoing part has shown which form of complex coefficients could be obtained through the different samples with distinct electrical conditions. Following that, it is necessary to illustrate samples with which kinds of orientations are needed to determine the six elastic and two piezoelectric coefficients. Similar to the design for the IEEE dynamic methods, in this process, the simpler sample-cuts with purer vibration modes also have the higher priority. In order to determine the required orientations, it is necessary to introduce four matrices: **L**, **M**, **A**, and **B** [50, 190]. **L** and **M** are two intermediate matrices and defined as follows:

$$L=\begin{bmatrix} l_1 & 0 & 0 & 0 & l_3 & l_2 \\ 0 & l_2 & 0 & l_3 & 0 & l_1 \\ 0 & 0 & l_3 & l_2 & l_1 & 0 \end{bmatrix}$$
$$M=\begin{bmatrix} l_1 & 0 & 0 \\ 0 & l_2 & 0 \\ 0 & 0 & l_3 \end{bmatrix}\begin{bmatrix} l_1^2-1 & l_2^2 & l_3^2 & l_2l_3 & l_1l_3 & l_1l_2 \\ l_1^2 & l_2^2-1 & l_3^2 & l_2l_3 & l_1l_3 & l_1l_2 \\ l_1^2 & l_2^2 & l_3^2-1 & l_2l_3 & l_1l_3 & l_1l_2 \end{bmatrix} \quad \textbf{(2-25)}$$

where l_1, l_2, and l_3 are the three components of the cutting orientation's unit vector **l**: **l**=[l_1 l_2 l_3]^t. **A** and **B** could provide the decisive information for the design and are defined as follows:

For bars with **n** $\perp$ **l**:

$$A=(L-M)s^E(L-M)^t, \quad B=(L-M)d^tn \quad \textbf{(2-26)}$$

For plates with **n** $\perp$ **l**:

$$A=Lc^EL^t, \quad B=Le^tn \quad \textbf{(2-27)}$$

For bars with **n** // **l**:

$$A=(L-M)s^E(L-M)^t-BB^t/\varepsilon_n, \quad B=(L-M)d^tn \quad \textbf{(2-28)}$$

For plates with **n** // **l**:

$$A=Lc^EL^t+BB^t/\varepsilon_n, \quad B=Le^tn \quad \textbf{(2-29)}$$

where for bars ε_n=$\mathbf{n}^t\varepsilon^T\mathbf{n}$, and for plates ε_n=$\mathbf{n}^t\varepsilon^S\mathbf{n}$. Matrix **A** is associated with the complex elastic and piezoelectric coefficients and could indicate the possible vibration modes, while **B** could illustrate how to electrically excite the different vibration modes. Next, we will minutely explain the design with the aid of matrix **A** and **B**.

X-cut plate:

For X-cut plates, **l**=[1 0 0]^t, when **n** // **l**, **n**=[1 0 0]^t, the matrices **A** and **B** are as follows:

$$A=\begin{bmatrix} c_{11}^E+e_{11}^2/\varepsilon_{11}^S & 0 & 0 \\ 0 & c_{66}^E & c_{14}^E \\ 0 & c_{14}^E & c_{44}^E \end{bmatrix},\quad B=\begin{bmatrix} e_{11} & 0 & 0 \\ 0 & -e_{11} & 0 \\ 0 & -e_{14} & 0 \end{bmatrix}\begin{bmatrix}1\\0\\0\end{bmatrix}=\begin{bmatrix}e_{11}\\0\\0\end{bmatrix} \tag{2-30}$$

A indicates that there are one pure extensional mode (c_{11}^E), and two coupled shear modes (c_{66}^E and c_{14}^E, c_{14}^E and c_{44}^E). And **B** implies that the pure extensional mode could be excited by the electric field in X direction. It is worth noting that in this case, the c_{11}^D would be directly determined, not c_{11}^E, because:

$$c_{11}^E+e_{11}^2/\varepsilon_{11}^S=c_{11}^E(1+\frac{e_{11}^2}{\varepsilon_{11}^S c_{11}^E})=c_{11}^D \tag{2-31}$$

However, once c_{11}^D and e_{11} were obtained, c_{11}^E would be easily got from (2-31). Thus, X-cut plates with **n** // **l** could provide the information for determining c_{11}^D, $c_{11}^E$and e_{11}.

Similarly, when **n**⊥**l**, and **n**=[0 1 0]^t, c_{66}^E and c_{14}^E could be obtained, however they are not extracted from the pure vibration mode, so this will not be adopted. And when **n**⊥**l**, and **n**=[0 0 1]^t, no vibration could be excited.

Y-cut plate:

For Y-cut plates, **l**=[0 1 0]^t, when **n** // **l**, **n**=[0 1 0]^t, the matrices **A** and **B** will be:

$$A=\begin{bmatrix} c_{66}^{E}+e_{11}^{2}/\varepsilon_{11}^{S} & 0 & 0 \\ 0 & c_{11}^{E} & -c_{14}^{E} \\ 0 & -c_{14}^{E} & c_{44}^{E} \end{bmatrix},\quad B=\begin{bmatrix} 0 & -e_{11} & 0 \\ -e_{11} & 0 & 0 \\ e_{14} & 0 & 0 \end{bmatrix}\begin{bmatrix} 0 \\ 1 \\ 0 \end{bmatrix}=\begin{bmatrix} -e_{11} \\ 0 \\ 0 \end{bmatrix} \tag{2-32}$$

A shows there are one pure shear mode (c_{66}^{E}), and two mixed extensional shear modes (c_{11}^{E} and c_{14}^{E}, c_{14}^{E} and c_{44}^{E}). And **B** illustrates that the pure shear mode could be excited by the electric field in Y direction. Thus, Y-cut plates with **n** // **l** could be used to determine c_{66}^{D}, c_{66}^{E} and e_{11}.

Z-cut plate:

For Z-cut plates, **l**=[0 0 1]^{t}, when **n**⊥**l,** and **n**=[1 0 0]^{t}, the matrices **A** and **B** are:

$$A=\begin{bmatrix} c_{44}^{E} & 0 & 0 \\ 0 & c_{44}^{E} & 0 \\ 0 & 0 & c_{33}^{E} \end{bmatrix},\quad B=\begin{bmatrix} 0 & -e_{14} & 0 \\ e_{14} & 0 & 0 \\ 0 & 0 & 0 \end{bmatrix}\begin{bmatrix} 1 \\ 0 \\ 0 \end{bmatrix}=\begin{bmatrix} 0 \\ e_{14} \\ 0 \end{bmatrix} \tag{2-33}$$

Obviously, there are two pure shear modes (c_{44}^{E}) and one pure extensional mode (c_{33}^{E}), and the pure shear modes could be excited by the electric field in X (or Y) direction. Therefore, Z-cut plates with **n**⊥**l** could be used for the determination of c_{44}^{E} and e_{14}.

XY-cut bar:

As we know, **l**=[0 1 0]^{t}, when **n**⊥**l**, and **n**=[1 0 0]^{t}, the matrices **A** and **B** could be expressed as:

$$A=\begin{bmatrix} s_{66}^{E} & 0 & 0 \\ 0 & s_{22}^{E} & -s_{14}^{E} \\ 0 & -s_{14}^{E} & s_{44}^{E} \end{bmatrix},\quad B=\begin{bmatrix} 0 & -2d_{14} & 0 \\ -d_{11} & 0 & 0 \\ d_{14} & 0 & 0 \end{bmatrix}\begin{bmatrix} 1 \\ 0 \\ 0 \end{bmatrix}=\begin{bmatrix} 0 \\ -d_{11} \\ d_{14} \end{bmatrix} \tag{2-34}$$

As can be seen from (2-34), there are one pure shear mode and two mixed extensional shear modes, however, the pure shear mode couldn't be excited by the electric field in X direction. Though the two mixed extensional shear modes are not pure, the measured admittance signals are clear and strong. Hence the XY-cut bars with **n**⊥**l** were employed to obtain s_{22}^{E}

(=s_{11}^E), s_{44}^E, and d_{14}. One thing to note is s_{66}^E could be got through XY-cut bars with **n**‖**l**, however, the impedance signals are unstable because the electrode surfaces are relative small (5 mm ×1 mm) which results in the instability of the electric field. Thus, XY-cut bars with **n**‖**l** are not exploited.

(XYt)-85° bar:

The (XY*t*)-85° bars are designed to approximately determine s_{33}^E, because it couldn't be directly and accurately obtained by any type of sample. For this kind of sample:

$$l = [0 \quad \cos 85^\circ \quad -\sin 85^\circ] \approx [0 \quad \frac{1}{10} \quad 1] \tag{2-35}$$

And

$$A \approx \begin{bmatrix} s_{44}^E & 0 & 0 \\ 0 & s_{44}^E & 0 \\ 0 & 0 & s_{33}^E \end{bmatrix}, \quad B \approx \begin{bmatrix} 0 & -0.2d_{11} - d_{14} & 0 \\ -0.2d_{11} + d_{14} & 0 & 0 \\ 0.01d_{11} & 0 & 0 \end{bmatrix} \begin{bmatrix} 1 \\ 0 \\ 0 \end{bmatrix} \approx \begin{bmatrix} 0 \\ -0.2d_{11} + d_{14} \\ 0.01d_{11} \end{bmatrix} \tag{2-36}$$

Through the above mentioned five types of samples, all the complex elastic and piezoelectric coefficients could be obtained. In summary, by measuring the X-cut, Y-cut, and Z-cut plate-samples, c_{11}^D, c_{66}^D, c_{44}^E, e_{11}, and e_{14}could be determined. Together with the ε^S, c_{11}^E and c_{66}^E could be calculated through (2-31). At the same time, we could know s_{22}^E, s_{44}^E, and s_{33}^E from the measurements of XY-cut and (XY*t*)-85° bars. Then, the remaining s_{ij}^E and c_{ij}^E could be got by applying (2-7). Finally, the d_{11} and d_{14} could be obtained by

$$d_{nj} = e_{ni} s_{ij}^E \tag{2-37}$$

The information of the samples and measurements will be summarized in Table 2-3.

Table 2-3. Information of samples and measurements for the methods of Du *et al*.

Sample-cuts	Electric field direction (**n**)	Sample dimension	Measured parameters	Directly related coefficients
X-cut plate	**n**∥x	$l\times w\times t=$ $12\times12\times2$ mm^3	C, R-X	ε_{11}^{T}, ε_{11}^{S}, c_{11}^{D}, and e_{11}
Y-cut plate	**n**∥y		R-X	c_{66}^{D}, and e_{11}
Z-cut plate	**n**∥z, and **n**⊥z		C, G-B	ε_{33}^{T}, ε_{33}^{S}, c_{44}^{E}, and e_{14}
XY-cut bar	**n**∥x	$l\times w\times t=$ $18\times5\times1$ mm^3	G-B	s_{22}^{E}, s_{44}^{E}, and d_{14}
(XYt)-85° bar				s_{33}^{E}

a) l,w, and t mean the length, width, and thickness. C, R-X, and G-B represent the capacitance, impedance, and admittance, respectively.
b) Other coefficients which are not included in the "Directly related coefficients" column could be calculated from the included ones.

2.3 RESULTS AND DISCUSSION

According to the methods mentioned above, all the real and complex dielectric, piezoelectric, and elastic coefficients of CTGS single crystals, and their temperature behaviors were determined. To avoid the possible confusion resulting from the disunity of the symbols, we will unify their forms. For example, the s_{ij}^{E} is used to represent the real elastic compliance coefficients at constant electric field, and (s_{ij}^{E})', (s_{ij}^{E})" are employed to denote the real and imaginary parts of the corresponding complex coefficients, respectively. The notations of other coefficients are similar to this one. In the following figures in this chapter, when the real and imaginary parts of the complex coefficients are with the same sign (both are positive or negative), "(i)" will be marked after the notations of the imaginary parts, otherwise, "(-i)" will be applied. In the figures which possess double Y axes, there are some cross or closely spaced lines. In order to avoid the confusion, the blue circles and arrows will be employed to specify which Y axis they are belonging to. Based on the fact that part of the coefficients are positive and the others are negative, and the symbols only represent the directions of the relative effects, which

are independent of the size of the values, all the “absolute values” were considered when talking about the trends with temperature.

2.3.1 Dielectric coefficients

Figure 2-5 presents the variations of the dielectric coefficients ε_r^T, $(\varepsilon_r^T)'$, $(\varepsilon_r^T)''$ as a function of temperature. According to the definition of the “complex dielectric coefficient”, its real part $(\varepsilon_r^T)'$ is equal to the real dielectric coefficient ε_r^T. As observed in Figure 2-5, the ε_{r11}^T and $(\varepsilon_{r11}^T)'$ (the closed red circles) increase from 22.33 to 43.31 as the temperature gradually varies from 21°C to 800°C, while the ε_{r33}^T and $(\varepsilon_{r33}^T)'$ (the closed blue squares) increase from 23.42 to 41.16. And the absolute values of $(\varepsilon_{r11}^T)''$ (the open red circles) and $(\varepsilon_{r33}^T)''$ (the open blue squares) rise from 0.053 to 228.85, and from 0.062 to 142.64, respectively. The increasing rates for all the ε_r^T, $(\varepsilon_r^T)'$, $(\varepsilon_r^T)''$ are relatively small when the temperature is lower than 400°C, while they become quite large after 400°C, especially the imaginary parts $(\varepsilon_{r11}^T)''$ and $(\varepsilon_{r33}^T)''$, implying that the conductivity of CTGS crystals will change significantly when the temperature is higher than 400°C. In addition, compared to the ε_{r33}^T and $(\varepsilon_{r33}^T)''$, the ε_{r11}^T and $(\varepsilon_{r11}^T)''$ increase slightly faster. Moreover, the dielectric losses $tan\delta=(\varepsilon_r^T)''/(\varepsilon_r^T)'$ from room temperature to 800°C are determined and presented in Figure 2-6, which show more intuitively the changes of losses with temperature. Under high temperatures (>500°C), the loss in X direction (about 5.3 at 800°C) grows faster than that in Z direction (about 3.5 at 800°C). Compared to PZT ceramic, the loss of which is typically in the range of 2 to 5 at 500°C, the CTGS crystals possess lower high-temperature loss, indicating the higher potential of CTGS for application at high temperatures.

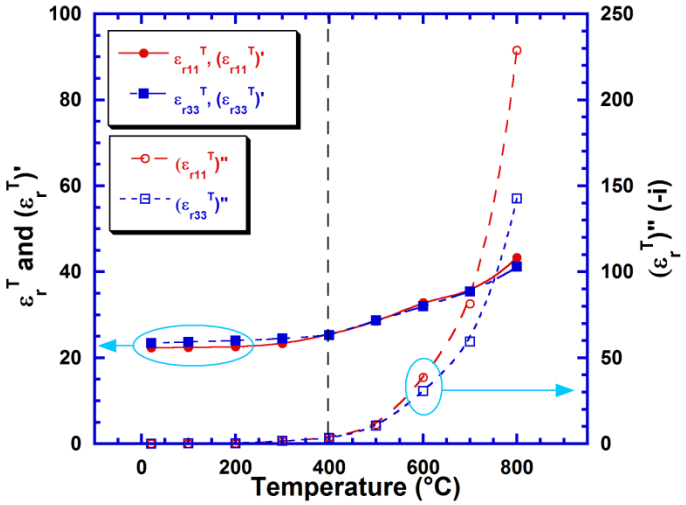

Figure 2-5. The variations of the real and complex dielectric coefficients of CTGS as a function of temperature.

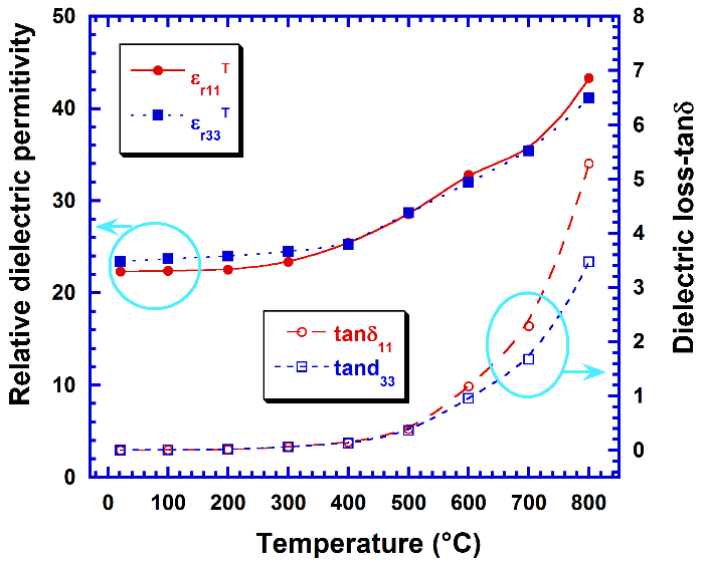

Figure 2-6. Relative permittivity and dielectric loss of CTGS as a function of temperature.

2.3.2 Piezoelectric coefficients

The variations of the piezoelectric coefficients d, d', and d'' as a function of temperature are shown in Figure 2-7. As can be seen, the absolute values of d_{11} (the closed red circles), d'_{11} (the closed blue squares), and d''_{11} (the open blue squares) range from 5.18 to 6.41, from 4.75 to 5.89, and from 0.26 to 0.32 pC/N, respectively, with slight increasing trends. Similarly, d_{14} (the closed brown triangles), d'_{14} (the closed black rhombi), and d''_{14} (the open black rhombi) vary from 11.14 to 12.54, from 10.01 to 11.38, and from 0.54 to 0.62 pC/N, respectively. Generally, these piezoelectric coefficients stay relatively stable over a wide range of temperature. Moreover, the absolute values of d_{11} and d_{14} are a little larger than those of d'_{11} and d'_{14}, respectively, which is in good agreement with Du's results on PZT ceramics and illustrates that the neglect of the dissipations would result in the overestimation of the piezoelectric coefficients [49].

Figure 2-8 exhibits the changes of another form of piezoelectric coefficients e, e', and e'' with temperature. Similar to d, d', and d'', e, e', and e'' also remain relatively stable from 21°C to 800°C: the absolute values of e_{11} (the closed red circles), e'_{11} (the closed blue squares), and e''_{11} (the open blue squares) range from 0.46 to 0.55, from 0.38 to 0.45, and from 2.0×10^{-4} to 2.9×10^{-4} C/m^2, respectively; and e_{14} (the closed brown triangles), e'_{14} (the closed black rhombi), and e''_{14} (the open black rhombi) change from 0.50 to 0.57, from 0.43 to 0.48, and from 9.5×10^{-5} to 1.5×10^{-4} C/m^2, respectively. Analogously, the absolute values of e_{11} and e_{14} are larger than those of e'_{11} and e'_{14}, respectively, which further supports the previous inference.

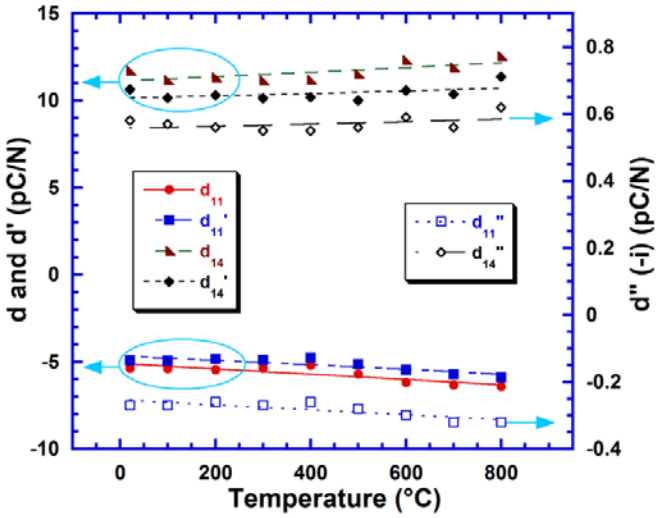

Figure 2-7. The variations of the real and complex piezoelectric coefficients *d*, *d′*, and *d″* of CTGS as a function of temperature.

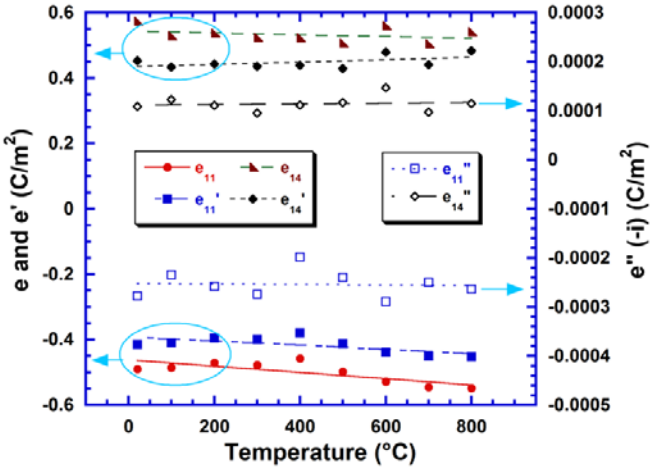

Figure 2-8. The variations of the real and complex piezoelectric coefficients *e*, *e′*, and *e″* of CTGS as a function of temperature.

2.3.3 Elastic coefficients

Figure 2-9 gives the temperature behaviors of two series of elastic compliance coefficients: s_{11}^E, $(s_{11}^E)'$, $(s_{11}^E)''$; and s_{33}^E, $(s_{33}^E)'$, $(s_{33}^E)''$, which are directly associated with the two extensional vibration modes. All of the six coefficients are increasing somewhat with the elevated temperature, however, the s_{11}^E (the closed red circles), $(s_{11}^E)'$ (the closed blue squares), and $(s_{11}^E)''$ (the open blue squares) exhibit excellent linearity, while s_{33}^E (the closed brown triangles), $(s_{33}^E)'$ (the closed black rhombi), and $(s_{33}^E)''$ (the open black rhombi) change nonlinearly. The fact that applying the (XY*t*)-85° bar-samples to approximately determine them should be partly responsible for their nonlinear performance. The increments of s_{11}^E, $(s_{11}^E)'$, and $(s_{11}^E)''$ values from 21°C to 800°C are about 7.8%, 8.2%, and 7.5%, respectively. Additionally, different with the piezoelectric coefficients d and d' discussed above, s_{11}^E and s_{33}^E are smaller than $(s_{11}^E)'$ and $(s_{33}^E)'$, respectively, which to some extent points out that the ignorance of the dissipations would have an opposite effect on the elastic compliance coefficients (will be further proved by most of other elastic compliance coefficients, except s_{12}^E and $(s_{12}^E)'$).

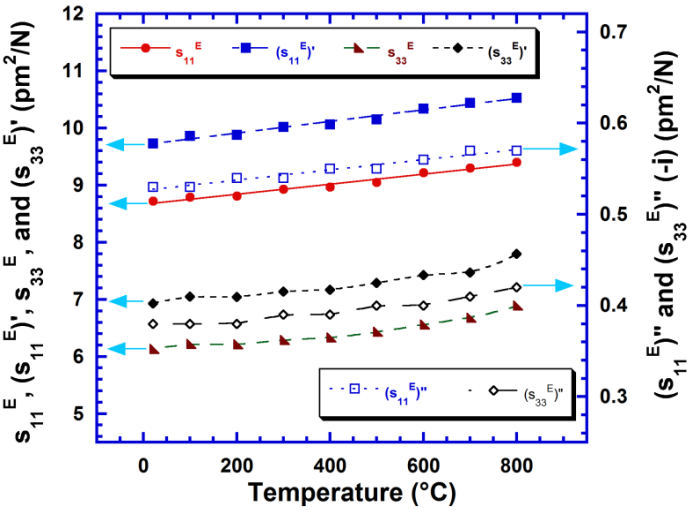

Figure 2-9. Temperature behaviors of elastic compliance coefficients s_{11} and s_{33} series of CTGS.

The temperature behaviors of the analogous two series of elastic stiffness coefficients: c_{11}^E, $(c_{11}^E)'$, $(c_{11}^E)''$; and c_{33}^E, $(c_{33}^E)'$, $(c_{33}^E)''$ are shown in Figure 2-10. As can be observed, c_{11}^E, $(c_{11}^E)'$, and $(c_{11}^E)''$ decrease with perfect linearity as the temperature goes up, and the variations are -4.9%, -6.6%, and -6.6%, respectively. c_{33}^E, $(c_{33}^E)'$, and $(c_{33}^E)''$ also exhibit negative temperature coefficients, however, their values decline nonlinearly. Due to most of the s_{ij}^E are smaller than $(s_{ij}^E)'$, and the s^E matrix and c^E matrix are reciprocal, it is a credible inference that c_{ij}^E would be larger than $(c_{ij}^E)'$, which is supported here by c_{11}^E, $(c_{11}^E)'$ and c_{33}^E, $(c_{33}^E)'$, and would be further proved by most of other elastic stiffness coefficients, except c_{14}^E and $(c_{14}^E)'$.

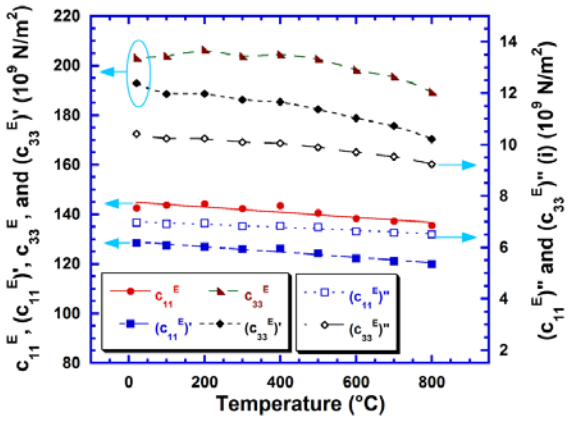

Figure 2-10. Temperature behaviors of elastic stiffness coefficients c_{11} and c_{33} series of CTGS.

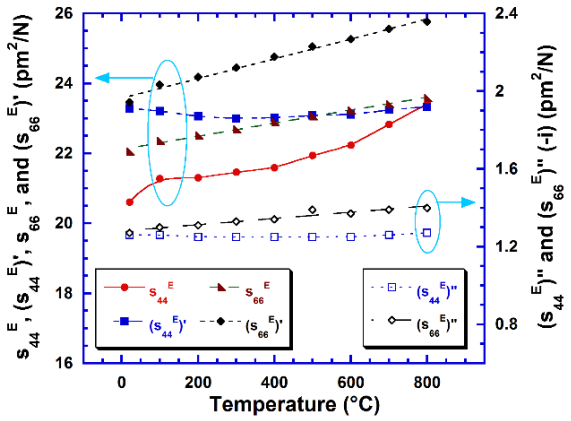

Figure 2-11. Temperature behaviors of elastic compliance coefficients s_{44} and s_{66} series of CTGS.

Figure 2-11 presents the pure shear vibration modes related elastic compliance coefficients: s_{44}^E, $(s_{44}^E)'$, $(s_{44}^E)''$; and s_{66}^E, $(s_{66}^E)'$, $(s_{66}^E)''$. The absolute values of s_{44}^E, $(s_{44}^E)'$, and $(s_{44}^E)''$ range from 20.61 to 23.41, from 23.00 to 23.33, and from 1.25 to 1.27 pm^2/N, respectively. Because of s_{44}^E was not directly obtained through the measurement of a single type of sample, and $(s_{44}^E)'$ was determined through the mixed shear modes (coupled with $(s_{14}^E)'$), their

regularity is not obvious. In contrast, s_{66}^{E}, $(s_{66}^{E})'$, and $(s_{66}^{E})''$ increase linearly from 22.05 to 23.58, from 23.46 to 25.77, and from 1.27 to 1.40 pm^2/N, respectively.

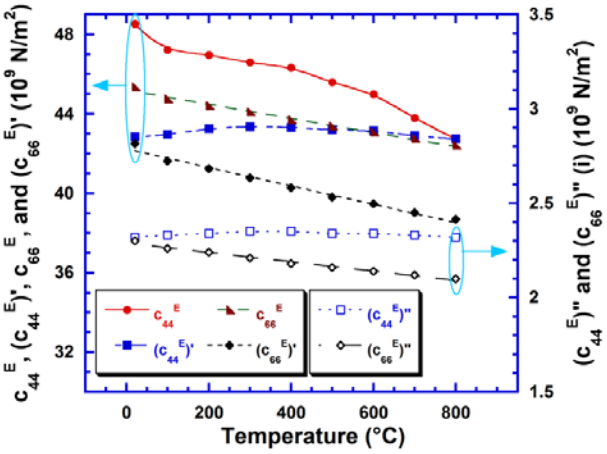

Figure 2-12. Temperature behaviors of elastic stiffness coefficients $\boldsymbol{c_{44}}$ and $\boldsymbol{c_{66}}$ series of CTGS.

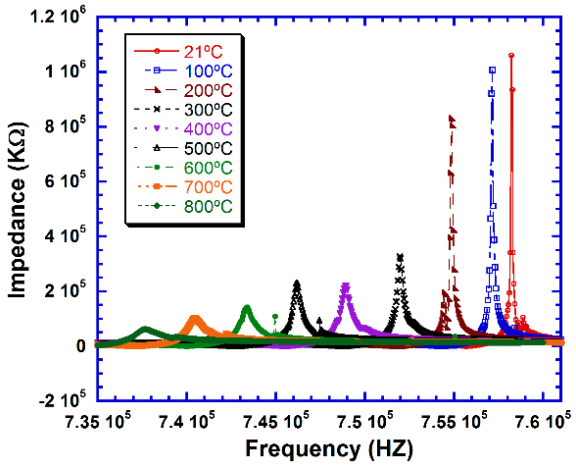

Figure 2-13. The impedance spectrums of one Y-cut CTGS plate sample over the tested temperature range.

The variations of the related elastic stiffness coefficients: c_{44}^E, $(c_{44}^E)'$, $(c_{44}^E)''$; and c_{66}^E, $(c_{66}^E)'$, $(c_{66}^E)''$ as a function of temperature could be seen in Figure 2-12. As the temperature increases from 21°C to 800°C, c_{44}^E, $(c_{44}^E)'$, and $(c_{44}^E)''$ vary nonlinearly from 48.53 to 42.73, from 43.35 to 42.73, and from 2.35 to 2.32 $\times 10^9$ N/m^2, respectively. However, c_{66}^E, $(c_{66}^E)'$, and $(c_{66}^E)''$ decrease linearly from 45.35 to 42.41, from 42.50 to 38.70, and from 2.30 to 2.10 $\times 10^9$ N/m^2, respectively. They were determined through the Z-cut and Y-cut plate-samples, respectively, which reflects that the linearity of Y-cut plate-samples' temperature behaviors is much better than that of Z-cut plate-samples'. The impedance spectrums of one Y-cut plate sample over the tested temperature range are exhibited in Figure 2-13, which not only shows the excellent linearity temperature behavior of Y-cut sample, but also reveals that the high temperature will weaken the amplitude and sharpness of the resonant peaks.

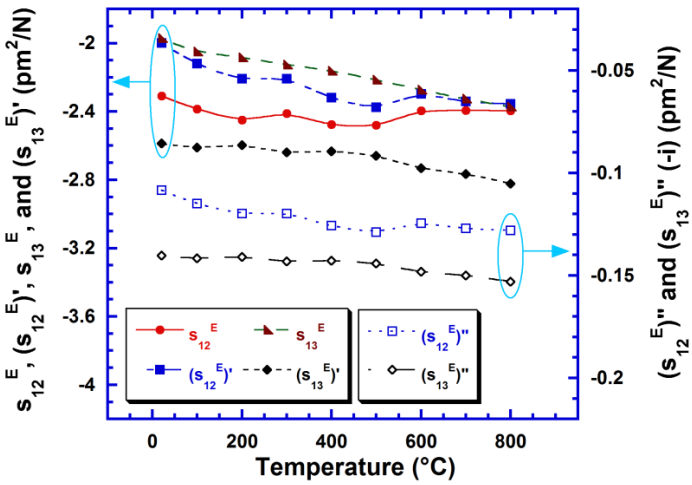

Figure 2-14. Temperature behaviors of elastic compliance coefficients s_{12} and s_{13} series of CTGS.

Figure 2-14 shows the temperature behaviors of s_{12}^E, $(s_{12}^E)'$, $(s_{12}^E)''$; and s_{13}^E, $(s_{13}^E)'$, $(s_{13}^E)''$. As the temperature rises, all their absolute values present a slight increase, however, the trends are less obvious and erratic. This is understandable: firstly, because they were determined on the basis of some other already obtained coefficients, which means they were affected by more errors; and secondly, because their absolute values are relatively small, which makes they were more vulnerable to the errors. The ranges of their absolute values are 2.31~2.48, 2.00~2.38, 0.11~0.13, 1.97~2.37, 2.59~2.82, and 0.14~0.15 pm^2/N, respectively. Similarly, the temperature behaviors of c_{12}^E, $(c_{12}^E)'$, $(c_{12}^E)''$; and c_{13}^E, $(c_{13}^E)'$, $(c_{13}^E)''$ could be found in Figure 2-15. And their ranges are 50.74~56.38, 42.60~45.69, 2.31~2.48, 62.52~68.37, 58.84~64.19, and 3.19~3.48 $\times 10^9$ N/m^2, respectively.

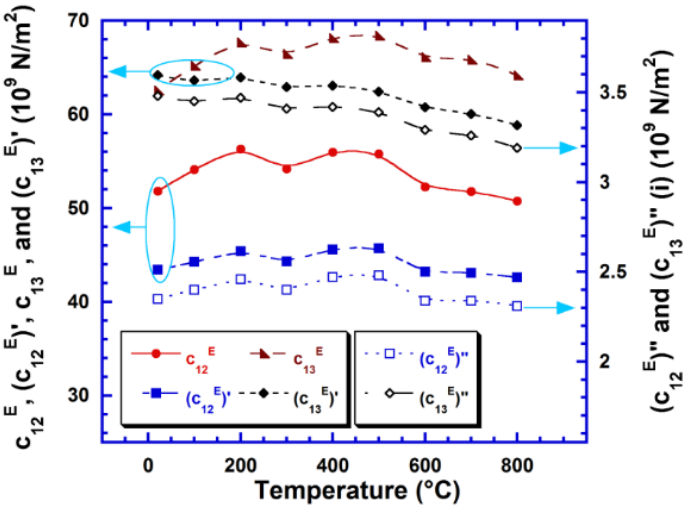

Figure 2-15. Temperature behaviors of elastic stiffness coefficients $\boldsymbol{c_{12}}$ and $\boldsymbol{c_{13}}$ series of CTGS.

Figure 2-16 and Figure 2-17exhibit the temperature performance of s_{14}^E, $(s_{14}^E)'$, $(s_{14}^E)''$, and c_{14}^E, $(c_{14}^E)'$, $(c_{14}^E)''$, respectively, and their absolute values' ranges are 0.092~0.119, 0.117~0.123,

0.0063~0.0066 pm^2/N, and 0.397~0.407, 0.406~0.426, 0.022~0.023 $\times 10^9$ N/m^2. They all possess positive temperature coefficients, and the complex coefficients ($(s_{14}^E)'$, $(s_{14}^E)''$, and $(c_{14}^E)'$, $(c_{14}^E)''$) show better linearity than the corresponding real ones (s_{14}^E and c_{14}^E) owing to the complex ones were obtained more directly (through XY-cut bars).

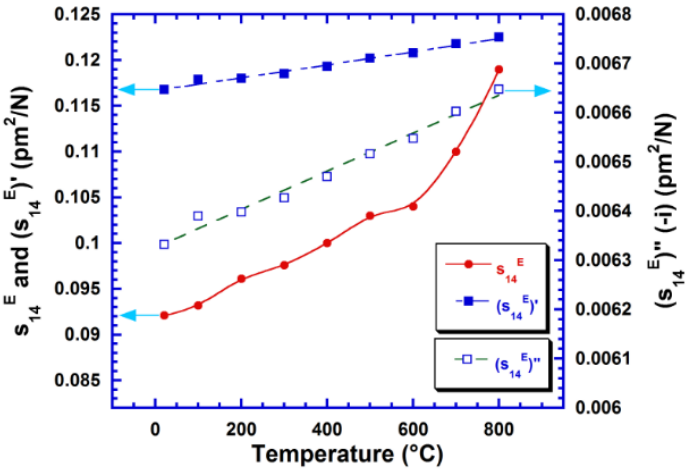

Figure 2-16. Temperature behaviors of elastic compliance coefficients s_{14} series of CTGS.

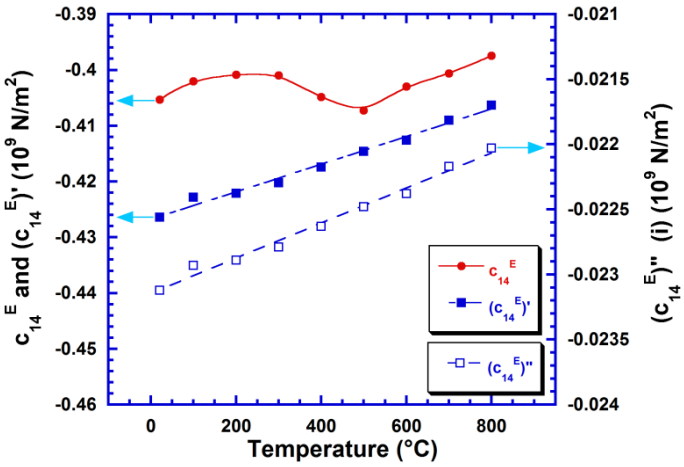

Figure 2-17. Temperature behaviors of elastic stiffness coefficients c_{14} series of CTGS.

The foregoing mentioned that Shi *et al.* [191] had reported all the real dielectric, piezoelectric, and elastic coefficients of CTGS single crystals at ambient temperature. Table 2-4 will compare their results with those obtained in this work at three selected points: 21°C, 400°C, and 800°C. Though the orientations of the applied samples and the procedures of determining the coefficients are with significant difference, most of the coefficients determined in this work at 21°C are quite close to those in Shi's report, which demonstrates the high degree of the applicability of the methods and designs developed in this paper. Besides the orientations and procedures, there are some other factors which will also result in different results: the different crystals grown conditions, e.g., the pulling rate and rotation rate; the different details of the sample preparation, e.g., the materials and thicknesses of the electrodes, and the dimensions of the samples. The little difference between the results in these two work could be understandable when considering these factors.

Table 2-4. The summary of the dielectric, piezoelectric, and elastic coefficients obtained in this work at three selected points (21°C, 400°C, and 800°C), and comparison with the already known results.

Data sources	Shi *et al.*[8]	This work					
Temperature	RT	21 °C		400 °C		800 °C	
Data types	Real	Real	Complex	Real	Complex	Real	Complex
ε_{r11}^{T}	18.15	22.33	22.33-i0.053	25.43	25.43-i3.84	43.31	43.31-i228.85
ε_{r33}^{T}	23.74	23.42	23.42-i0.062	25.25	25.25-i3.28	41.16	41.16-142.62
d_{11}	-4.58	-5.35	-4.92+i0.27	-5.18	-4.75+i0.26	-6.41	-5.89+i0.32
d_{14}	10.43	11.72	10.65-i0.58	11.19	10.19-i0.55	12.54	11.38-i0.62
e_{11}	-0.41	-0.49	-0.41+i0.00028	-0.46	-0.38+i0.00020	-0.55	-0.45+0.00026
e_{14}	0.42	0.57	0.45-i0.00011	0.52	0.44-i0.00011	0.54	0.48-i0.00011
s_{11}^{E}	9.28	8.72	9.73-i0.53	8.97	10.06-i0.55	9.40	10.53-i0.57
s_{33}^{E}	6.56	6.13	6.93-i0.38	6.33	7.17-i0.39	6.89	7.80-i0.42
s_{44}^{E}	24.47	20.61	23.28-i1.26	21.59	23.02-i1.25	23.41	23.33-i1.27
s_{66}^{E}	22.16	22.05	23.46-i1.27	22.89	24.76-i1.34	23.58	25.77-i1.40
s_{12}^{E}	-1.80	-2.31	-2.00+i0.11	-2.47	-2.32+i0.13	-2.40	-2.36+i0.13
s_{13}^{E}	-1.88	-1.97	-2.59+i0.14	-2.16	-2.63+i0.14	-2.37	-2.82+i0.15
s_{14}^{E}	-0.12	0.092	0.12-i0.0063	0.10	0.12-i0.0065	0.12	0.12-i0.0066
c_{11}^{E}	123.2	142.6	128.4+i6.96	143.44	126.1+i6.84	135.6	120.0+i6.50
c_{33}^{E}	178.1	203.3	192.9+i10.42	204.6	185.4+i10.05	189.3	170.4+i9.24
c_{44}^{E}	40.9	48.53	42.83+i2.32	46.33	43.31+i2.35	42.73	42.73+i2.32
c_{66}^{E}	44.9	45.35	42.50+i2.30	43.70	40.28+i2.18	42.41	38.70+i2.10
c_{12}^{E}	33.0	51.91	43.41+i2.35	56.04	45.58+i2.47	50.74	42.60+i2.31
c_{13}^{E}	44.8	62.52	64.19+i3.48	68.13	63.06+i3.42	64.14	58.84+i3.19
c_{14}^{E}	0.44	-0.41	-0.43-i0.023	-0.40	-0.42-i0.023	-0.40	-0.41-i0.022

a) RT means the room temperature.

b) The units of d_{ij}, e_{ij}, s_{ij}^{E}, and c_{ij}^{E} are pC/N, C/m^2, pm^2/N, and ×10^9 N/m^2, respectively.

2.4 CONCLUSION

In summary, the fully ordered CTGS single crystals which were grown by the CZ pulling technique were investigated from the room temperature to 800°C. All the real and complex dielectric, piezoelectric, and elastic coefficients were completely determined. The determination of the real coefficients was based on the IEEE dynamic methods, and the related design and measurement information was summarized in Table 2-1. According to the methods of Du *et al*., and in combination with the structure characteristics of CTGS crystals, an effective program was designed to determine the complex coefficients and was summed up in Table 2-3. In addition, the results at three selected temperature points (21°C, 400°C, and 800°C) were shown in Table

2-4, and the comparisons with the previously reported results convincingly proved the accuracy of the methods employed in this paper. Our results show: 1) the dielectric permittivity and loss increase dramatically after 400°C, but the loss of CTGS is smaller than that of the PZT ceramic at the same temperature, 2) the piezoelectric coefficients stay relatively stable over the test temperature range with very slight increasing trends, 3) for the elastic constants, the absolute values of s_{ij}^{E} increase with the rise of temperature, while those of c_{ij}^{E} decrease, and among them, s_{11}, c_{11}, and c_{66} exhibit the best linearity with temperature. This work provides materials parameters for the further device design, fabrication, and applications of CTGS single crystals.

This chapter includes materials excerpted from the following publication of the author:

Zu, Hongfei, et al. "Characterization of the Dielectric, Piezoelectric, and Elastic Coefficients of Ca 3 TaGa 3 Si 2 O 14 Single Crystals up to 800° C." IEEE transactions on ultrasonics, ferroelectrics, and frequency control 63.5 (2016): 764-777.

3.0 FULL CHARACTERIZATION OF THE BASIC PROPERTIES OF $YCA_4O(BO_3)_3$ CRYSTALS UP TO 800ºC

As investigated in Chapter 1, similar to the ordered langasite family crystals, the rare-earth calcium oxyborate single crystals-ReCOB are another series of novel high-temperature materials, which will also not suffer from the severe obsession caused by phase change until the melting points (~1500°C) [110, 111, 117-120], and have been the focus of more and more consideration. In addition to the excellent high-temperature tolerance, ReCOB single crystals also exhibit remarkable piezoelectric properties: ultrahigh electric resistivity at elevated temperatures (10^6~10^8 Ω·cm at 1000°C), high coupling factors (~31.5%), quality factors (~10^4), and piezoelectric coefficients (~15.8 pC/N) [9, 111, 119, 196], which pave the path for them to become the encouraging alternatives to the traditional high-temperature piezoelectric materials. Furthermore, compared to CTGS, ReCOB crystals possess lower symmetry, indicating more opportunities to obtain low, even zero, temperature coefficients since the lower symmetry will provide a larger number of non-zero elastic constants to create greater possibilities to balance the temperature coefficients between a variety of crystal orientations [33, 197, 198].

Among the ReCOB crystals, the YCOB crystals were considered to be the preferred choice for high-temperature sensing from the perspective of performance, crystal stability and cost [9, 111, 117-120, 133, 196]. A lot of research on the basic properties and high-temperature applications of YCOB have been carried out recently. Shimizu and Takeda *et al.* [199, 200]

introduced the growth method, characterized the 27 independent material (dielectric, elastic and piezoelectric) constants, and investigated the surface acoustic wave (SAW) properties. But, their study lacks information about the effects of high-temperature on crystal performance. Yu, Zhang, and Kim *et al.* [34, 111, 201-204] studied the properties of YCOB in depth and detail over a wide temperature range, and developed the vibration sensors for ultra-high temperature (> 1000°C) use. However, the temperature dependence of the basic electromechanical properties has not been fully revealed. More significantly, the complex coefficients which are critical for describing the performance of both low-loss and lossy materials at elevated temperatures are poorly known.

Therefore, in this chapter, we will fully characterize the basic properties of YCOB crystals from the ambient temperature to 800°C as we did for CTGS in Chapter 2 to get a more comprehensive understanding of YCOB and lay a solid foundation for future applications.

3.1 EXPERIMETAL DETAILS

3.1.1 The synthesis of YCOB

The YCOB piezoelectric single crystals used in this work were grown in a conventional RF-heating Czochralski (CZ) furnace, and the high purity (99.99%) raw materials: $CaCO_3$, Y_2O_3, and H_3BO_3 were employed to synthesis the crystals. First, the powders of the raw materials were mixed in stoichiometric ratio and sintered at 1300°C for 20 h, and then, the sintered polycrystalline powders were introduced into an iridium crucible and melted at 1400°C. Subsequently, a YCOB single crystal with ⟨010⟩ direction was used as the seed to grow the

crystals by the CZ pulling technique. The crystals were grown at a rate of 0.5-1 mm/h with the rotation of 15-20 rpm under N_2 plus 1 vol% O_2 atmosphere. Finally, the as-grown crystals were cooled down to room temperature at the rate of 25 °C/h.

3.1.2 Experimental preparation

The experimental preparation for characterizing YCOB parameters, including the sample processing and system setup, is the same with that for CTGS described in Chapter 2. Please refer to the relevant section when necessary.

3.2 METHODS FOR THE DETERMINATION OF THE BASIC PROPERTIES OF YCOB CRYSTALS

3.2.1 The symmetry of YCOB

YCOB crystals belong to the monoclinic crystal system and the point group m. So the dielectric, piezoelectric, and elastic constants matrices are as follows:

$$\varepsilon_{ij} = \begin{bmatrix} \varepsilon_{11} & 0 & \varepsilon_{13} \\ 0 & \varepsilon_{22} & 0 \\ \varepsilon_{13} & 0 & \varepsilon_{33} \end{bmatrix} \quad \textbf{(3-1)}$$

$$d_{ij} = \begin{bmatrix} d_{11} & d_{12} & d_{13} & 0 & d_{15} & 0 \\ 0 & 0 & 0 & d_{24} & 0 & d_{26} \\ d_{31} & d_{32} & d_{33} & 0 & d_{35} & 0 \end{bmatrix} \quad \textbf{(3-2)}$$

$$s_{ij} = \begin{bmatrix} s_{11} & s_{12} & s_{13} & 0 & s_{15} & 0 \\ s_{12} & s_{22} & s_{23} & 0 & s_{25} & 0 \\ s_{13} & s_{23} & s_{33} & 0 & s_{35} & 0 \\ 0 & 0 & 0 & s_{44} & 0 & s_{46} \\ s_{15} & s_{25} & s_{35} & 0 & s_{55} & 0 \\ 0 & 0 & 0 & s_{46} & 0 & s_{66} \end{bmatrix} \quad \textbf{(3-3)}$$

For other types of these constants, such as β_{ij}, e_{ij}, and c_{ij}, they have the same forms with ε_{ij}, d_{ij}, and s_{ij}, respectively. It is obvious that the independent dielectric, piezoelectric, and elastic coefficients of YCOB single crystals are 4, 10, and 13, respectively, which are much more than the unknown constants of CTGS single crystals (2, 2, and 6, respectively). Therefore, to precisely determine all the properties of YCOB, a number of samples with different orientations for both longitudinal and shear vibrations are required, including some singly rotated, or even doubly rotated cuts. In the next section, the derivation process of the determination of all the coefficients based on the two methods (IEEE method and Du, Wang, and Uchino's method) will be discussed in detail, following the principles and procedures employed in Chapter 2.

3.2.2 IEEE dynamic method for the determination of the real constants

The basic principles and steps for the determination of the real constants of YCOB crystals according to the IEEE method are basically the same with those for CTGS, however, the characterization of YCOB is more complicated due to the low symmetry of the point group m. Many more differently oriented regular and rotated cuts are needed, and the solutions for the rotated cuts can be derived from the non-rotated ones by using a system of rotated axes (x_1', x_2', and x_3') which are rotated from the reference axes (x_1, x_2, and x_3) [28]. Accordingly, the

dielectric, piezoelectric, and elastic constants for any rotated cuts are given by the following general tensor formulas:

$$\varepsilon_{ij}^{'} = \frac{\partial x_i^{'}}{\partial x_k}\frac{\partial x_j^{'}}{\partial x_l}\varepsilon_{kl} \tag{3-4}$$

$$d_{ijk}^{'} = \frac{\partial x_i^{'}}{\partial x_l}\frac{\partial x_j^{'}}{\partial x_m}\frac{\partial x_k^{'}}{\partial x_n}d_{lmn} \tag{3-5}$$

$$s_{ijkl}^{'} = \frac{\partial x_i^{'}}{\partial x_m}\frac{\partial x_j^{'}}{\partial x_n}\frac{\partial x_k^{'}}{\partial x_o}\frac{\partial x_l^{'}}{\partial x_p}s_{mnop} \tag{3-6}$$

where the partial derivatives are the direction cosines defined as follows:

$$\frac{\partial x_i^{'}}{\partial x_m} = \begin{vmatrix} \frac{\partial x_1^{'}}{\partial x_1} & \frac{\partial x_1^{'}}{\partial x_2} & \frac{\partial x_1^{'}}{\partial x_3} \\ \frac{\partial x_2^{'}}{\partial x_1} & \frac{\partial x_2^{'}}{\partial x_2} & \frac{\partial x_2^{'}}{\partial x_3} \\ \frac{\partial x_3^{'}}{\partial x_1} & \frac{\partial x_3^{'}}{\partial x_2} & \frac{\partial x_3^{'}}{\partial x_3} \end{vmatrix} = \begin{vmatrix} l_1 & m_1 & n_1 \\ l_2 & m_2 & n_2 \\ l_3 & m_3 & n_3 \end{vmatrix} \tag{3-7}$$

3.2.2.1 Dielectric constants

The three dielectric constants on the diagonal (ε_{11}^T, ε_{22}^T, and ε_{33}^T) can be directly obtained from the measurement of capacitances of X-cut, Y-cut, and Z-cut square plate samples, respectively, through the following equations:

$$\varepsilon_{11,22,33}^T = \frac{C_{X,Y,Z}\cdot t}{A},\ \varepsilon_{r11,22,33}^T = \frac{\varepsilon_{11,22,33}^T}{\varepsilon_0}, \quad \text{and } \varepsilon_0 \approx 8.85\times10^{-12}\ F/m \tag{3-8}$$

where *C*, *t* and *A* are the low frequency capacitances (measured at 2 kHz), thicknesses, and effective areas of the plate samples, and ε_0 is the vacuum permittivity. Then, the ε_{13}^T can be determined by a singly rotated square plate sample (ZX*w*)45°, referring to Z-cut, through the following relationship which is derived from (3-4):

$$\varepsilon_{33}^{T}(\theta)=\varepsilon_{11}^{T}\sin^2\theta+2\varepsilon_{13}^{T}\cos\theta\sin\theta+\varepsilon_{33}^{T}\cos^2\theta \tag{3-9}$$

3.2.2.2 Elastic constants

As stated previously, the length-extensional modes of bar resonators possess the highest priority when considered for the determination of the elastic constants due to their high purity. The remaining constants which cannot be directly obtained from length-extensional modes can be measured through face/thickness shear mode vibrators. If we treat a rectangle bar sample whose length along the Y-axis as the reference sample, according to (3-6) and (3-7), the elastic constants of the rotated cuts can be generally denoted as：

$$\begin{aligned}s_{22}^{E}(\theta)=&\,s_{11}^{E}l_2^4+(2s_{12}^{E}+s_{66}^{E})l_2^2m_2^2+(2s_{13}^{E}+s_{55}^{E})l_2^2n_2^2\\&+2(s_{14}^{E}+s_{56}^{E})l_2^2m_2n_2+2s_{15}^{E}l_2^3n_2+2s_{16}^{E}l_2^3m_2+s_{22}^{E}m_2^4\\&+(2s_{23}^{E}+s_{44}^{E})m_2^2n_2^2+2s_{24}^{E}m_2^3n_2+2(s_{25}^{E}+s_{46}^{E})l_2m_2^2n_2\\&+2s_{26}^{E}l_2m_2^3+s_{33}^{E}n_2^4+2s_{34}^{E}m_2n_2^3+2s_{35}^{E}l_2n_2^3+2(s_{36}^{E}+s_{46}^{E})l_2m_2n_2^2\end{aligned} \tag{3-10}$$

Specific to YCOB crystals, we can get s_{22}^{E}, s_{33}^{E}, and $2s_{23}^{E}+s_{44}^{E}$ from (XY*t*)0°, 30°, and 60° cuts through

$$s_{22}^{E}(\theta)=s_{22}^{E}\cos^4\theta+(2s_{23}^{E}+s_{44}^{E})\sin^2\theta\cos^2\theta+s_{33}^{E}\sin^4\theta \tag{3-11}$$

and obtain s_{22}^{E}, s_{11}^{E}, and $2s_{12}^{E}+s_{66}^{E}$ from (ZY*t*)0°, -30°, and -60° cuts by

$$s_{22}^{E}(\theta)=s_{22}^{E}\cos^4\theta+(2s_{12}^{E}+s_{66}^{E})\sin^2\theta\cos^2\theta+s_{11}^{E}\sin^4\theta \tag{3-12}$$

Similarly, from (YZ*t*)0°, 30°, 45°, 60°, and 75° cuts, we can get s_{33}^{E}, s_{11}^{E}, s_{15}^{E}, s_{35}^{E}, and $2s_{13}^{E}+s_{55}^{E}$ by

$$\begin{aligned}s_{33}^{E}(\theta)=&\,s_{33}^{E}\cos^4\theta+2s_{35}^{E}\cos^3\theta\sin\theta+(2s_{13}^{E}+s_{55}^{E})\sin^2\theta\cos^2\theta\\&+2s_{15}^{E}\sin^3\theta\cos\theta+s_{11}^{E}\sin^4\theta\end{aligned} \tag{3-13}$$

In addition, (3-11)-(3-13) can mutually verify s_{11}^{E}, s_{22}^{E}, and s_{33}^{E}.

Then, the $2s_{25}^{E}+s_{46}^{E}$ can be acquired from (XZ*wt*)45°/45° cut by

$$s_{22}^{E'} = \frac{1}{16}(s_{11}^E + s_{55}^E + s_{33}^E) + \frac{1}{8}(s_{13}^E + s_{15}^E + s_{44}^E + s_{35}^E + s_{66}^E + s_{46}^E) + \frac{1}{4}(s_{12}^E + s_{22}^E + s_{23}^E + s_{25}^E) \quad \textbf{(3-14)}$$

Moreover, s_{44}^E, s_{55}^E, and s_{66}^E can be determined from the XY, YZ, and ZX face shear cuts, respectively, by

$$s^E(\theta) = \frac{1}{4\rho w^2 f_a^2 (1-k^2)} \quad \textbf{(3-15)}$$

$$k^2 = \frac{\pi}{2}\frac{f_r}{f_a}\cot\left(\frac{\pi}{2}\frac{f_r}{f_a}\right) \quad \textbf{(3-16)}$$

where ρ, w, f_r, f_a, and k are crystal density (3.28 g/cm^3), sample width, resonant frequency, anti-resonant frequency, and coupling factor, respectively. Furthermore, the s_{46}^E can be extracted from (ZXw)45° face shear sample through

$$s_{66}^E(\theta) = s_{66}^E \cos^2\theta - 2s_{46}^E \sin\theta\cos\theta + s_{44}^E \sin^2\theta \quad \textbf{(3-17)}$$

Finally, the s_{23}^E, s_{13}^E, s_{12}^E, and s_{25}^E, can be calculated through the relationships obtained from (3-11)-(3-14).

3.2.2.3 Piezoelectric constants

The characterization of the 10 piezoelectric constants can be accomplished through the dielectric, elastic, and coupling factor tensors:

$$d^2 = k^2 \varepsilon^T s^E \quad \textbf{(3-18)}$$

where the k can be got through (3-16) by measuring the f_r and f_a of certain pre-designed samples.

d_{11} and d_{33} can be directly obtained through (3-18) by the measurement of X-cut and Z-cut square plate samples. The determination of the remaining piezoelectric constants requires information of some combinations of reference and rotated samples. And the formulas for the rotated cuts can be derived from (3-5) and (3-7). Take (XYt)θ cuts for example,

$$\begin{aligned} d_{12}(\theta) = {} & d_{11}l_1l_2^2 + d_{12}l_1m_2^2 + d_{13}l_1n_2^2 + 2d_{15}l_1l_2n_2 \\ & + 2d_{24}m_1m_2n_2 + 2d_{26}m_1l_2m_2 \\ & + d_{31}n_1l_2^2 + d_{32}n_1m_2^2 + d_{33}n_1n_2^2 + 2d_{35}n_1l_2n_2 \end{aligned} \quad \textbf{(3-19)}$$

Applying (3-19) to YCOB crystals, we can get d_{12} and d_{13} from (XY*t*)0° and 60° cuts through

$$d_{12}(\theta) = d_{12}\cos^2\theta + d_{13}\sin^2\theta \quad \textbf{(3-20)}$$

Similarly, we can obtain:

d_{31} and d_{32} from (ZY*t*)0° and -60° cuts through

$$d_{32}(\theta) = d_{32}\cos^2\theta + d_{31}\sin^2\theta \quad \textbf{(3-21)}$$

d_{32} and d_{33}-$2d_{24}$ from (ZY*w*)0° and 45° cuts through

$$d_{32}(\theta) = d_{32}\cos^3\theta + (d_{33} - 2d_{24})\sin^2\theta\cos\theta \quad \textbf{(3-22)}$$

d_{12} and d_{11}-$2d_{26}$ from (XY*w*)0° and 45° cuts through

$$d_{12}(\theta) = d_{12}\cos^3\theta + (d_{11} - 2d_{26})\sin^2\theta\cos\theta \quad \textbf{(3-23)}$$

d_{13}, d_{11}-$2d_{35}$, d_{31}, and $2d_{15}$-d_{33} from (XZ*w*)0°, 30°, 45°, and 60° cuts through

$$\begin{aligned} d_{13}(\theta) = {} & d_{13}\cos^3\theta + (d_{11} - 2d_{35})\sin^2\theta\cos\theta \\ & - d_{31}\sin^3\theta + (2d_{15} - d_{33})\sin\theta\cos^2\theta \end{aligned} \quad \textbf{(3-24)}$$

Additionally, in this procedure, (3-20)-(3-24) can mutually verify d_{12}, d_{13}, d_{31}, and d_{32}.

3.2.3 Du, Wang, and Uchino's method for the determination of the complex constants

In Du's papers [49, 50, 190] and Chapter 2 in this work, the method for determining the complex constants has been meticulously deduced and successfully applied on PZT ceramics, $LiNbO_3$ and CTGS single crystals. Herein, we will take advantage of this mature approach to characterize the complex constants of YCOB crystals.

3.2.3.1 Dielectric constants

The three complex dielectric constants on the diagonal can be got from X-cut, Y-cut, and Z-cut square plate samples through

$$\varepsilon_r = \varepsilon_r^{'} - i\varepsilon_r^{''}, \qquad \varepsilon_r^{''} = \varepsilon_r^{'} \cdot D \tag{3-25}$$

And then, by measuring the capacitance and dissipation of (ZX*w*)45° square plate sample, the ε_{r13} can be determined through (3-9). If C_p and D were measured at a low frequency (2 kHz), the ε_r^T will be got; if they were measured at a high frequency (20 MHz), the ε_r^S will be obtained.

3.2.3.2 Elastic and piezoelectric constants

X-cut square plate sample with n//l=[1 0 0]^t

The matrices **A** and **B** are as follows:

$$\mathrm{A} = \begin{bmatrix} c_{11}^E + \dfrac{e_{11}^2}{\varepsilon_{11}^S} & 0 & c_{15}^E + \dfrac{e_{11}e_{15}}{\varepsilon_{11}^S} \\ 0 & c_{66}^E & 0 \\ c_{15}^E + \dfrac{e_{11}e_{15}}{\varepsilon_{11}^S} & 0 & c_{55}^E + \dfrac{e_{15}^2}{\varepsilon_{11}^S} \end{bmatrix} = \begin{bmatrix} c_{11}^D & 0 & c_{15}^D \\ 0 & c_{66}^E & 0 \\ c_{15}^D & 0 & c_{55}^D \end{bmatrix}, \quad \mathrm{B} = \begin{bmatrix} e_{11} \\ 0 \\ e_{15} \end{bmatrix} \tag{3-26}$$

where **A** indicates there are two mixed extensional shear modes (c_{11} and c_{15}; c_{15} and c_{55}), and one pure shear mode (c_{66}), while **B** illustrates that the electric field in X-direction only can stimulate the two mixed extensional shear modes. Therefore, by identifying the three corresponding resonant frequencies, the c_{11}^D, c_{15}^D, c_{55}^D, e_{11}, and e_{15} can be directly determined by

$$\Lambda = \sqrt{\rho / c^D}, \quad k^2 = \frac{e^2}{\varepsilon^S \cdot c^D}, \quad \eta = k^2 / C, \quad A = \frac{\eta}{\omega \Lambda a} \tag{3-27}$$

Afterwards, c_{11}^E, c_{15}^E, and c_{55}^E can be obtained straightforwardly through (3-26).

Y-cut square plate sample with n//l=[0 1 0]^t

Similarly, the **A** and **B** matrices of Y-cut plate are

$$\mathrm{A}=\begin{bmatrix} c_{66}^{E}+\dfrac{e_{26}^{2}}{\varepsilon_{22}^{S}} & 0 & c_{46}^{E}+\dfrac{e_{24}e_{26}}{\varepsilon_{22}^{S}} \\ 0 & c_{22}^{E} & 0 \\ c_{46}^{E}+\dfrac{e_{24}e_{26}}{\varepsilon_{22}^{S}} & 0 & c_{44}^{E}+\dfrac{e_{24}^{2}}{\varepsilon_{22}^{S}} \end{bmatrix}=\begin{bmatrix} c_{66}^{D} & 0 & c_{46}^{D} \\ 0 & c_{22}^{E} & 0 \\ c_{46}^{D} & 0 & c_{44}^{D} \end{bmatrix},\quad \mathrm{B}=\begin{bmatrix} e_{26} \\ 0 \\ e_{24} \end{bmatrix} \tag{3-28}$$

Accordingly, two coupled shear modes (c_{66} and c_{46}; c_{46} and c_{44}) and one pure extensional mode (c_{22}) exist in Y-cut plate resonator, and the electric field in Y-direction can excite the two coupled shear modes. Thus, in this case, c_{66}^{D}, c_{46}^{D}, c_{44}^{D}, e_{24}, e_{26}, c_{66}^{E}, c_{46}^{E}, and c_{44}^{E} can be got.

Z-cut square plate sample with n//l=[0 0 1]^t

$$\mathrm{A}=\begin{bmatrix} c_{55}^{E}+\dfrac{e_{35}^{2}}{\varepsilon_{33}^{S}} & 0 & c_{35}^{E}+\dfrac{e_{33}e_{35}}{\varepsilon_{33}^{S}} \\ 0 & c_{44}^{E} & 0 \\ c_{35}^{E}+\dfrac{e_{33}e_{35}}{\varepsilon_{33}^{S}} & 0 & c_{33}^{E}+\dfrac{e_{33}^{2}}{\varepsilon_{33}^{S}} \end{bmatrix}=\begin{bmatrix} c_{55}^{D} & 0 & c_{35}^{D} \\ 0 & c_{44}^{E} & 0 \\ c_{35}^{D} & 0 & c_{33}^{D} \end{bmatrix},\quad \mathrm{B}=\begin{bmatrix} e_{35} \\ 0 \\ e_{33} \end{bmatrix} \tag{3-29}$$

As one can see, there are two mixed extensional shear modes (c_{55} and c_{35}; c_{35} and c_{33}), and one pure shear mode (c_{44}), and the two mixed extensional shear modes can be inspired by the Z-direction electric field. Consequently, c_{55}^{D}, c_{35}^{D}, c_{33}^{D}, e_{35}, e_{33}, c_{55}^{E}, c_{35}^{E}, and c_{33}^{E} can be obtained.

XY-cut rectangular bar sample with n⊥l, n=[1 0 0]^t, and l=[0 1 0]^t

$$\mathrm{A}\begin{bmatrix} s_{66}^{E} & 0 & s_{46}^{E} \\ 0 & s_{22}^{E} & 0 \\ s_{46}^{E} & 0 & s_{44}^{E} \end{bmatrix},\quad \mathrm{B}=\begin{bmatrix} 0 \\ d_{12} \\ 0 \end{bmatrix} \tag{3-30}$$

Obviously, in XY-cut rectangular bar sample, there are two coupled shear modes (s_{66} and s_{46}; s_{46} and s_{44}) and one pure extensional mode (s_{22}), and the pure extensional mode can be excited

by the electric field in X-direction. Therefore, under this condition, s_{22}^E and d_{12} can be determined through

$$\Lambda = \sqrt{\rho \cdot s^E}, \quad k^2 = \frac{d^2}{\varepsilon^T \cdot s^E}, \quad \eta = C \cdot k^2, \quad A = \frac{\eta}{\omega \Lambda a} \tag{3-31}$$

ZY-cut rectangular bar sample with n⊥l, n=[0 0 1]^t, and l=[0 1 0]^t

$$\mathrm{A} = \begin{bmatrix} s_{66}^E & 0 & s_{46}^E \\ 0 & s_{22}^E & 0 \\ s_{46}^E & 0 & s_{44}^E \end{bmatrix}, \quad \mathrm{B} = \begin{bmatrix} 0 \\ d_{32} \\ 0 \end{bmatrix} \tag{3-32}$$

Extremely similar to the above case (*XY*-cut bar), s_{22}^E and d_{32} can be obtained in this case.

ZX-cut rectangular bar sample with n⊥l, n=[0 0 1]^t, and l=[1 0 0]^t

$$\mathrm{A} = \begin{bmatrix} s_{11}^E & 0 & s_{15}^E \\ 0 & s_{66}^E & 0 \\ s_{15}^E & 0 & s_{55}^E \end{bmatrix}, \quad \mathrm{B} = \begin{bmatrix} d_{31} \\ 0 \\ d_{35} \end{bmatrix} \tag{3-33}$$

From **A** and **B**, it can be known that the two mixed extensional shear modes (s_{11} and s_{15}; s_{15} and s_{55}) can be stimulated to measure s_{11}^E, s_{15}^E, s_{55}^E, d_{31}, and d_{35}.

XZ-cut rectangular bar sample with n⊥l, n=[1 0 0]^t, and l=[0 0 1]^t

$$\mathrm{A} = \begin{bmatrix} s_{55}^E & 0 & s_{35}^E \\ 0 & s_{44}^E & 0 \\ s_{35}^E & 0 & s_{33}^E \end{bmatrix}, \quad \mathrm{B} = \begin{bmatrix} d_{15} \\ 0 \\ d_{13} \end{bmatrix} \tag{3-34}$$

Very similar to *ZX*-cut bar sample, the *XZ*-cut can be used to solve s_{55}^E, s_{35}^E, s_{33}^E, d_{15}, and d_{13}.

So far, eight elastic stiffness constants (c_{11}^E, c_{15}^E, c_{55}^E, c_{66}^E, c_{46}^E, c_{44}^E, c_{35}^E, and c_{33}^E) and six elastic compliance constants (s_{22}^E, s_{11}^E, s_{15}^E, s_{55}^E, s_{35}^E, and s_{33}^E) have been obtained, which are enough to determine the remaining s_{ij}^E and c_{ij}^E according to:

$$c_{ij}^E = (s_{ij}^E)^{-1} \tag{3-35}$$

Subsequently, all d_{ij} and e_{ij} can be determined from the known parameters: e_{11}, e_{15}, e_{24}, e_{26}, e_{33}, e_{35}, d_{12}, d_{32}, d_{31}, d_{35}, d_{13}, and d_{15} through

$$e_{nj} = d_{ni} c_{ij}^{E} \tag{3-36}$$

One may have found that the number of the sample cuts used to determine the complex constants is much less than that used for the real constants, however, it does not mean the characterization of the real constants must require more cuts than the complex ones. Actually, if the orientation, dimension, and electric direction of one sample are the same, the vibration modes and the information they carry will be the same. The reason why we employed more samples to solve the real constants is that the calculation of the IEEE method is relatively simple, so we tried to use the purest vibration mode to extract each coefficient, regardless of the calculation process; however, the calculation of the Du, Wang, and Uchino's method is much more complex, especially for the rotated cuts, the **M**, **L**, **A**, and **B** matrices of which are very cumbersome, so we tried to use non-rotated samples, as few as possible, to accomplish the characterization of the complex constants.

Figure 3-1 graphically shows the sample orientations used in this work, among which the X, Y, and Z -cuts are square plates with the dimension of 12×12×2 mm^3, and all others are rectangular bars with the dimension of 18×5×1 mm^3. Here, the sample cuts which were rotated in the same way, but in different angles are usually represented by one small graphic. For example, the one marked as (7) in Figure 3-1.(a) stands for (YZ*t*)30°, 45°, 60°, and 75° cuts. The notations of the cuts follow IEEE standard [6].

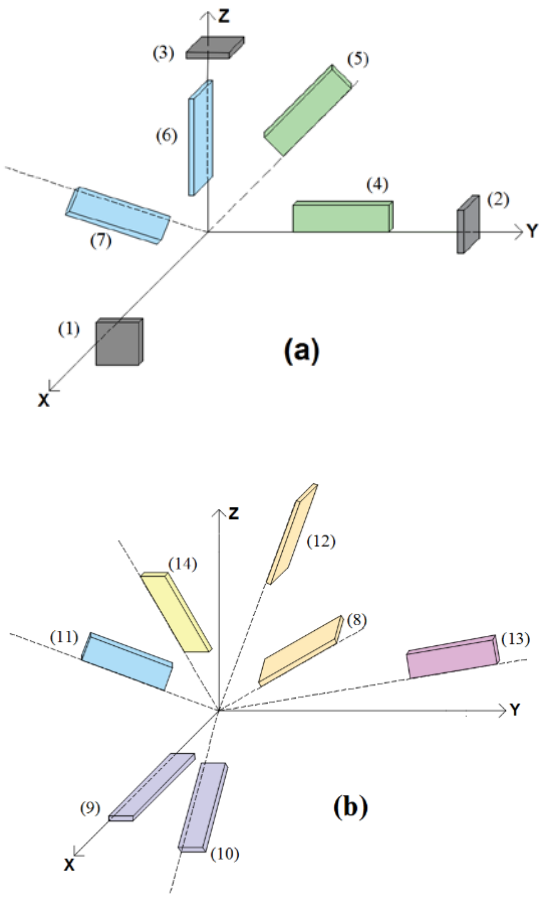

Figure 3-1. The sample orientations used for the determination of properties of YCOB: **(a)**: (1) X-cut, (2) Y-cut, (3) Z-cut, (4) XY-cut, (5) (XY*t*)30°, and 60°, (6) YZ-cut, (7) (YZ*t*)30°, 45°, 60°, and 75°; **(b)**: (8) (ZY*t*)0°, -30°, and -60°, (9) ZX-cut, (10) (ZX*w*)45°, (11) (XZ*wt*)45°/45°, (12) (ZY*w*)0°, and 45°, (13) (XY*w*)0°, and 45°, (14) (XZ*w*)0°, 30°, 45°, and 60°.

Table 3-1 summarizes the sample cuts employed for determining each dielectric, elastic, and piezoelectric constant using the aforementioned two methods.

Table 3-1. Sample cuts used for determining each parameter of YCOB crystal.

IEEE method		Du, Wang, and Uchino's method	
Parameters	Sample cuts	Parameters	Sample cuts
ε_{11} ε_{22} ε_{33}	X-cut Y-cut Z-cut	ε_{11} ε_{22} ε_{33}	X-cut Y-cut Z-cut
ε_{13}	(ZX*w*)45°	ε_{13}	(ZXw)45°
s_{22}, s_{33}, $2s_{23}+s_{44}$	(XY*t*)0°, 30°, 60°	c_{11}, c_{15}, c_{55}, e_{11}, e_{15}	X-cut
s_{22}, s_{11}, $2s_{12}+s_{66}$	(ZY*t*)0°, -30°, -60°		
s_{33},s_{11},s_{15},s_{35} $2s_{13}+s_{55}$	(YZ*t*)0°, 30°, 45°, 60°, 75°	c_{66}, c_{44}, c_{46}, e_{24}, e_{26}	Y-cut
$2s_{25}+s_{46}$	(XZ*wt*)45°/45°		
c_{66}, s_{66}, s_{12}	ZX-cut	c_{33}, c_{35}, c_{55}, e_{33}, e_{35}	Z-cut
c_{44}, s_{44}, s_{23}	XY-cut		
s_{55}, s_{13}	YZ-cut	s_{22}, d_{12}	XY-cut
s_{46}, s_{25}	(ZX*w*)45°		
d_{12}, d_{13} d_{31}, d_{32} d_{32}, d_{33}- $2d_{24}$ d_{12}, d_{11}- $2d_{26}$	(XY*t*)0°, 60° (ZY*t*)0°, -60° (ZY*w*)0°, 45° (XY*w*)0°, 45°	s_{22}, d_{32}	ZY-cut
		s_{11}, s_{15}, s_{55}, d_{31}, d_{35}	ZX-cut
d_{11} d_{33}	X-cut Z-cut	s_{33}, s_{35}, s_{55}, d_{13}, d_{15}	XZ-cut
d_{13}, d_{11}- $2d_{35}$, d_{31}, $2d_{15}$- d_{33}	(XZ*w*)0°,30°,45,60°		

3.3 RESULTS AND DISCUSSION

According to the previously mentioned methods and procedures, all the real and complex dielectric, elastic and piezoelectric coefficients of YCOB crystals were determined in the temperature range of 21 to 800°C. Since YCOB crystals possess many independent nonzero coefficients, the results will be shown as concisely as possible but informatively enough to facilitate information retrieval. Thus, in this chapter, we will only graphically show the coefficients which were directly obtained, not including those calculated through (3-35) and (3-36). In addition, most of the real and imaginary parts of complex coefficients will not be shown in the same figure. So, "(i)" or "(-i)" will not be used to represent whether the signs of

real and imaginary parts are consistent any more. Instead, the sign of each parameter will be clearly marked out in the figures.

3.3.1 Dielectric constants

Figure 3-2 shows the temperature dependence of both the real and complex dielectric constants in the range of 21 to 800°C. Obviously, they all possess the tendency to increase with the elevated temperature. Especially the imaginary parts of the complex coefficients, they increase dramatically after 400°C, indicating that the electrical loss turns larger abruptly above 400°C, and further illustrating that the free charge in YCOB crystals accumulates rapidly after 400°C. All of the dielectric components of the main diagonal are positive (ε_{r11}^{T}: 8.18~36.34, ε_{r22}^{T}: 11.34~45.97, and ε_{r33}^{T}: 9.86~38.26), while the remaining element of the secondary diagonal is negative and much smaller (ε_{r13}^{T}: -0.88~-15.92), which implies that if the electric field is applied along the +X direction, the positive charge of dielectric polarization will appear in the -Z face. In addition, the ε_{r22}^{T} is slightly larger than ε_{r11}^{T} and ε_{r33}^{T}, which has been demonstrated to be partially attributed to the longer average bond length along *b* axis than *a* and *c* axes in the rare earth oxygen octahedron [111, 120]. Furthermore, the dielectric losses $tan\delta=(\varepsilon_{r}^{T})''/(\varepsilon_{r}^{T})'$ from room temperature to 800°C are presented in Figure 3-3. As can be seen, the electrical losses of YCOB under high temperatures are lower than CTGS, indicating why YCOB possesses higher resistivity. In addition, the loss in Y direction (about 1.7 at 800°C) is the smallest.

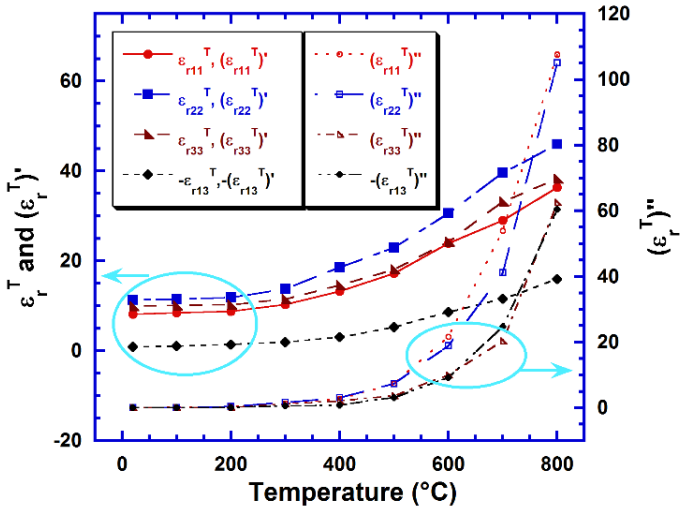

Figure 3-2. The real and complex dielectric coefficients of YCOB versus temperature.

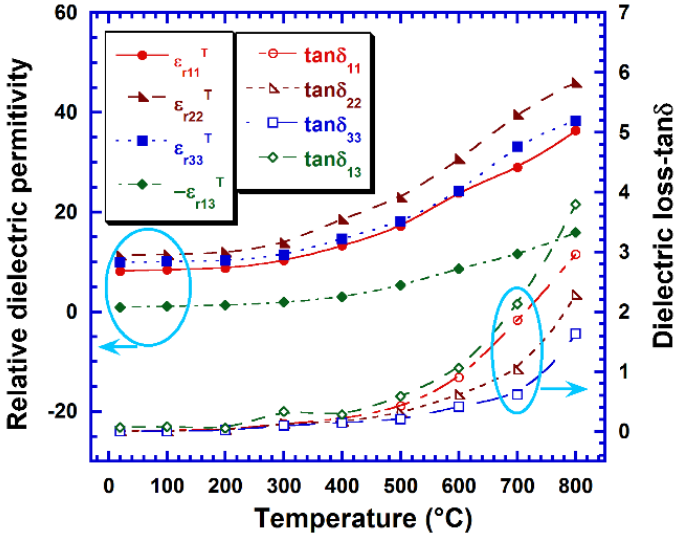

Figure 3-3. Relative permittivity and dielectric loss of YCOB versus temperature.

3.3.2 Elastic constants

3.3.2.1 Real elastic constants

Figure 3-4 displays the 6 real elastic compliance constants on the main diagonal s_{ii}^E (i=1~6) of YCOB crystal, while Figure 3-5 shows the other 7 off the main diagonal. As can be seen from Figure 3-4, all the main diagonal elements increase with the elevated temperature and exhibit excellent linearity, demonstrated by the extremely high regression coefficients R^2 (basically >0.99). Among the 6 components, s_{44}^E is the largest in value (32.77 to 36.59 pm^2/N) and s_{33}^E possesses the best linearity (R^2=0.99785). By contrast, s_{22}^E is minimal (6.81 to 7.70 pm^2/N) and the linearity is relatively low (R^2=0.98964). It is worth noting that the pure shear factors (s_{44}^E, s_{55}^E, and s_{66}^E) are much larger than the pure extensional ones (s_{11}^E, s_{22}^E, and s_{33}^E), indicating YCOB crystals will behave softer in pure shear vibrations. In addition, as shown in Figure 3-5, the constants off the main diagonal also rise as the temperature increases. However, they are much smaller in values (generally <4 pm^2/N) and lower in linearity (R^2<0.98).

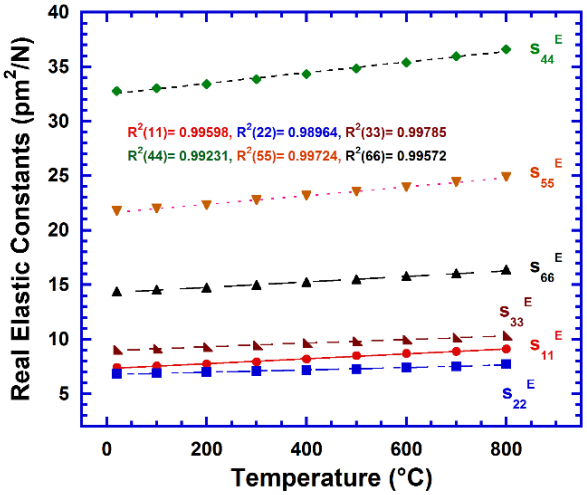

Figure 3-4. Real elastic compliance constants on the main diagonal of YCOB crystal versus temperature.

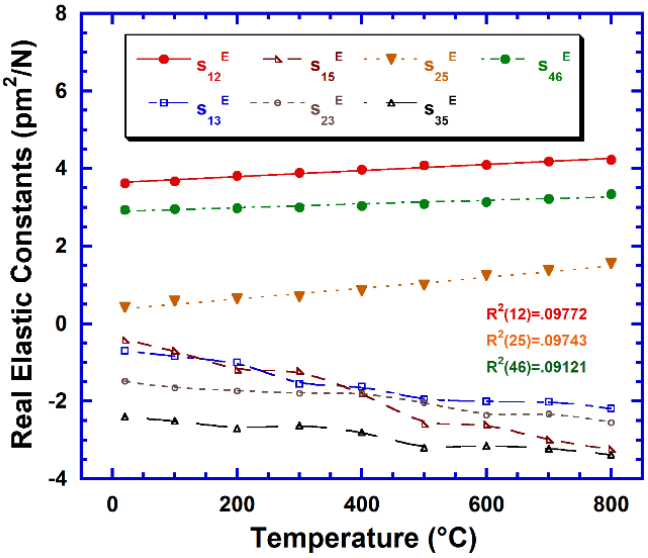

Figure 3-5. Real elastic compliance constants off the main diagonal of YCOB crystal versus temperature.

3.3.2.2 Complex elastic constants

The directly obtained complex elastic constants through the methods derived in section 3.2.3.2 are as follows: c_{11}^D, c_{15}^D, c_{55}^D, c_{66}^D, c_{46}^D, c_{44}^D, c_{35}^D, c_{33}^D, s_{22}^E, s_{11}^E, s_{15}^E, s_{55}^E, and s_{33}^E. Figure 3-6 shows the real parts of the 5 elastic stiffness constants on the main diagonal, while Figure 3-7 exhibits the corresponding imaginary parts. Contrary to the s_{ii}^E shown in Figure 3-4, c_{ii}^D decrease linearly (R^2>0.99 basically) with the temperature increases. c_{66}^D possesses the best linearity (R^2=0.99941), while c_{55}^D the lowest (R^2=0.94569). And the smaller the s_{ii}^E, the larger the c_{ii}^D, among which the smallest is c_{44}^D (31.04 to 27.54 ×10^9 N/m^2), and the largest is c_{11}^D (173.62 to 153.94 ×10^9 N/m^2, c_{22}^D is even higher). Moreover, the larger pure elements illustrate YCOB crystals will behave harder in pure extensional vibrations, which is consistent with the previous conclusion.

The imaginary parts shown in Figure 3-7 are very small when the temperature is lower than 600°C, and increase dramatically after that. However, compared with their real parts, they

are about 4 to 5 orders of magnitude lower before 600°C, and about 3 to 4 orders lower at 800°C, demonstrating the elastic loss of YCOB is quite low even under ultra-high temperature. In addition, the large real part is usually accompanied by a large imaginary part.

Figure 3-8 shows c_{15}^{D}, c_{46}^{D}, and c_{35}^{D}, which are much smaller than the main diagonal components in value, but have the same trend with temperature. Among them, (c_{46}^{D})' is negative. The negative elastic constants are considered likely to affect the stability of the crystal lattices. But according to the "Born stability criteria" [205, 206] and some follow-up scholars' derivation [207, 208], the necessary and sufficient stability conditions for crystal lattices are: 1) the matrix **C** is definite positive, 2) all eigenvalues of **C** are positive, 3) all the leading principal minors of **C** are positive, and 4) an arbitrary set of minors of **C** are all positive. This requires all main diagonal elements of **C** (c_{ii}) should be positive, but it's not necessary for non-main diagonal elements. Another noteworthy point is that all the complex elastic constants mentioned in this part are with the form c_{ij}^{D}=(c_{ij}^{D})'-(c_{ij}^{D})".

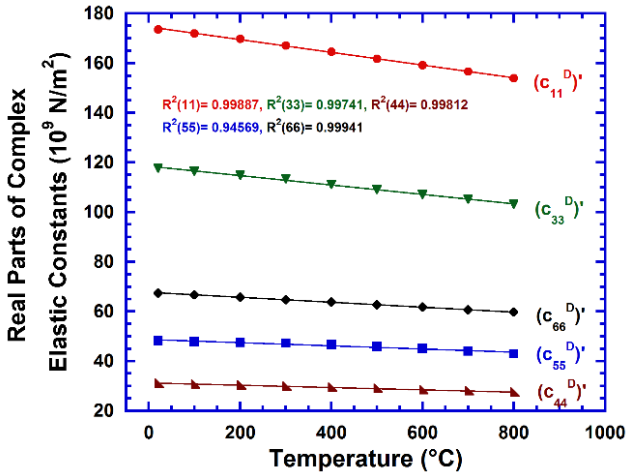

Figure 3-6. Real parts of complex elastic stiffness constants on the main diagonal of YCOB crystal versus temperature.

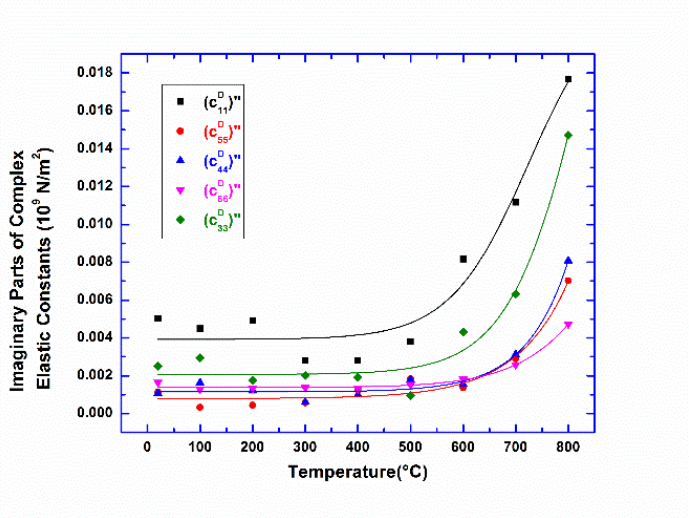

Figure 3-7. Imaginary parts of complex elastic stiffness constants on the main diagonal of YCOB crystal versus temperature.

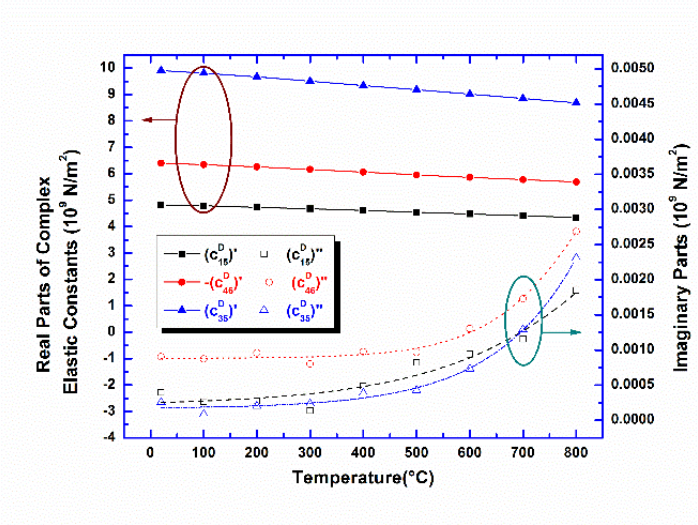

Figure 3-8. Some other complex elastic stiffness constants off the main diagonal of YCOB crystal versus temperature.

Figure 3-9 exhibits the real parts of the 5 complex elastic compliance constants (s_{22}^E, s_{11}^E, s_{15}^E, s_{55}^E, and s_{33}^E), and their values, even the regression coefficients R^2, are very close to the

corresponding real constants shown in Figure 3-4 and Figure 3-5, which is a strong proof of the high consistency of the two employed methods. The imaginary parts are shown in Figure 3-10, and their small values once again prove that the elastic loss of YCOB is very low. In addition, all the complex compliance constants discussed in this part are with the form s_{ij}^{E}=(s_{ij}^{E})'+(s_{ij}^{E})".

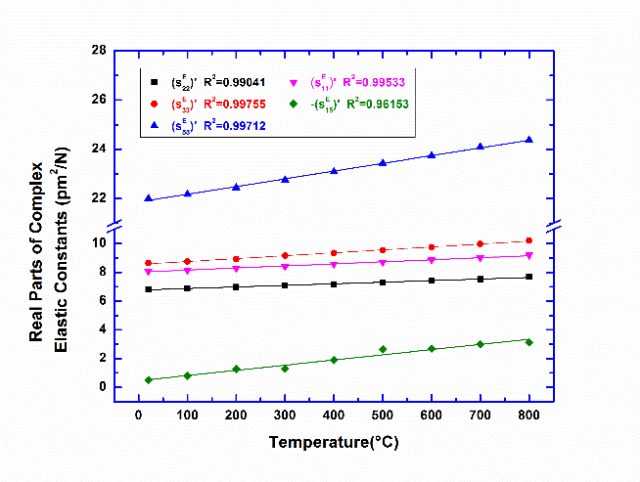

Figure 3-9. Real parts of some complex elastic compliance constants of YCOB crystal versus temperature.

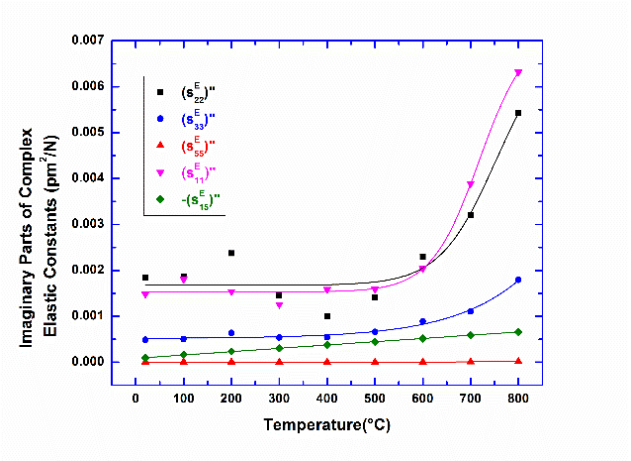

Figure 3-10. Imaginary parts of some complex elastic compliance constants of YCOB crystal versus temperature.

3.3.3 Piezoelectric constants

3.3.3.1 Real piezoelectric constants

Figure 3-11 shows the 10 real piezoelectric constants-d_{ij}, all of which slightly increase with the rise of temperature. Among them, d_{11}, d_{12}, d_{26}, d_{33}, and d_{35} are positive, while d_{13}, d_{15}, d_{24}, d_{31}, and d_{32} are negative. The positive/negative sign only reflects the direction, not representing the size of the constants, e.g., d_{13} is negative means that if the normal strain/stress is applied in the +Z direction, the induced polarization will be along -X direction. In another word, the induced positive charge will accumulate in the -X face. As one can see, d_{26}, d_{24}, d_{15}, and d_{32} are relatively large in value (3.7~8.2, -3.1~-8.5, -2.3~-6.1, and -3.4~-5.6 pC/N, respectively). By contrast, d_{11} (0.57~0.85 pC/N) and d_{33} (0.68~1.3 pC/N) are the smallest.

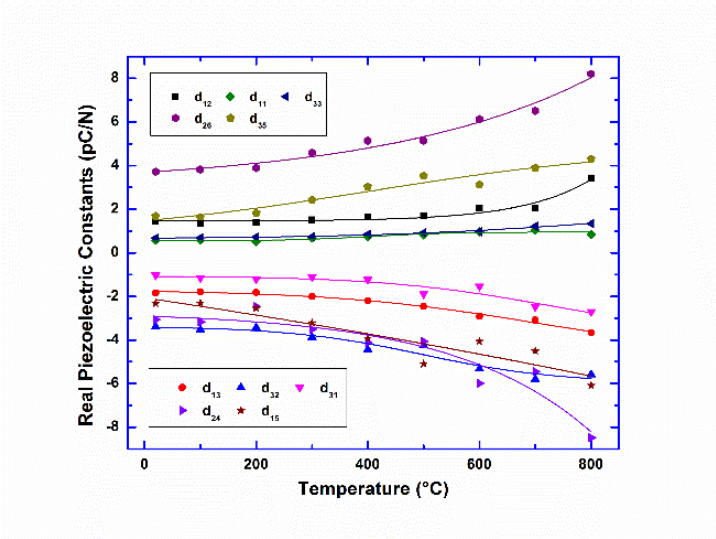

Figure 3-11. Real piezoelectric constants (d_{ij}) of YCOB crystal versus temperature.

3.3.3.2 Complex piezoelectric constants

The complex piezoelectric constants directly obtained through Du, Wang, and Uchino's method in this work are d_{12}, d_{32}, d_{31}, d_{35}, d_{13}, d_{15}, e_{11}, e_{15}, e_{24}, e_{26}, e_{33}, and e_{35}. Figure 3-12 presents both the real parts and imaginary parts of the two positive piezoelectric charge constants d_{12} and d_{35}, and the four negative ones d_{32}, d_{31}, d_{35}, and d_{13} are shown in Figure 3-13. As can be seen, both the real parts and imaginary parts increase slightly with the elevated temperature, which is very consistent with the behavior of real constants. Moreover, the imaginary parts synchronize with the real parts, but are about one order of magnitude lower in value.

Figure 3-14 exhibits the temperature dependence of e_{11}, e_{26}, and e_{33}, and Figure 3-15 displays the results of e_{15}, e_{24}, and e_{35}. All the real parts decrease slightly as the temperature rises, except for (e_{11})', while all the imaginary parts increase. Similar to the charge constants d_{ij}, the imaginary parts of e_{ij} are about one order of magnitude lower than the corresponding real parts. (e_{11})', (e_{15})', (e_{24})', (e_{26})', (e_{33})', and (e_{35})' vary in the following range as the temperature increases from the room temperature to 800°C: 0.039~0.14, 0.14~0.04, 0.053~0.029, 0.07~0.073, 0.034~0.031, and 0.060~0.007 C/m^2, respectively.

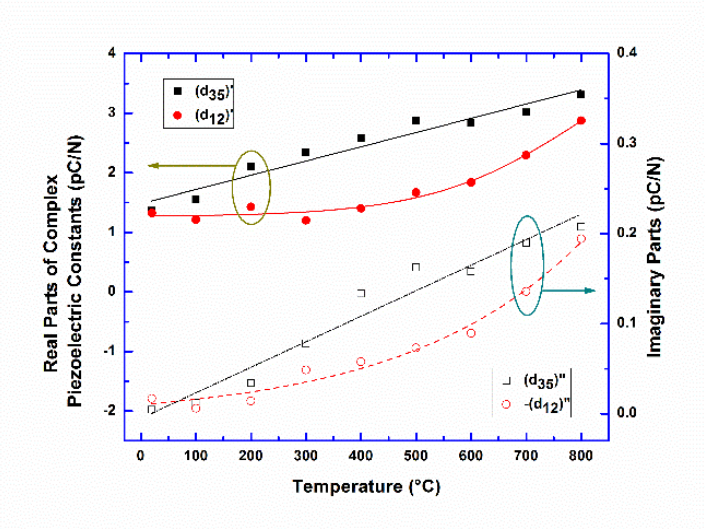

Figure 3-12. Complex piezoelectric constants ($\boldsymbol{d_{12}}$ and $\boldsymbol{d_{35}}$) of YCOB crystal versus temperature.

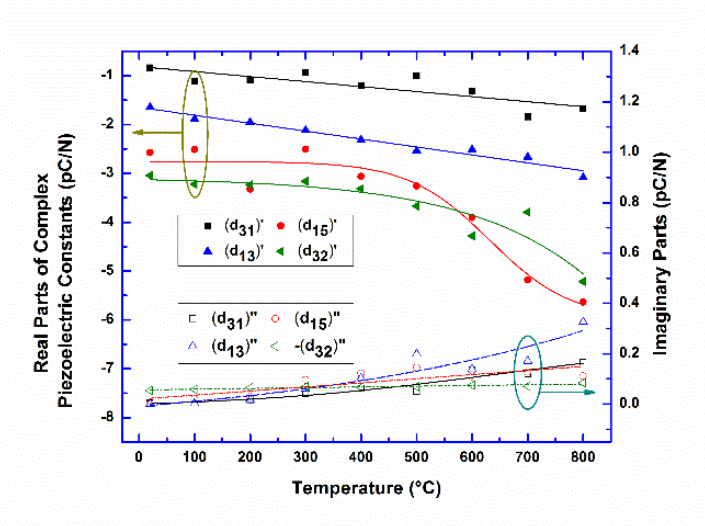

Figure 3-13. Complex piezoelectric constants ($\boldsymbol{d_{13}}$, $\boldsymbol{d_{15}}$, $\boldsymbol{d_{31}}$, and $\boldsymbol{d_{32}}$) of YCOB crystal versus temperature.

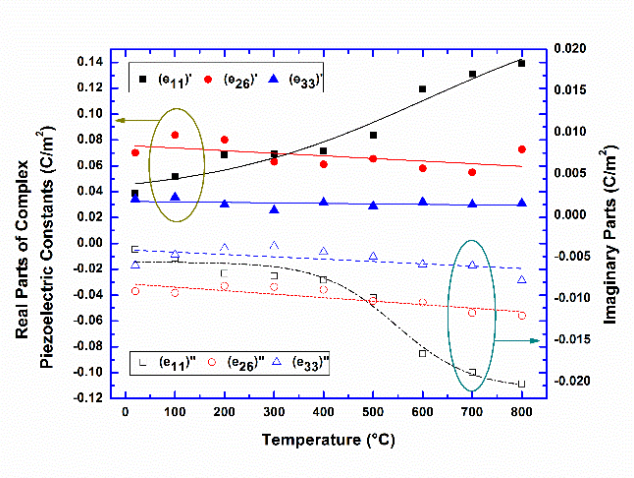

Figure 3-14. Complex piezoelectric constants (e_{11}, e_{26}, and e_{33}) of YCOB crystal versus temperature.

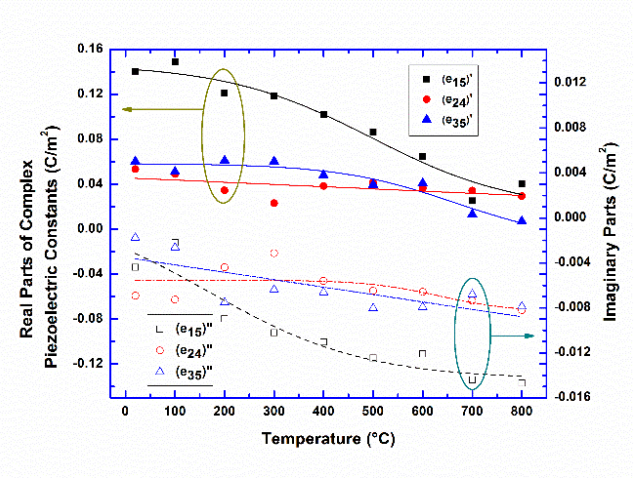

Figure 3-15. Complex piezoelectric constants (e_{15}, e_{24}, and e_{35}) of YCOB crystal versus temperature.

3.4 CONCLUSION

To sum up, in this Chapter, the basic properties of YCOB single crystals were fully characterized in a wide temperature range from ambient temperature to 800°C, including all the real and complex dielectric, piezoelectric, and elastic constants. Similar to the characterization of CTGS, the real constants of YCOB were obtained by the IEEE dynamic method, and the complex ones were determined according to the approach developed by Du, Wang, and Uchino. Owing to the low symmetry of YCOB, the independent dielectric, piezoelectric, and elastic coefficients are 4, 10, and 13, respectively. The method of determining each parameter was deduced in detail, and 23 kinds of cut samples were needed accordingly, which were shown in Figure 3-1. And Table 3-1 lists the cut orientation of crystal used to determine each parameter.

According to our measurement and calculation, we can get the following conclusions:

1) The dielectric permittivity and loss increase dramatically after 400°C, and the loss of YCOB is a little smaller than CTGS. And among the relative permittivity, ε_{r22}^{T} possesses the largest value, while ε_{r13}^{T} is the smallest and negative;

2) The elastic compliance constants basically increase linearly with the temperature rises, while the stiffness constants decrease linearly. The components on the main diagonal (s_{ii}^{E} and c_{ii}^{D} (i=1~6)) possess better linearity and larger values than the non-main diagonal elements. Most of the imaginary parts of the complex constants increase dramatically after 600°C, but they are about 3 to 5 orders of magnitude lower than the real parts;

3) The real piezoelectric charge constants d_{ij} (or real parts of complex constants (d_{ij})') increase slightly with the elevated temperature, while the (e_{ij})' basically decrease with the increase of the

temperature. And the imaginary parts are about one tenth of the corresponding real parts in value. In addition, d_{26}, d_{24}, d_{15}, and d_{32} are relatively large in value.

4.0 ROBUST BAW TEMPERATURE SENSOR

In Chapter 2 and 3, we fully characterized the basic dielectric, elastic and piezoelectric constants of the two very promising high temperature sensing crystals-CTGS and YCOB, respectively, and determined their temperature-dependent behavior over the temperature range of 21 to 800°C. From this Chapter, we will implement research on reliable and robust sensor devices, which are with a variety of different applications under high temperature, on the basis of the previous work. Obviously, the study on YCOB sensors will encounter a higher complexity than CTGS ones due to the coupling among different vibration modes caused by the low symmetry of monoclinic crystal. In this work, we will mainly study the high-temperature sensor applications based on CTGS crystals. But, the basic principles and derived models of CTGS sensors can be used for similar YCOB sensors by taking into account the low symmetry.

When selecting a sensor, there are many key items to consider:

- Sensitivity - This is usually the most representative factor for sensors. Because it directly displays the relationship between the directly measured parameters and the indirectly desired ones, and it also reflects how “sensitive” is the former to the latter;
- Accuracy & Precision - Accuracy has to do with how close the sensor reading is to the actual value, while Precision refers to the ability of the sensor to detect small changes;
- Long-term Stability - Any material or device suffers more or less from aging, which will result in drift of the characteristic parameters, inaccurate outputs, or even failure of the entire

system. The long-term stability is pursued by every sensing device, especially for the ones used in harsh environment, where it is time-consuming and costly to get the access to change the sensors inside the system;

- Linearity – The linear relationship between the measured quantity and the sensed one is desired, because the higher the linearity, the simpler to use.

These factors mentioned above are critical for sensors, consequently, they should be taken into accounts comprehensively when selecting materials, processing devices, and designing systems.

In this Chapter, we will first investigate the feasibility of temperature sensor based on CTGS, which means we will select samples with some specific orientations to sense the physical quantity–"temperature". Since our research focuses on the high-temperature sensors: the materials were tested at elevated temperatures and the devices are going to be used at high temperatures, the study of "temperature sensor" is very important and should be done with the highest priority. Because, on the one hand, with this study, the temperature of the specific location in the high-temperature related harsh environment where the sensor will be mounted will be monitored accurately and in real-time without an extra thermocouple; and on the other hand, when investigating other types of high-temperature sensors, e.g. high-temperature mass sensor and high-temperature pressure sensor, the effect of temperature on the sensor outputs (e.g. resonant frequency) needs to be subtracted first to extract the frequency-mass/pressure relation.

4.1 CTGS BAW TEMPERATURE SENSOR

4.1.1 The sensitivity of temperature sensor

As sensor's sensitivity indicates how much its output changes regarding to the input quantity being measured changes, and in the particular case of temperature sensor, the output and input are the resonant frequency and temperature, respectively, it is obvious that we should choose a relationship between the frequency and temperature to serve as the sensitivity. In addition to considering the fact that the resonant frequency differs with the vibration modes and dimensions of the devices, we will adopt the ratio of the rate of resonant frequency change to the temperature change as the sensitivity of temperature sensor, which can be written as:

$$-\frac{\Delta f}{f_0}\cdot\frac{1}{\Delta T} \qquad \textbf{(4-1)}$$

where f_0 is the intrinsic resonant frequency which was measured under room temperature, and the negative sign means the resonant frequency usually decrease with the rise of temperature.

4.1.2 Selection of the crystal cut for the temperature sensor

From the raw data used in Chapter 2 for the characterization of CTGS properties, we selected three kinds of samples as candidates due to their superior frequency-temperature linearity: X-cut (thickness mode), XY-cut (length extensional mode), and Y-cut (thickness shear mode), the regression coefficients of which are all larger than 0.99. Afterwards, to evaluate the stability of the candidate resonators, the repeated measurements of the selected samples were done for three

to four times with one-month interval. Figure 4-1, Figure 4-2, and Figure 4-3 respectively show the results of the linearity and stability tests of the three kinds of samples.

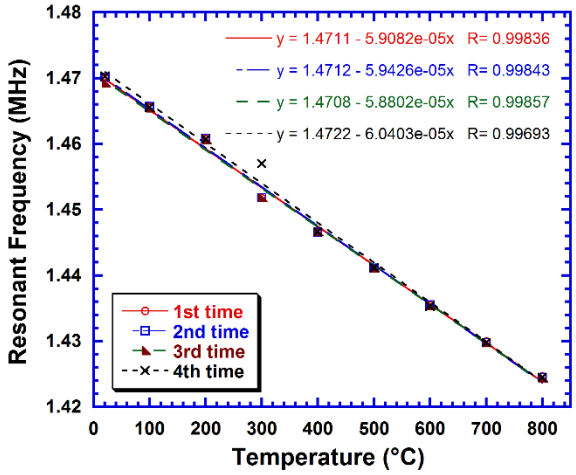

Figure 4-1. Four repeated test of CTGS X-cut thickness mode resonator.

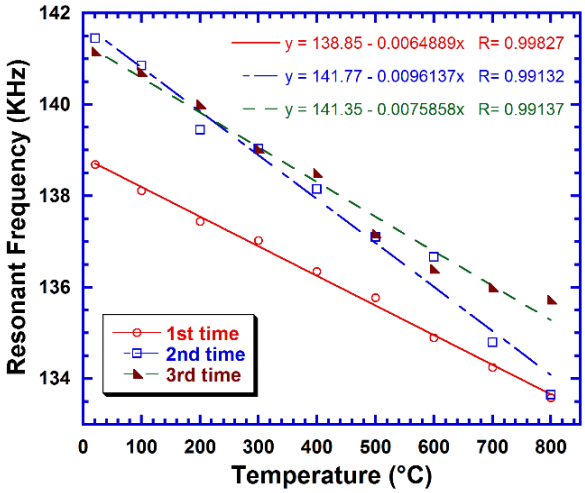

Figure 4-2. Three repeated test of CTGS XY-cut length extensional mode resonator.

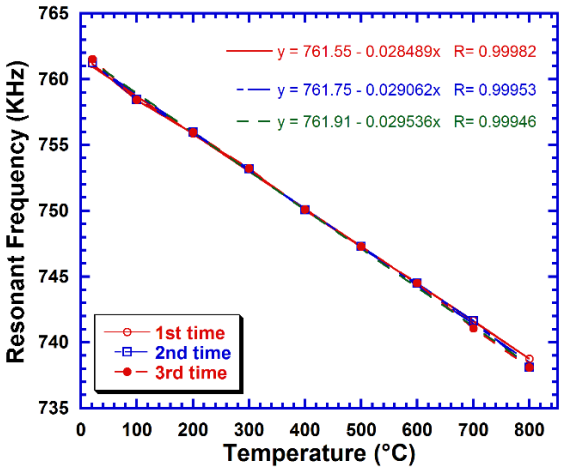

Figure 4-3. Three repeated test of CTGS Y-cut thickness shear mode resonator.

As can be seen from Figure 4-2, there are significant differences between the results of the three tests over two months of XY-cut resonator, indicating the long-term stability of XY-cut ample is relatively low. So, it is not suitable for the temperature sensor. By contrast, X-cut thickness mode and Y-cut thickness shear mode resonators show excellent stability. Especially the Y-cut, both the linearity and stability are perfect: regression coefficients R^2>0.999, and the results of the three frequency tests are substantially coincident in the range of 200 to 600°C.

The linearity, stability, and sensitivity of X-cut, XY-cut, and Y-cut resonators are summarized in Table 4-1. Y-cut has an advantage in linearity and stability, while X-cut is a bit higher in sensitivity. Therefore, on the whole, Y-cut thickness shear mode resonator is the optimal choice for temperature sensor.

Table 4-1. The linearity, stability, and sensitivity of XY-, X-, and Y-cut resonators of CTGS crystal.

Sample Cut	Linearity (R^2)	Stability	Sensitivity (10^{-3} °C^{-1})
XY-cut	0.991	Unsatisfactory	--
X-cut	0.998	Excellent	4.0
Z-cut	0.999	Perfect	3.9

4.1.3 Ultra-high temperature (1000°C) test of the CTGS Y-cut resonator

In order to meet the potential higher temperature requirements, we carried out the measurement for another Y-cut resonator from room temperature to 1000°C. Both the resonant frequency and anti-resonant frequency of the sample were recorded and their temperature dependence up to 1000°C are exhibited in Figure 4-4. Inspiringly, both the resonant and anti-resonant frequencies possess perfect linearity (R^2>0.999) to temperature, implying the feasibility of CTGS crystals for sensing applications under ultra-high temperatures.

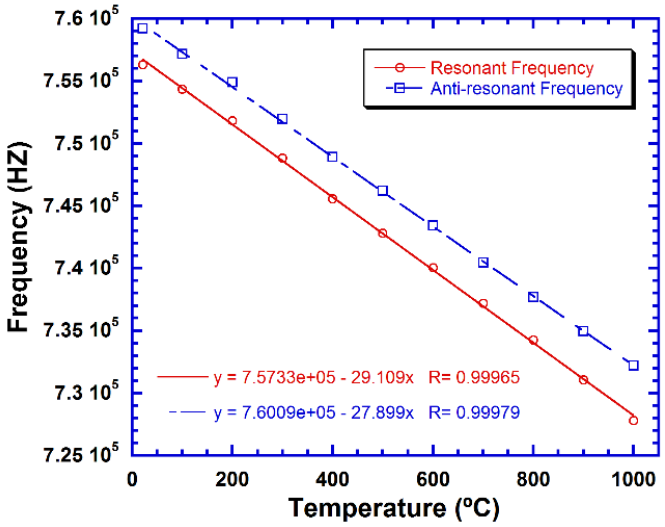

Figure 4-4. Resonant and anti-resonant frequencies test of CTGS Y-cut resonator up to 1000°C.

4.2 CONCLUSION

In conclusion, first we investigated the optimal sample cut choice of CTGS crystals for temperature sensors according to the linearity, stability, and sensitivity. After a comprehensive comparison, Y-cut thickness shear mode resonators were considered to be the best choice for temperature sensors due to their perfect linearity and stability. And then, we confirmed the feasibility of CTGS crystals for applications under ultra-high temperatures up to 1000°C.

5.0 HIGH-TEMPERATURE BAW MASS SENSOR FOR THERMOGRAVIMETRIC ANALYSIS OF NANO- AND MICRO-LAYERS OF POLYMER

5.1 BACKGROUND

As stated in Chapter 1, the acoustic wave (AW) sensors can response to a physical, chemical, or biological stimulus in a sensitive and real-time manner, so they have drawn increasing attraction in recent years. Among the AW sensors, the piezoelectric ones show a lot of extraordinary merits such as high resolution, wide frequency and temperature ranges, high stability, low power consumption, and low cost, and they are able to sense many physical and chemical quantities such as temperature, pressure, mass, gas concentration, and liquid viscosity [133, 136, 209]. To date, many surface acoustic wave (SAW) sensors [210], thin film bulk acoustic resonators (FBAR) [211], and bulk acoustic wave (BAW) [212] sensors have been reported as mass sensors. Compared to the former two types, BAW mass sensors are with the property of simple preparation process, easy to use, high temperature-tolerance, high repeatability and durability, and little damping, because neither the interdigitated transducers (IDTs) nor the functional piezoelectric thin film is needed. Therefore, piezoelectric BAW mass sensors that can be used at elevated temperature range are ideal devices for thermogravimetric analysis (TGA) applications.

The most widely used BAW mass sensor is the quartz crystal microbalance (QCM) [213, 214], which is based on the AT-cut thickness-shear mode (TSM) quartz resonator. AT-cut TSM

quartz crystals possess very high quality factor and stable oscillation, and are with extremely high sensitivity to the surface perturbation. Nonetheless, the high temperature (HT) usage of quartz is limited by the α-β phase transition (573°C), and further restricted by mechanical twinning (300°C), which is far from meeting the growing demands for HT in the aerospace, energy, and automotive industries. In last Chapter, the Y-cut CTGS crystals were shown to possess extremely high stability and temperature linearity in repeated high temperature tests. Therefore, in this Chapter, we will try to develop the high-temperature BAW mass sensor based on it to solve the high-temperature failure issue from which QCM suffers.

To measure the performance of the HT BAW mass sensor, the thermogravimetric analysis (TGA) method is usually adopted. TGA is an effective way to study the physical and chemical properties of materials as a function of increasing temperature. Accordingly, it can precisely provide information about lots of physical and chemical phenomena, such as vaporization, absorption, and decomposition, which are accompanied by weight loss or gain [215]. More importantly, The TGA technique has been successfully applied to determine the selected characteristics or analyze specific processes of many materials at the nano- and micro-scales [216-218]. In this Chapter, the CTGS Y-cut thickness shear mode resonators will be investigated as HT mass sensors through the TGA of nano- and micro- polymer mass layers. The Poly(methyl methacrylate) (PMMA) was adopted to form the nanolayer, and Polyimide was used to deposit the microscale layer.

5.2 EXPERIMENTAL PREPARATION AND METHOD

5.2.1 Measurement preparation

The CTGS Y-cut square plate samples with the dimension about 12.00×12.00×0.71 mm^3 were cut and polished. And then, 30 nm chrome (Cr) and 70 nm gold (Au) films were sputtered sequentially on the major surfaces to serve as the electrodes. Afterwards, the 950 (PMMA) A2 photoresists (Solids: 2% in Anisole, from MicroChem) were spin-coated in the desired area at the rate of 4000, 2000, and 1000 rpm for 60 s, followed by pre-baking at 180 °C for 120 s, to form 146, 196, and 286 nm thin layers, respectively. As for the polyimide, PI 2611 (from HD MicroSystems) was coated at the speed of 5000 rpm, followed by pre-baking at 130 °C for 90 s, resulting in 5280 nm mass layer.

As shown in Figure 5-1, both two major surfaces of the resonators were partially covered by electrodes (the active area was 6.54×5.89 mm^2), thereby only the middle area has electrodes on both sides, which confines the displacement field to the center of the crystal by the energy trapping theory. In addition, the PMMA and PI layers were coated slightly smaller than the middle area. Finally, four small grooves (two at each end) were opened for the convenience of extracting the electrodes with fine platinum wires. Figure 5-2 exhibits the thickness test results of the PMMA and PI layers by surface profiler (KLA Tencor Alpha Step IQ).

The same measurement system as shown in Figure 2-3 was employed for the TGA application, and the tests were carried out in the dry N_2 atmosphere with the flow rate of 100 mL/min, and the heating rate was 5°C/min.

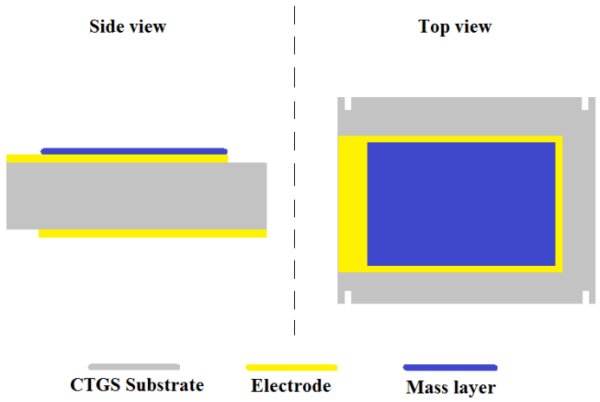

Figure 5-1. Schematic diagram of the CTGS HT BAW mass sensor with polymer mass loading.

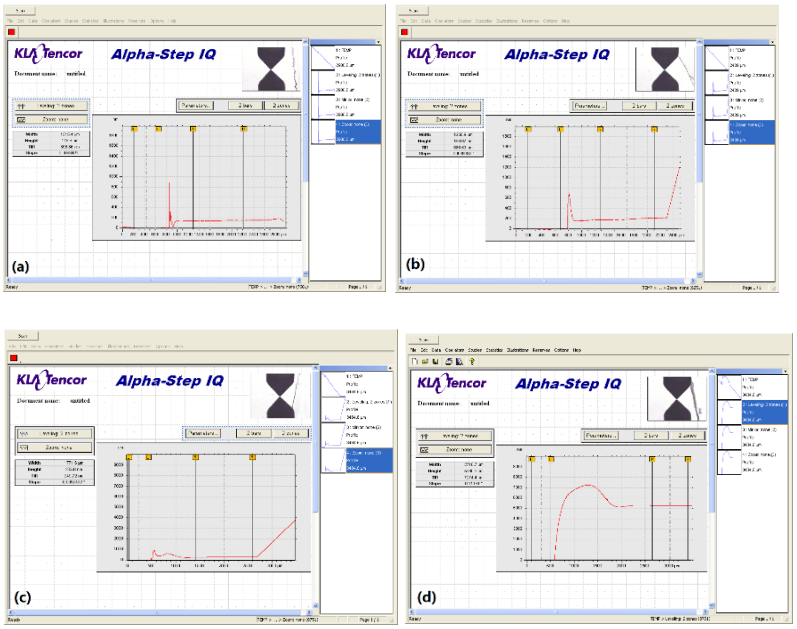

Figure 5-2. Thickness test results of the PMMA and PI layers at different coating speeds:

(a) PMMA at 4000 rpm-145.6 nm, (b) PMMA at 2000 rpm-196.07 nm, (c) PMMA at 1000 rpm-285.8 nm, (d) PI at 5000 rpm-5280.3 nm.

5.2.2 Method

5.2.2.1 Definition of mass sensitivity

Since we monitor the mass change through the frequency shift of the resonators, hereby we define the sensitivity of the mass sensor "*S*" to be:

$$S = -\frac{\Delta f}{\Delta m} \quad \textbf{(5-1)}$$

where Δf and Δm represent frequency shift of the resonator and mass change, respectively. And The minus sign here is because the mass loading usually results in a reduction in the resonant frequency.

5.2.2.2 Mass sensitivity analysis

The TSM QCM is the most widely used micro-weight mass sensor, which typically consists of a thin AT-cut quartz disk with circular electrodes deposited at the center of both sides and can be electrically excited in thickness-shear modes. When the mass is deposited onto the electrode of one side, the electrically-excited acoustic-wave propagation, e.g. the resonant frequency, could change accordingly through entire quartz crystal [219].

The displacement u_x in the crystal is a superposition of the waves propagating through it:

$$u_x(y,t) = (A\mathrm{e}^{jky} + B\mathrm{e}^{-jky})\mathrm{e}^{jwt} \quad \textbf{(5-2)}$$

where *A* and *B* are constants, and ω, *k*, and *t* are angular excitation frequency, wavenumber, and time, respectively. A round-trip phase shift of the acoustic wave is

$$\Delta\phi = 2kh_s + 2\pi \quad \textbf{(5-3)}$$

where h_s is the thickness of the resonator. And when $\Delta\phi$ is an integer multiple of 2π, the crystal will resonant. Because

$$k = 2\pi / \lambda = \omega / v_s \tag{5-4}$$

where λ is the acoustic wavelength and v_s is the shear wave velocity, we can obtain

$$h_s = N(\frac{\lambda}{2}), \quad f_N = \frac{Nv_s}{2h_s} \tag{5-5}$$

Moreover, the shear wave phase velocity v_s in the crystal in given by

$$v_s = (\frac{\mu_q}{\rho_q})^{1/2} \tag{5-6}$$

where μ_q and ρ_q are the shear stiffness and mass density of the substrate crystal, respectively. When both faces of the crystal are stress-free, the displacement in (5-2) can be expressed by

$$u_x(y,t) = u_{x0}\cos(k_N y)\,\mathrm{e}^{j\omega t} \tag{5-7}$$

where u_{x0} is the surface displacement and k_N=$N\pi/h_s$.

When mass accumulates on the surface, the resonant frequency will change to rebalance the kinetic and potential energies. The peak kinetic energy density is

$$U_k = \frac{\omega^2}{2}(\rho_s u_{x0}^2 + \rho_q \int_0^{h_s} \left|u_x(\mathrm{y})\right|^2 \mathrm{dy}) \tag{5-8}$$

where ρ_s is the areal mass density (mass/area) of the mass loading layer and ρ_q is the volume mass density of the substrate crystal. From (5-7) and (5-8), we can get

$$U_k = \frac{\omega^2 u_{x0}^2}{2}(\rho_s + \frac{\rho_q h_s}{2}) \tag{5-9}$$

And the peak potential energy density is

$$U_p = \frac{1}{2}\mu_q k^2 u_{x0}^2 \int_0^{h_s} \sin^2(\mathrm{ky})\,\mathrm{dy} = \frac{\mu_q k^2 u_{x0}^2 h_s}{4} \tag{5-10}$$

Through balancing the peak kinetic energy density and the peak potential energy density, the following relation can be obtained

$$(\frac{\omega_0}{\omega})^2 = 1 + \frac{2\rho_s}{h_s\rho_q} \quad \textbf{(5-11)}$$

For $\rho_s \ll h_s\rho_q$, (5-11) can be expressed in a linear relationship:

$$\frac{\Delta f}{f_0} = -\frac{\rho_s}{h_s\rho_q} \quad \textbf{(5-12)}$$

Combining (5-5), (5-6), and (5-12), the Sauerbrey equation which has been widely recognized as a very effective equation for determining the frequency of a piezoelectric crystal with the mass deposited on it since its development by G. Sauerbrey in 1959 can be written as:

$$\Delta f = -\frac{2f_0^2\rho_s}{\sqrt{\rho_q\mu_q}} = -\frac{2f_0^2}{A_s\sqrt{\rho_q\mu_q}}\Delta m \quad \textbf{(5-13)}$$

Thus, according to (5-1) and (5-13), the sensitivity of the TSM mass sensor can be related to the properties of the substrate crystal by

$$S = \frac{\Delta f}{\Delta m} = \frac{2f_0^2}{A_s\sqrt{\rho_q\mu_q}} \quad \textbf{(5-14)}$$

To apply this equation, the piezoelectric crystal-mass system should meet the following three conditions: the mass layer should be rigid, the mass must be deposited evenly, and the frequency change $\Delta f/f$ < 0.02. The first two conditions can be met through the spin-coating and pre-baking processes, and the last one will be demonstrated later.

5.2.2.3 Experimental procedure

In this work, firstly, we deposited the same thicknesses of target mass loadings onto the active area of standard QCMs (from International Crystal Manufacturing, Oklahoma City, OK) to demarcate the areal mass densities (mass/area) of the mass loading layers: ρ_s. The basic parameters of the standard QCMs are as follows: volume mass density ρ_q is 2.651×10^3 kg/m^3,

active area A_q is 2.047×10^{-5} m^2, thickness of the TSM resonator h_q is 165 μm, and the resonant frequency is 10 MHz. Therefore, through measuring the resonant frequency f_0 (when no mass deposited) and the frequency shifts Δf resulted from the mass layers of the QCMs, ρ_s can be determined by (5-12).

Because the areal mass densities on Quartz and CTGS resonators are the same, the weight of the mass layers deposited on TSM CTGS can be obtained by

$$\Delta m = A_s \rho_s \quad \textbf{(5-15)}$$

where A_s=$6.54\times5.89=3.852\times10^{-5}$ m^2.

Finally, the frequency shifts Δf resulted from the mass layers of the TSM CTGS resonator can be measured by the impedance analyzer. Consequently, the sensitivity of the CTGS TSM mass sensor can be obtained by (5-1).

5.3 RESULTS AND DISCUSSION

5.3.1 PMMA nanolayers

Figure 5-3 and Figure 5-4 illustrate the changes of admittance resulted from different PMMA mass layers of TSM Quartz and CTGS resonators, respectively. The relationship between the resonant frequencies and the thickness of PMMA mass layers was extracted and shown in Figure 5-5. Obviously, the resonant frequencies of both Quartz and CTGS resonators shift downwards linearly with the increase of the mass layer thickness. Then, the areal mass density ρ_s of the PMMA layers can be determined by (5-12) with the information of quartz resonator, which is about 1.1×10^{-4} kg/m^3 for the 146 nm layer. Furthermore, the weight of the deposited 146 nm

PMMA on CTGS resonator $\Delta m=\rho_s \times A_c$=4.22 μg. Therefore, the mass sensitivity of TSM CTGS resonator obtained from the 146 nm mass layer can be obtained by (5-1), which is about 24 Hz/μg. Similarly, the mass sensitivity can be verified by the other two thicknesses of PMMA layers, which are pretty close to this value.

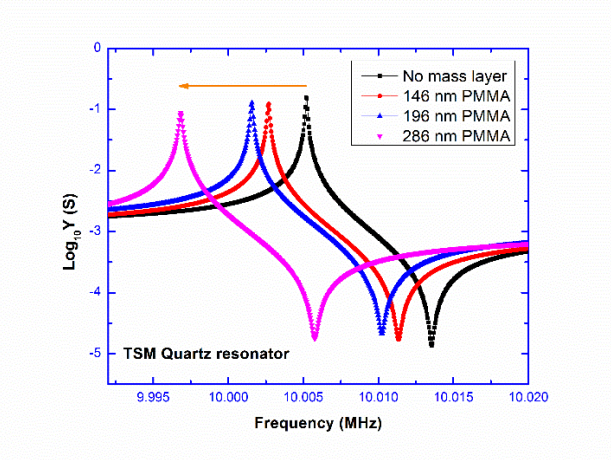

Figure 5-3. Admittance of the TSM quartz resonator with different PMMA mass layers versus frequency.

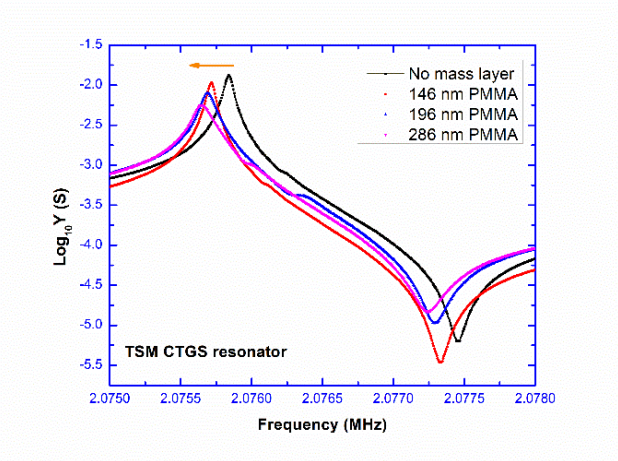

Figure 5-4. Admittance of the TSM CTGS resonator with different PMMA mass layers versus frequency.

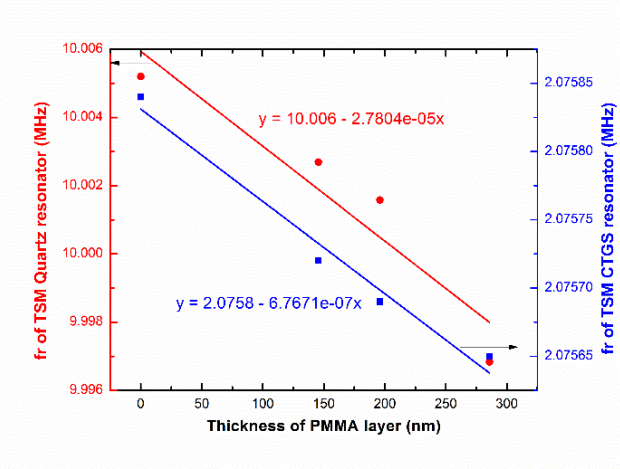

Figure 5-5. Resonant frequencies of Quartz (red) and CTGS (blue) resonators versus thicknesses of PMMA layers.

To implement the TGA tests, first of all, the TSM CTGS resonator without mass loading was measured from room temperature to 460°C, and the resonance spectrum (Y-θ) was recorded as a reference. Then, the resonance spectrum (Y-θ) of the CTGS resonator with a mass layer on the surface was measured again under the same conditions. Thus, the difference of the resonant frequencies at the same temperature which resulted from the mass layers can be used to reflect the weight changes during the decomposition process of PMMA.

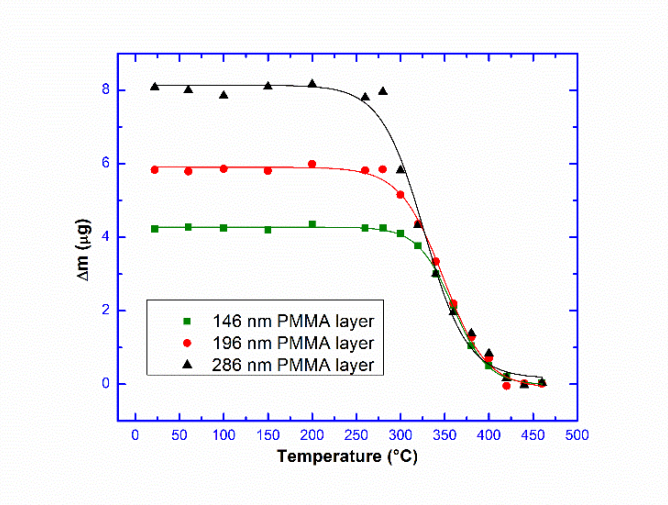

Figure 5-6. TGA test of TSM CTGS mass sensor with different PMMA mass layers.

Figure 5-6 exhibits the results of the TGA tests for 146, 196, and 286 nm PMMA mass layers. As one can see, the CTGS mass sensor accurately detected the decomposition process of the PMMA layers which occurred in the range of 300 to 400 °C. Before 300°C, the weights of the mass layers remained basically the same. When the decomposition temperature of PMMA was reached, the amount of remaining mass drastically decreases until all PMMA thin film decomposed and no further mass change observed. Therefore, the TSM CTGS resonator is a very effective mass sensing device for thermogravimetric analysis application.

5.3.2 Polyimide microlayer

To demonstrate the feasibility of CTGS BAW mass sensor at even higher temperatures, 5280-nm polyimide (PI) layer was deposited as the mass loading and the TGA test was carried out up to 800°C, the result is shown in Figure 5-7. Knowing that the decomposition of PI usually occurs in the range of 500 to 600 °C, the result in Figure 5-7 gave a perfect interpretation to this process.

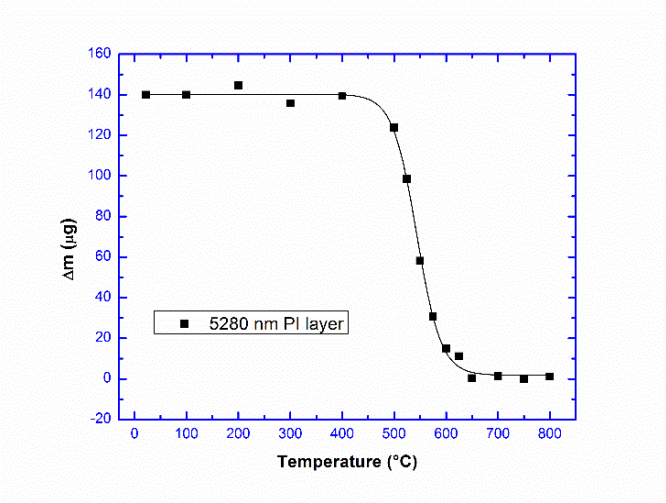

Figure 5-7. TGA test of TSM CTGS mass sensor with 5280 nm Polyimide mass layer.

Finally, the resonant frequency of 0.71 mm Y-cut TSM CTGS resonator at room temperature was about 2.076 MHz, while the frequency change caused by the 5280 nm PI layer was only about 3300 Hz, demonstrating the condition of $\Delta f/f < 0.02$ was satisfied. The frequency changes resulted from the PMMA thin film layers are much smaller, in the range of 100 to 200 Hz, which obviously satisfied this condition.

5.4 CONCLUSION

In summary, the CTGS Y-cut TSM resonator with the dimension of 11.97×11.93×0.71 mm^3 was investigated as high-temperature mass sensor for thermogravimetric analysis. The TSM with the 2.076 MHz resonant frequency at room temperature was employed as the sensing mode, which is very similar to the widely used QCM sensors. The TGA technique was used to evaluate the performance of the mass sensor. 146, 196, and 286 nm PMMA mass layers, and 5280 nm PI

layer were adopted as the mass loadings, respectively. It was demonstrated that the CTGS mass sensor used in this work was able to detect accurately the mass changes of the thin film mass layers in a wide temperature range up to 800°C with the sensitivity about 24 HZ/μg. Furthermore, it is worth mentioning that there is still a great potential to improve the mass sensitivity by reducing the thickness of the CTGS resonator.

6.0 NONLINEAR EFFECTS AND HIGH-TEMPERATURE PRESSURE SENSOR

6.1 NONLINEAR EFFECTS IN PIEZOELECTRIC CRYSTALS

As clearly stated at the beginning of Chapter 2, the IEEE methods used for the determination of the dielectric, elastic, and piezoelectric coefficients are only applicable to linear (dielectric, piezoelectric and elastic coefficients are considered as constants independent of the applied electric fields and mechanical stresses) and low-loss (electrical and mechanical dissipations could be neglected) piezoelectric materials. Although the CTGS and YCOB single crystals can be undoubtedly treated as linear and low-loss materials, the study of their non-linearity and dissipations will improve our understanding of them and expand the relevant new applications. The loss-related issues of the two crystals have been addressed through Du, Wang, and Uchino's methods by introducing the imaginary part for each coefficient in Chapter 2 and 3, respectively. In this Chapter, we will focus on the non-linearity, as well as a related important application-pressure sensor.

First of all, let's take a brief review of the basic linear theory of piezoelectricity. From a mechanical point of view, the stress-strain relationship of linear piezoelectric materials follows the Hooke's law, denoted by (1-8) $T_i=c_{ij}S_j$. And under electrical considerations, the electric displacement relates to the electric field by (1-2) $D_i=\varepsilon_{ik}E_k$. Furthermore, the mechanical and electrical quantities are coupled by direct or converse piezoelectric effect, which can be derived

from (1-13): D_i=$e_{ip}S_p$ and T_p=$e_{ip}E_i$. Finally, when taking into account the specific boundary conditions, we can obtain one typical form of the constitutive equations of the linear piezoelectric medium:

$$\begin{aligned} T_i &= c_{ij}^E S_j - e_{ki} E_k \\ D_i &= e_{ij} S_j + \varepsilon_{ik}^S E_k \end{aligned} \tag{6-1}$$

However, the constitutive equations will become very complicated when considering the nonlinear phenomena in crystals which are numerous and related to different kinds of interaction processes [220]:

$$\begin{aligned} T_i = {} & c_{ij}S_j + \frac{1}{2}c_{ijk}S_jS_k + \frac{1}{6}c_{ijkl}S_jS_kS_l + \cdots \\ & - e_{mi}E_m - \frac{1}{2}e_{mn,i}E_mE_n - e_{m,ij}E_mS_j \\ & - \frac{1}{2}e_{m,ijk}E_mS_jS_k - \frac{1}{2}e_{mn,ij}E_mE_nS_j - \frac{1}{6}e_{mnp,i}E_mE_nE_p - \cdots \end{aligned} \tag{6-2}$$

$$\begin{aligned} D_h = {} & e_{hj}S_j + e_{hm,j}E_mS_j + \frac{1}{2}e_{h,jk}S_jS_k + \frac{1}{6}e_{h,jkl}S_jS_kS_l \\ & + \frac{1}{2}e_{hm,jk}E_mS_jS_k + \frac{1}{2}e_{hmn,j}E_mE_nS_j + \cdots \varepsilon_{hm}E_m \\ & + \frac{1}{2}\varepsilon_{hmn}E_mE_n + \frac{1}{6}\varepsilon_{hmnp}E_mE_nE_p + \cdots \end{aligned} \tag{6-3}$$

where c_{ij}, c_{ijk}, and c_{ijkl} are the second, third, and fourth order of elastic constants, respectively; ε_{hm}, ε_{hmn}, and ε_{hmnp} are the second, third, and fourth order of dielectric constants; e_{mi} is the second order piezoelectric constant, $e_{mn,i}$ and $e_{m,ij}$ are the third order ones, and $e_{m,ijk}$, $e_{mn,ij}$, and $e_{mnp,i}$ are those of the fourth order. The comma in the high orders of piezoelectric constants is employed to avoid the possible confusion between the subscripts that correspond to the strains and those to the electric fields. The subscripts to the left of the comma relate to the electric fields, while those to the right are with respect to the strains. And (6-2) and (6-3) are obtained without

considering the damping. The most widely known non-linear effect is the electrostrictive effect, which is represented by the $d_{i,mn}$ type of coefficients (S_i=$d_{i,mn}S_mS_n$) and are found in lots of ceramics and crystals.

Usually, the dielectric, elastic, and piezoelectric constants are defined by the free energy expression [220]:

$$\Phi = \Phi_{electric} + \Phi_{elastic} + \Phi_{piezoelectric} \tag{6-4}$$

where the electric, elastic, and piezoelectric energies are written in terms of the power terms of the electric fields, strains, and the products of them, respectively.

$$\begin{aligned}
\Phi_{electric} &= -\frac{1}{2}\varepsilon_{ij}E_iE_j - \frac{1}{6}\varepsilon_{ijk}E_iE_jE_k - \frac{1}{24}\varepsilon_{ijkl}E_iE_jE_kE_l - \cdots - \frac{1}{n!}\varepsilon_{ij\cdots n}E_iE_j\cdots E_n \\
\Phi_{elastic} &= \frac{1}{2}c_{ij}S_iS_j + \frac{1}{6}c_{ijk}S_iS_jS_k + \frac{1}{24}c_{ijkl}S_iS_jS_kS_l + \cdots + \frac{1}{n!}c_{ij\cdots n}S_iS_j\cdots S_n \\
\Phi_{piezoelectric} &= -e_{im}E_iS_m - \frac{1}{2}e_{ij,\mathrm{m}}E_iE_jS_m - \frac{1}{2}\varepsilon_{i,\mathrm{mn}}E_iS_mS_n - \cdots
\end{aligned} \tag{6-5}$$

The number of non-zero and independent coefficients increases rapidly with the order, for the crystals in trigonal system and point group 32, e.g. Quartz and CTGS, the numbers of the second, third, and fourth order coefficients are summarized in Table 6-1 [220].

Table 6-1. The number of second, third, and fourth order nonzero/independent dielectric, elastic, and piezoelectric constants of CTGS crystals.

Number of nonzero/independent constants	Dielectric	Elastic	Piezoelectric
2nd order	3/2	18/6	5/2
3rd order	2/1	31/14	41/16
4th order	8/4	69/23	--

So far, the high order (third and fourth) coefficients related to the non-linearity of Quartz have not yet been fully studied, and those of CTGS and YCOB are less documented in the literature. Usually, there are two ways to investigate the non-linearity of the crystals, one is to apply the DC bias, and the other is to apply forces/stresses to the crystal resonators. Next, we will launch research in these two aspects focusing on TSM CTGS Y-cut resonator.

6.2 INVESTIGATION OF THE NON-LINEARITY EFFECTS BASED ON THE DC BIAS FIELDS

Just like the electrostrictive effect, when the piezoelectric devices are subjected to certain electric fields, some of their important properties, e.g. dielectric permittivity, dielectric loss, piezoelectric constants and so on, may significantly change, especially for the ferroelectric materials [221-225].

The applied DC bias fields may lead to the frequency shift of the piezoelectric resonator which is due on the one hand to the crystal dimension change that is considered to be corresponding to the usual linear piezoelectric effect and, on the other hand to the quadratic variation that corresponds to the non-linear effect [220]. Consequently, the investigation of the non-linearity of CTGS crystals under DC bias fields will be conducive to more comprehensive understanding of this material, and to the development of some potential applications, e.g. using DC bias to tune materials properties [225].

6.2.1 Non-linear effects in CTGS Y-cut TSM resonator

For the CTGS Y-cut TSM resonator (11.99×11.94×2.00 mm^3, the active area 7.24×6.42 mm^2) with the electric fields applied along the Y direction, the fundamental equations are [220]:

$$T_6 = C_{66}S_6 + \frac{1}{6}C_{6666}S_6^3 - e_{26}E_2 - \frac{1}{6}e_{222,6}E_2^3 - \frac{1}{2}e_{22,66}E_2^2S_6 - \frac{1}{2}e_{2,666}E_2S_6^2 \quad \textbf{(6-6)}$$

$$D_2 = e_{26}S_6 + \frac{1}{2}e_{222,6}E_2^2S_6 + \frac{1}{2}e_{22,66}E_2S_6^2 + \frac{1}{6}e_{2,666}S_6^3 + \varepsilon_{22}E_2 + \frac{1}{6}\varepsilon_{2222}E_2^3 \quad \textbf{(6-7)}$$

$$\rho\frac{\partial^2 u}{\partial t^2} = \frac{\partial T_6}{\partial y} \quad \textbf{(6-8)}$$

$$I = S\frac{\partial D_2}{\partial t} \quad \textbf{(6-9)}$$

$$\frac{\partial D_2}{\partial y} = 0 \quad \textbf{(6-10)}$$

(6-6) and (6-7) show that the related high order coefficients are the fourth order ones, which is because in this specific case, the third order coefficients are zero:

$$C_{666} = 0, \quad e_{2,66} = 0, \quad e_{22,6} = 0, \quad \varepsilon_{222} = 0 \quad \textbf{(6-11)}$$

And (6-10) illustrates the space charges are ignored.

By solving the wave propagation equation and taking into account the specific boundary conditions, the expression illustrating the frequency difference as a function of the current amplitude (I_0) can be obtained (please refer to page 267 to 287 of [220]):

$$f = f_0\left(1 + \frac{3n^2}{256}\frac{c_{6666}^D}{c_{66}^D}\frac{\pi^2 I_0^2}{e_{26}^2 S^2 \omega_0^2}\right) \quad \textbf{(6-12)}$$

where n is the overtone rank, and S is the active area. Similarly, the capacitance difference can be expressed by the current amplitude through

$$C = C_0(1+\frac{n^4}{512}\frac{\varepsilon_{2222}}{\varepsilon_{22}}\frac{\pi^4(c_{66}^D)^2 I_0^2}{e_{26}^2 Q^2 S^2 \omega_0^2}) \quad \textbf{(6-13)}$$

where Q is the quality factor. (6-12) can be employed to determine c_{6666}^D and f_0 by measuring resonant frequencies and current amplitudes at two overtones through the impedance analyzer, and (6-13) can be used to obtain ε_{2222} and C_0 through the measurement of the capacitances, quality factors, and current amplitudes at two overtones. The spectrum near the first, third, and fifth overtones are shown in Figure 6-1, the resonant frequencies of which are about 789.6082 kHz, 2.2444763 MHz, and 3.7431115 MHz, respectively. And the calculated results of the fourth order coefficients are shown in Table 6-2. The c_{6666}^D is in the order of 10^{14} N/m^2, and ε_{2222} is in the order of 10^{-25} F·m/V^2.

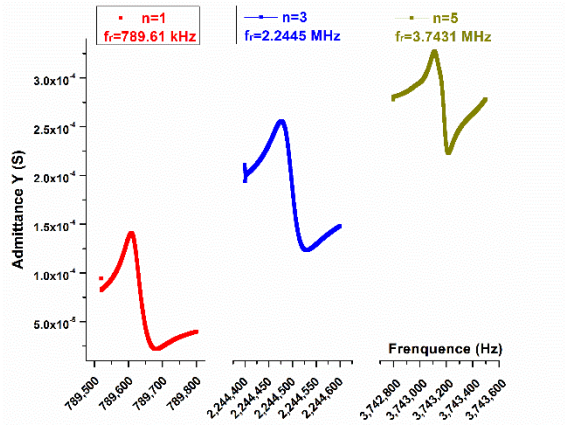

Figure 6-1. The spectrum near the first, third, and fifth overtones of the CTGS Y-cut TSM resonator.

Table 6-2. The fourth order coefficients of the CTGS crystal.

	n= 1 & 3	n= 1 & 5	n= 3 & 5
c^D_{6666} ($\times 10^{14}$ N/m^2)	4.40	3.26	5.22
ε_{2222} ($\times 10^{-25}$ F·m/V^2)	-2.89	-1.96	-1.64

6.2.2 Influence of the DC bias field

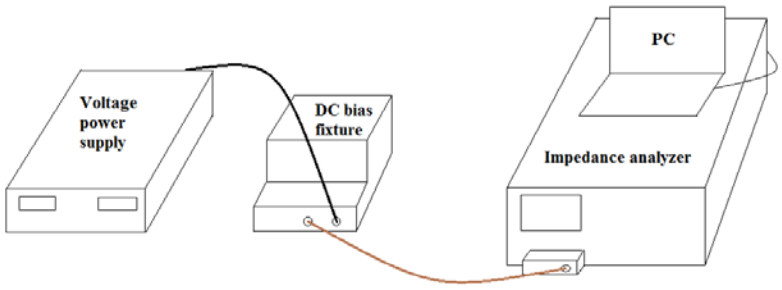

Figure 6-2. The schematic diagram of the DC bias fields measurement system setup.

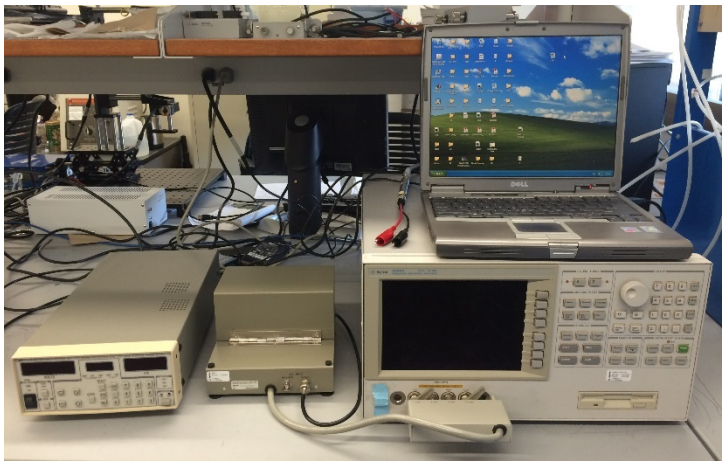

Figure 6-3. The photograph of the actual DC bias measurement system.

Figure 6-2 shows the schematic diagram of the DC bias fields system setup and Figure 6-3 exhibits the photograph of the actual system. The CTGS Y-cut resonator was tested inside the DC bias fixture (Agilent 16065A) with the voltage power supply (SRS PS325) providing the input DC voltages and the impedance analyzer acquiring the spectrum near the resonant frequencies. According to the previous analysis, the applied DC bias will lead to the frequency shift of the resonator. In this measurement, the range of the applied DC bias was from -180 to 180 V. The frequency variation versus the applied DC bias field is shown in Figure 6-4.

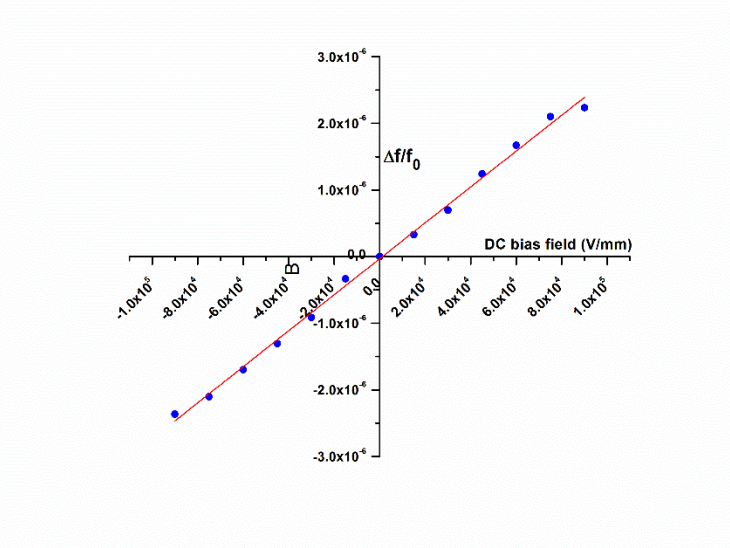

Figure 6-4. The frequency variation of the CTGS Y-cut TSM resonator versus the DC bias field.

As can be seen from Figure 6-4, the frequency variation is very linear, and if we use a second-order polynomial to fit the data, it will be:

$$\Delta f / f_0 = 2.697 \times 10^{-11} E - 8.033 \times 10^{-19} E^2 \qquad \textbf{(6-14)}$$

And it was demonstrated that [220]:

$$\frac{1}{E^2}\frac{df}{f} \simeq \frac{1}{4}\left[c_{6666}^{D} \frac{{e_{26}}^2}{(c_{66}^{D})^3} + h_{22,66}^{*} \frac{{\varepsilon_{22}}^2}{c_{66}^{D}} \right] \quad \textbf{(6-15)}$$

where

$$h_{22,66}^{*} = h_{22,66} + 2h_{2,666}\frac{e_{26}}{\varepsilon_{22}c_{66}^{D}} + 16h_{222,6}\frac{e_{26}}{\pi^2} - 8\varepsilon_{2222}\frac{{e_{26}}^2}{\pi^2{\varepsilon_{22}}^2} \quad \textbf{(6-16)}$$

Thus,

$$\frac{1}{4}\left[c_{6666}^{D} \frac{{e_{26}}^2}{(c_{66}^{D})^3} + h_{22,66}^{*} \frac{{\varepsilon_{22}}^2}{c_{66}^{D}} \right] \simeq -8.033\times10^{-19} \quad \textbf{(6-17)}$$

From (6-17), the fourth order coefficient $h_{22,66}^{*}$ can be obtained:

$$h_{22,66}^{*} \simeq -6.87\times10^{12}\ m/F$$

Similar to the characterization of the second order coefficients in Chapter 2 and 3, the determination of more high-order (third and fourth) coefficients requires the measurements of numerous of samples with different orientations and vibration modes.

6.3 FORCE-FREQUENCY EFFECT AND PRESSURE SENSOR

6.3.1 Force-frequency effect in piezoelectric materials

Analog to the frequency drift driven by the electrical fields discussed in the previous section, the applied external mechanical fields (force/stress) will also lead to the frequency change of the piezoelectric materials, which is due to the non-linear elastic responses. This phenomenon is called force-frequency effect and was first discovered by Bottom in 1947 [226], who reported the frequency change of the quartz resonator when it was squeezed by an external force. After that,

Bottom [227] further pointed out that the change in crystal frequency (Δf) is linearly proportional to the applied external force (F), and this conclusion was confirmed by many other researchers later, such as Ballato [228, 229], and Mingins [230]. And all of their researches are based on the Quartz crystal. On the basis of these previous work, to get the direct force sensitive, Ratajski [231, 232] listed every possible influencing factor, including crystal material, crystal orientation, vibration mode, electrode diameter (for circular samples), temperature, crystal drive level, stress distribution factor, and a design factor related to the force points, and he basically checked and verified each parameter to see whether they had an impact on the force sensitivity. He only investigated the crystalline Quartz at constant temperature and constant drive level, which were initially proved to have no effect on the force sensitivity by Ballato. Furthermore, Mingins pointed out that the force sensitivity was independent of electrode diameter. Finally, Ratajski summarized the expression of the force sensitivity K_f:

$$K_f(\psi,\vartheta)=\frac{\Delta f}{f_0}\frac{1}{F}\frac{D}{f_0} \tag{6-18}$$

where ψ is the rotated angle of the Y-cut Quartz about X-axis, θ is the angle between the applied force and X-axis, F is the applied force, and D is the diameter for the circular sample. Afterwards, this empirical formula was widely recognized and K_f was called the force-frequency coefficient. Up to now, the force-frequency effect of many piezoelectric ceramics and crystals have been extensively investigated [233-240].

However, (6-18) is only an empirical formula based on experiments. To get a more complete and thorough understanding of the force-frequency effect, the theoretical analysis is essential. The theoretical problem can be classified as part of the general theory of incremental elastic deformations superposed on initial finite deformations [241], the general theory of which was developed by Green *et al.* [242] and many other researchers supplemented and expanded it

later [243-245]. All these pre-studies are concerned with infinite elastic media. On this basis, Lee *et al.* [241, 246-248] derived a system of six two-dimensional plate equations for the small motions superimposed on finite elastic body under initial stresses. In his derivation process, the third-order elastic coefficients were involved in the stress-strain relations. And they proposed an explicit formula to predicting the frequency variations caused by the external force/stress of rotated Y-cut TSM resonator:

$$\frac{\Delta f}{f_0} = S_{initial} + \frac{1}{2c_{66}}\left(c_{166}S_1 + c_{266}S_2 + c_{366}S_3 + c_{466}S_4\right) \quad \textbf{(6-19)}$$

where $S_{initial}$ is the initial strain; c_{166}, c_{266}, c_{366}, and c_{466} are the third-order elastic coefficients; S_1, S_2, S_3, and S_4 are the strain components result from the applied external force/stress. It is obvious that the frequency change is linearly proportional with the strain components, in turn, linear with the magnitude force/stress. It was demonstrated that the computational results according to (6-19) agreed very well with the experimental ones [241].

In the case of CTGS Y-cut TSM resonator (ψ=0), if the force/stress is applied along the X direction (θ=0), (6-19) will be:

$$\frac{\Delta f}{f_0} = S_1 + \frac{1}{2c_{66}}\left(c_{166}S_1 + c_{266}S_2 + c_{366}S_3 + c_{466}S_4\right) \quad \textbf{(6-20)}$$

And if the force/stress is applied along the Z direction (θ=90°), it will be:

$$\frac{\Delta f}{f_0} = S_3 + \frac{1}{2c_{66}}\left(c_{166}S_1 + c_{266}S_2 + c_{366}S_3\right) \quad \textbf{(6-21)}$$

There is no $c_{466}S_4$ term in (6-21), which is because the c_{34} of CTGS crystal is zero, resulting in the absence of S_4. (6-20) and (6-21) will be employed to investigate the pressure sensors based on CTGS Y-cut TSM resonators in the following section.

6.3.2 CTGS Y-cut TSM high-temperature pressure sensor

6.3.2.1 Measurement system setup

In order to verify the feasibility of the high-temperature pressure sensor based on the CTGS Y-cut resonator and calibrate the pressure sensitivity, we designed and processed the pressure tubing as shown in Figure 6-5.

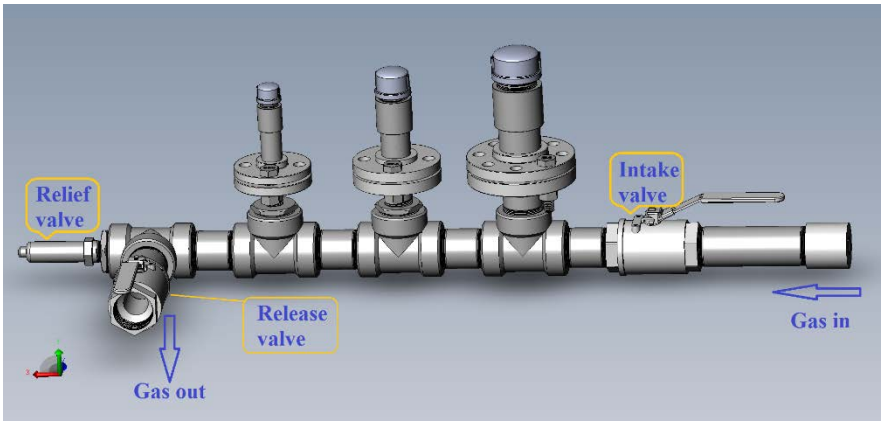

Figure 6-5. Schematic diagram of the pressure tubing for the test of high-temperature pressure sensor**.**

The tubing system consists of three branches, three valves, and some necessary connecting parts, most of which are made of 304 stainless steel. Among the three valves, one is the intake valve, one is the release valve, and the other one is the relief valve. Both the intake and release valves are ball valves, which can be turned on and off instantly. The relief valve was designed to prevent excessive pressure in the pipe, which is closed when the pressure is below 225 PSI (1551 kPa), but will automatically open to unload the pressure when it exceeds 225 PSI. The inlet of the tube will connect to a N_2 tank with a regulator to adjust the target pressure. Before inflating, close the release valve and open the intake one. Then, open the switch of the N_2

tank and get the desired pressure through the regulator. The inflatable process is very fast. After the pressure inside the tube reaches the target value, it will remain there if there is no other action and one can implement the required tests, and if a higher pressure is wanted, one only needs to continue to adjust the regulator. After all the tests have been done, close the switch of the tank and open the release valve to deflate.

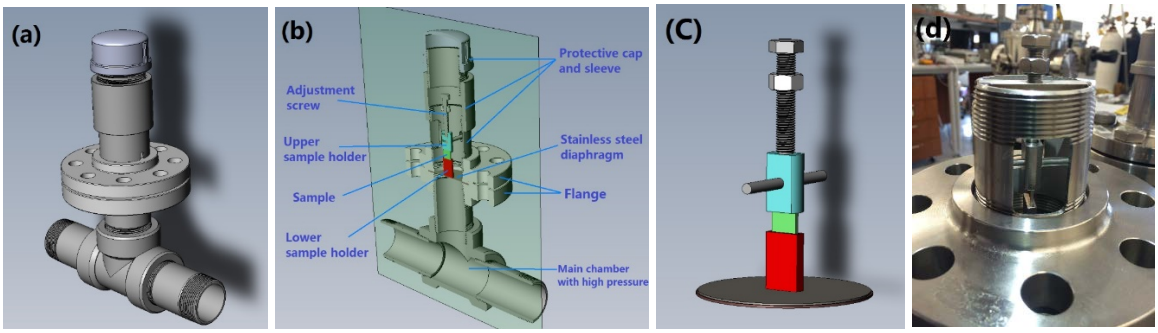

Figure 6-6. (a) Schematic diagram of one branch of the pressure tubing, (b) cross section of the branch, (c) the internal structure of the branch, and (d) photograph of the branch without the protective parts.

The three branches are with the same structure, but differ in the dimension. Figure 6-6.(a) schematically shows the structure of one branch and Figure 6-6.(b) presents its cross section. As one can see, each branch has a flange, at the middle of which we will place a stainless steel diaphragm and use a gasket and screws to seal and clamp the whole part. Above the flange and diaphragm, there are protective cap and sleeve to avoid the potential danger caused by the rupture of the diaphragm, although the possibility is very low. The internal structure of the branch is shown in Figure 6-6.(c). From bottom to up, there are diaphragm, lower sample holder, sample, upper sample holder, and the adjustment screw of the upper sample holder. The screw can be used to adjust the height of the upper sample holder to load and unload the sample, and it

is fixed with a beam as exhibited in Figure 6-6.(d). In this case, once inflating the pressure tubing, there will be a pressure difference between the two sides of the diaphragm because the part above the diaphragm is connected to the atmosphere, and further producing a force to the fixed objects above the diaphragm. In other words, the sample will be under a force/stress field.

6.3.2.2 System modeling

To find the clear correlation between the resonant frequency variation of the sample and the pressure difference on the two sides of the diaphragm, three steps are needed.

The first step is to establish the relationship between the pressure difference and the induced force, which can be obtained through the decomposition and respective analysis of the system. First of all, let's only consider the diaphragm under a uniform stress, as shown in Figure 6-7, where ΔP is the pressure difference, r is the radius of the free part of the diaphragm, and t is the diaphragm thickness.

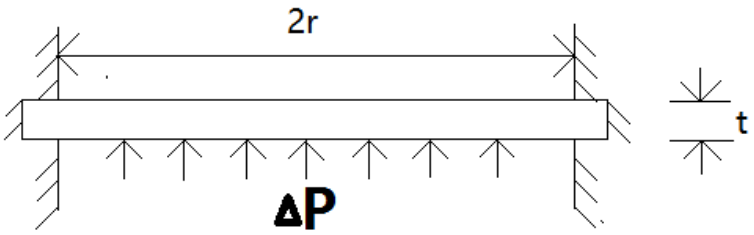

Figure 6-7. Schematic diagram of the edge clamped circular plate under uniform load.

It is well known that the maximum stress (σ_m) of the diaphragm will appear at the edges:

$$\sigma_m = \frac{3\Delta P r^2}{4t^2} \tag{6-22}$$

And the maximum deflection (y_m) will occur at the center:

$$y_m = \frac{\Delta P r^4}{64D} \tag{6-23}$$

where D is the flexural rigidity:

$$D = \frac{E \cdot t^3}{12(1-\nu^2)} \tag{6-24}$$

where E is the Young modulus of elasticity and ν is Poisson's ratio. In our measurement, the stainless steel diaphragms were used, for which E=200 GPa, ν=0.29, and the yield tensile stress is 215 MPa. By substituting σ_m=215 MPa into (6-22), the maximum pressure difference that the diaphragm with specific radius and thickness can withstand within its elastic deformation can be obtained. For the diaphragms fitted in the three flanges, the radiuses are 11.43, 18.80, and 27.94 mm. Moreover, for each radius, we prepared four types of diaphragms with different thickness: 0.10, 0.15, 0.30, and 0.41 mm.

Then, the diaphragm is subjected to an external force from the lower sample holder, which can be analyzed by the edge clamped circular plate model under center load as shown in Figure 6-8, where F is the external force from the lower sample holder.

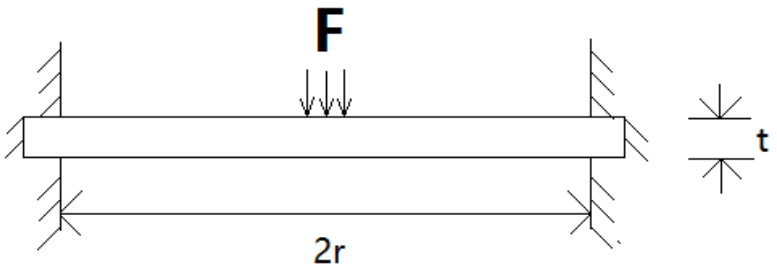

Figure 6-8. Schematic diagram of the edge clamped circular plate under center load.

In this case, the maximum reflection will also occur at the center:

$$y_m = \frac{Fr^2}{16\pi D} \tag{6-25}$$

Thus, from (6-23) and (6-25) we can get the resultant deflection (y) of the diaphragm is:

$$y = \frac{\Delta P r^4}{64D} - \frac{Fr^2}{16\pi D} \tag{6-26}$$

For the holder-sample-holder system, shown in Figure 6-9, where E_s, h_1, and A_1 are the young's modulus of elasticity, height, and force area (cross-sectional area) of the stainless steel holder, respectively; E_c, h_2, and A_2 are those for crystal sample, when ignoring the gravity of the sample and holder, and the depth of the grove of the holder, we can obtain:

$$\begin{aligned} F &= E_s \varepsilon_1 A_1 \\ F &= E_c \varepsilon_2 A_2 \end{aligned} \tag{6-27}$$

and

$$y = 2\varepsilon_1 h_1 + \varepsilon_2 h_2 \tag{6-28}$$

Furthermore, the two deflections in (6-26) and (6-28) should be the same:

$$2\varepsilon_1 h_1 + \varepsilon_2 h_2 = \frac{\Delta P r^4}{64D} - \frac{Fr^2}{16\pi D} \tag{6-29}$$

Accordingly, we can get the linear relationship between the induced force F and the applied pressure difference ΔP:

$$F = \alpha \cdot \Delta P \tag{6-30}$$

where

$$\alpha = \frac{\pi r^4}{\frac{128\pi D h_1}{E_s A_1} + \frac{64\pi D h_2}{E_c A_2} + 4r^2} \tag{6-31}$$

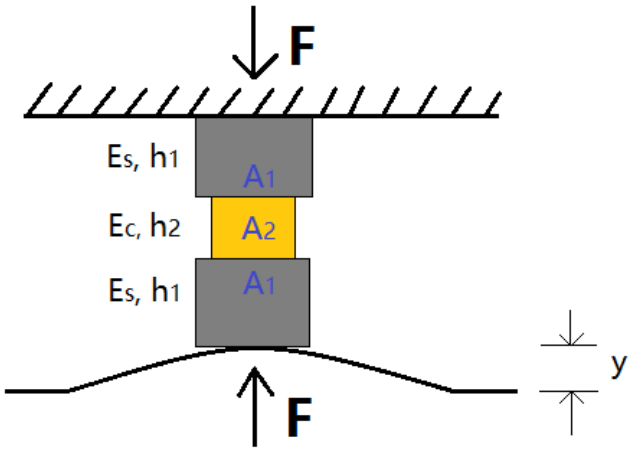

Figure 6-9. Schematic diagram of the holder-sample-holder system under force.

During our measurement, the dimensions of the holders and CTGS Y-cut sample are as follows: h_1=25.39 mm, A_1=5.12×15.82=81.00 mm^2, h_2=11.99 mm, and A_2=2.00×11.99=23.98 mm^2 (YZ plane) or A_2=2.00×11.97=23.94 mm^2 (XY plane).

Next, the second step is to find the relationship between the induced force F and the resulting strain components of the crystal sample. If we only consider the normal stress along the

force direction, it will be F/A_2. And according to the elastic coefficients matrix of CTGS crystals in (2-3), if the force is along X-axis, the resulting nonzero strain components are:

$$S_1 = \frac{F}{A_2} s_{11},\ S_2 = \frac{F}{A_2} s_{12},\ S_3 = \frac{F}{A_2} s_{13},\ S_4 = \frac{F}{A_2} s_{14} \tag{6-32}$$

And if the force is along Z-axis, the nonzero strain components are:

$$S_1 = \frac{F}{A_2} s_{31} = \frac{F}{A_2} s_{13},\ S_2 = \frac{F}{A_2} s_{32} = \frac{F}{A_2} s_{32},\ S_3 = \frac{F}{A_2} s_{33} \tag{6-33}$$

where s_{11}, s_{12}, s_{13}, s_{14}, and s_{33} are the elastic compliance components.

Finally, the third step is to determine the frequency-strain relation, which has been discussed previously and expressed by (6-20) and (6-21).

Therefore, by synthesizing the derivations of the above three steps, we can obtain the relationship between the resonant frequency variation $\frac{\Delta f}{f_0}$ and the pressure difference ΔP:

If the force is along X-axis:

$$\frac{\Delta f}{f_0} = \frac{\alpha}{A_2}\left[s_{11} + \frac{1}{2c_{66}}\left(c_{166} s_{11} + c_{266} s_{12} + c_{366} s_{13} + c_{466} s_{14} \right) \right] \cdot \Delta P \tag{6-34}$$

If the force is along Z-axis:

$$\frac{\Delta f}{f_0} = \frac{\alpha}{A_2}\left[s_{33} + \frac{1}{2c_{66}}\left(c_{166} s_{13} + c_{266} s_{13} + c_{366} s_{33} \right) \right] \cdot \Delta P \tag{6-35}$$

where α was shown in (6-31).

6.3.2.3 High-temperature pressure sensor test

Similar to the temperature sensor in Chapter 4, we can define the sensitivity (S_P) of the pressure sensor as:

$$S_p = \frac{\Delta f}{f_0}\frac{1}{\Delta P} \tag{6-36}$$

Thus, If the force is along X-axis, the sensitivity is:

$$S_P = \frac{\alpha}{A_2}\left[s_{11} + \frac{1}{2c_{66}}\left(c_{166}s_{11} + c_{266}s_{12} + c_{366}s_{13} + c_{466}s_{14}\right)\right] \tag{6-37}$$

and if the force is along Z-axis, the sensitivity will be:

$$S_P = \frac{\alpha}{A_2}\left[s_{33} + \frac{1}{2c_{66}}\left(c_{166}s_{13} + c_{266}s_{13} + c_{366}s_{33}\right)\right] \tag{6-38}$$

According to the previous model, we carried out the high-temperature test for the CTGS Y-cut TSM resonator. The photograph of the entire pressure tubing is shown in Figure 6-10, and the setup of the high-temperature pressure sensor test system is presented in Figure 6-11. We wrapped the flexible heating tape (OMEGA, SWH) around the pipe above the flange to achieve the target of local heating around the sample, which was powered by a benchtop controller (OMEGA, CSi32K). In addition, the benchtop controller monitors the temperature through a flexible thermocouple, the end of which was fixed close to the sample.

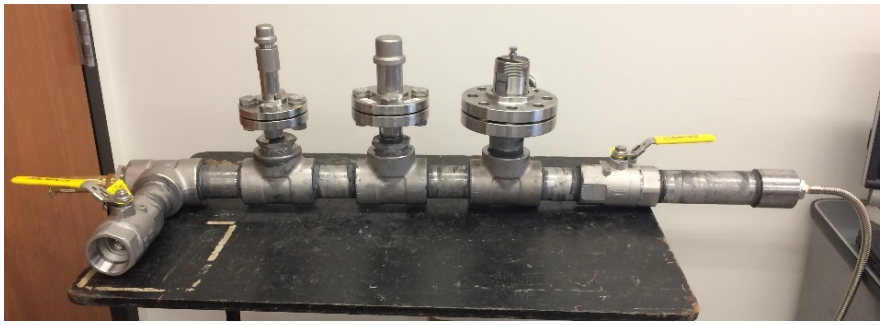

Figure 6-10. Photograph of the stainless steel pressure tubing.

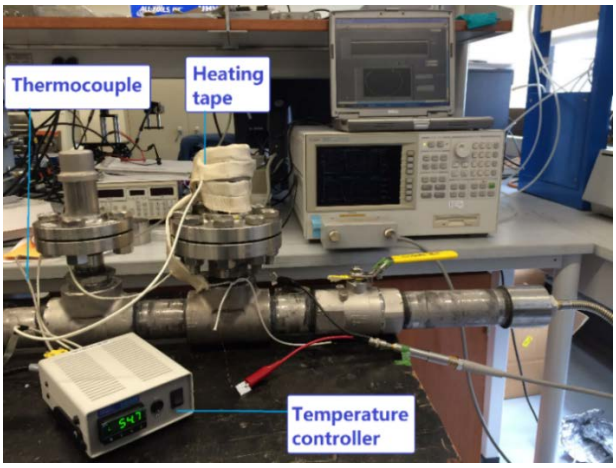

Figure 6-11. Photograph of the high-temperature pressure sensor test system.

In our measurement, we investigated the frequency variations of the sample in the temperature range of 21 to 300°C, and pressure difference range of 0 to 45 PSI (310.26 kPa). The results of force along X-axis and along Z-axis are as follows.

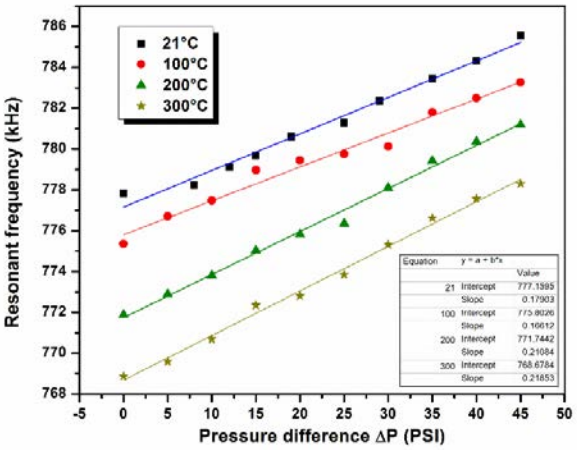

Figure 6-12. Resonant frequency of CTGS Y-cut TSM resonator as a function of the pressure difference at different temperatures when force along X-axis.

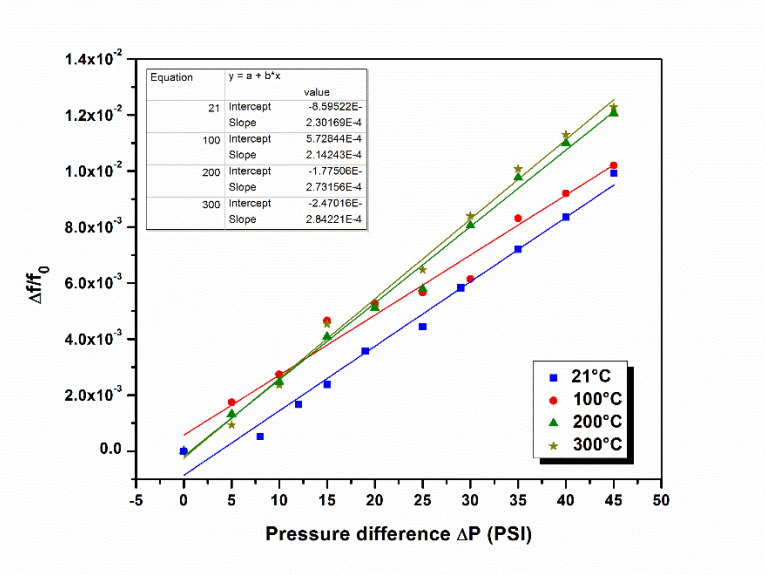

Figure 6-13. Frequency variation of CTGS Y-cut TSM resonator as a function of the pressure difference at different temperatures when force along X-axis.

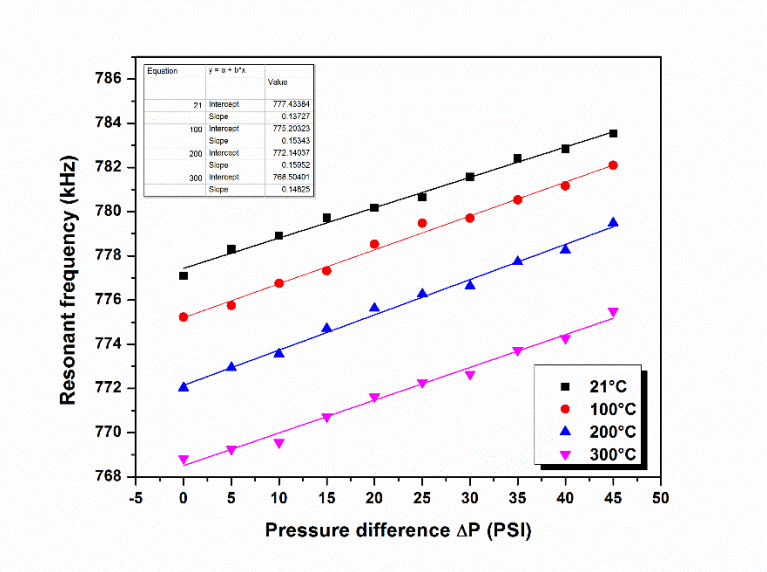

Figure 6-14. Resonant frequency of CTGS Y-cut TSM resonator as a function of the pressure difference at different temperatures when force along Z-axis.

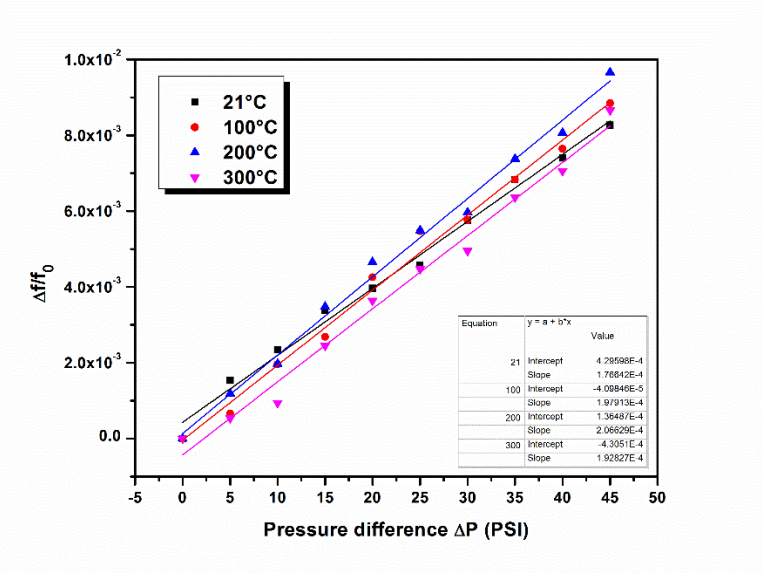

Figure 6-15. Frequency variation of CTGS Y-cut TSM resonator as a function of the pressure difference at different temperatures when force along Z-axis.

Figure 6-12 and Figure 6-13 show respectively the resonant frequency (f_r) and frequency variation ($\frac{\Delta f}{f_0}$) of CTGS Y-cut TSM resonator as a function of the pressure difference (ΔP) at different temperatures (21, 100, 200, and 300°C) when the force is along X-axis. As can be seen, the resonant frequency increases linearly with the rise of the pressure difference and the growth rates are 0.18, 0.17, 0.21, and 0.22 kHz/PSI at 21, 100, 200, and 300°C, respectively. Moreover, the pressure sensitivities at these temperatures are 2.30, 2.14, 2.73, and 2.84 $\times 10^{-4}$ in^2/lbf, respectively.

Figure 6-14 and Figure 6-15 exhibit the relevant information for the case that the force along Z-axis. Similarly, the resonant frequency increases linearly with pressure difference at the rates of 0.14, 0.15, 0.16, and 0.15 kHz/PSI at 21, 100, 200, and 300°C, respectively. And the pressure sensitivities are 1.77, 1.98, 2.07, and 1.93 $\times 10^{-4}$ in^2/lbf, respectively.

By comparing these results, we can draw the following conclusions: 1) The temperature has no direct and obvious influence on the sensitivity of the pressure sensor; 2) The pressure sensor is more sensitive when the force is along X-axis (3.63×10^{-8} m^2/N, averagely) than along the Z-axis (2.81×10^{-8} m^2/N, averagely).

Additionally, once we get the sensitivity, we can obtain some information about the third-order elastic stiffness coefficients (c_{166}, c_{266}, c_{366}, and c_{466}) through (6-37) and (6-38). Although we can't identify each one accurately, we can know the effective coefficients:

$$s_{166}^{*} = s_{11} + \frac{1}{2c_{66}}\left(c_{166}s_{11} + c_{266}s_{12} + c_{366}s_{13} + c_{466}s_{14}\right) \quad \textbf{(6-39)}$$

and

$$s_{366}^{*} = s_{33} + \frac{1}{2c_{66}}\left(c_{166}s_{13} + c_{266}s_{13} + c_{366}s_{33}\right) \quad \textbf{(6-40)}$$

For example, if we use the diaphragm with r=11.43 mm and t=0.41 mm,

when the force is along X-axis, which means $E_c=c_{11}$=142.6 GPa, we can get $\alpha=6.1248\times10^{-4}$ m^2, and further we can obtain $s_{166}^{*}=1.421\times10^{-9}$ $m^2/N=1421$ pm^2/N;

when the force is along Z-axis, which means $E_c=c_{33}$=203.3 GPa, we can get $\alpha=6.1253\times10^{-4}$ m^2 and $s_{366}^{*}=1.098\times10^{-9}$ $m^2/N=1098$ pm^2/N;

6.4 CONCLUSION

In conclusion, the non-linearity effects of CTGS crystals which are related to the high-order (third and fourth) dielectric and elastic coefficients were investigated in this Chapter. We studied the non-linearity effects through applying electric or mechanical fields to the crystal resonator,

because its resonant frequency will change when it is subjected to the applied external fields, which have been demonstrated to be directly associated to the high-order coefficients. And the CTGS Y-cut TSM resonators were selected as the research objects.

Through applying DC bias fields (along Y-axis) to the CTGS Y-cut resonator, we found that its resonant frequency increased linearly with the enhancement of the DC electric fields. In addition, through the DC bias test, we characterized the following fourth order dielectric and elastic coefficients of CTGS crystals: ε_{2222}=-2.16×10^{-25} F·m/V^2, c^D_{6666}=4.29×10^{14} N/m^2, and $h^*_{22,66}$=-6.87×10^{12} m/F.

More significantly, we thoroughly studied the force-frequency effect of the CTGS resonator and designed and processed the high-temperature pressure sensor test system. According to our test system, we established an accurate model and successfully derived the expression of the pressure sensitivity which consisted of the third-order elastic stiffness coefficients (c_{166}, c_{266}, c_{366}, and c_{466}). It was found that the resonant frequency also increased linearly with the pressure difference increasing. And the sensitive of the pressure sensor is higher when the force is along X-axis (3.63×10^{-8} m^2/N, averagely) than along the Z-axis (2.81×10^{-8} m^2/N, averagely). Additionally, we determined two effective third-order elastic coefficients: s^*_{166}=1.421×10^{-9} m^2/N and s^*_{366}=1.098×10^{-9} m^2/N.

7.0 CONCLUSION AND PROSPECT

This dissertation thoroughly investigated two novel and currently most promising high-temperature piezoelectric sensing single crystals: CTGS and YCOB, and implemented in-depth studies of high-temperature temperature sensor, mass sensor, and pressure sensor based on the CTGS Y-cut thickness shear mode resonators which possessed the best overall high-temperature performance.

1) First of all, we characterized all the basic real and complex dielectric, elastic, and piezoelectric constants of these two crystals, as well as their temperature dependence over the temperature range of 21 to 800°C. This work not only let us have a better understanding of these materials, but also, more importantly, demonstrated that they were capable of sensing at 800°C or even higher temperatures and provided us a great deal of data base for future research concerning these two crystals.
2) Furthermore, we designed and experimentally validated the robust and reliable high-temperature temperature senor, mass sensor, and pressure sensor based on CTGS Y-cut TSM resonators:
   A. the temperature sensor was proved to be able to work stably up to 1000°C with excellent linearity;
   B. the mass sensor possessed the inspiring ability to accurately monitor the mass change of micro- and nano-scale polymer layers up to 800°C;

C. the pressure sensor showed the purely linear relationship between the frequency variation of the resonator and the pressure difference in the temperature range of 21 to 300°C, and pressure difference range of 0 to 310.26 kPa (but not limited to these values);

D. the non-linear effects were studied and some higher order dielectric and elastic coefficients were characterized.

Through the study of this work, we have a more comprehensive understanding of these crystals, and, more surprisingly, we see their enormous potential in high-temperature sensing applications. Consequently, there are a lot of relevant research worth more time and effort to pursue. We hereby propose some topics worthy of future study:

a) The theoretical derivation and experimental verification of the optimal crystalline orientations for different types of high-temperature sensors of CTGS and YCOB, like AT-cut of Quartz;
b) The theoretical modeling and practical applications of high-temperature sensors based on YCOB crystals;
c) The research on surface acoustic wave (SAW) sensors based on CTGS and YCOB to broaden the application frequency range and improve the sensitivity;
d) The study on wireless and passive high-temperature sensors to improve the applicability and simplicity;
e) Sensor related interdisciplinary research, e.g. 3-D printable sensor, biosensor, and so on.

BIBLIOGRAPHY

[1] W. G. Cady, *Piezoelectricity*: McGraw-Hill, 1946.

[2] C. Brown, R. Kell, R. Taylor, and L. Thomas, "Piezoelectric materials, a review of progress," *IRE Transactions on component parts,* vol. 9, pp. 193-211, 1962.

[3] R. C. Buchanan, *Ceramic materials for electronics: processing, properties, and applications*: Marcel Dekker, Inc., 1986.

[4] M. Lippmann, "lectricité libre est constante,. Cette loi, que j'appellerai le principe," 1881.

[5] W. Voigt, *Lehrbuch der kristallphysik (mit ausschluss der kristalloptik)*: Springer-Verlag, 2014.

[6] IEEE, "IEEE Standard on Piezoelectricity," ed, 1988.

[7] J. Nuffer and T. Bein, "Applications of piezoelectric materials in transportation industry," in *Global symposium on innovative solutions for the advancement of the transport industry*, 2006.

[8] G. H. Haertling, "Ferroelectric ceramics: history and technology," *Journal of the American Ceramic Society,* vol. 82, pp. 797-818, 1999.

[9] S. Zhang and F. Yu, "Piezoelectric materials for high temperature sensors," *Journal of the American Ceramic Society,* vol. 94, pp. 3153-3170, 2011.

[10] M. J. Schulz, M. J. Sundaresan, J. Mcmichael, D. Clayton, R. Sadler, and B. Nagel, "Piezoelectric materials at elevated temperature," *Journal of Intelligent Material Systems and Structures,* vol. 14, pp. 693-705, 2003.

[11] G. W. Hunter, J. D. Wrbanek, R. S. Okojie, P. G. Neudeck, G. C. Fralick, L. Chen, *et al.*, "Development and application of high-temperature sensors and electronics for propulsion applications," in *Defense and Security Symposium*, 2006, pp. 622209-622209-12.

[12] R. Turner, P. A. Fuierer, R. Newnham, and T. Shrout, "Materials for high temperature acoustic and vibration sensors: A review," *Applied acoustics,* vol. 41, pp. 299-324, 1994.

[13] D. Damjanovic, "Materials for high temperature piezoelectric transducers," *Current Opinion in Solid State and Materials Science,* vol. 3, pp. 469-473, 1998.

[14] J. Tichý, J. r. Erhart, E. Kittinger, and J. Prívratská, *Fundamentals of piezoelectric sensorics: mechanical, dielectric, and thermodynamical properties of piezoelectric materials*: Springer Science & Business Media, 2010.

[15] E. Philippot, A. Ibanez, A. Goiffon, M. Cochez, A. Zarka, B. Capelle, *et al.*, "A quartz-like material: gallium phosphate (GaPO4); crystal growth and characterization," *Journal of crystal growth,* vol. 130, pp. 195-208, 1993.

[16] H. Fritze, "High temperature piezoelectric materials: Defect chemistry and electro-mechanical properties," *Journal of electroceramics,* vol. 17, pp. 625-630, 2006.

[17] H. Fritze, "High-temperature bulk acoustic wave sensors," *Measurement Science and Technology,* vol. 22, p. 012002, 2010.

[18] S. Zhang, Y. Zheng, H. Kong, J. Xin, E. Frantz, and T. R. Shrout, "Characterization of high temperature piezoelectric crystals with an ordered langasite structure," *Journal of Applied Physics,* vol. 105, p. 114107, 2009.

[19] S. B. Lang, *Sourcebook of pyroelectricity* vol. 2: CRC Press, 1974.

[20] R. Newnham and L. E. Cross, "Ferroelectricity: The foundation of a field from form to function," *MRS bulletin,* vol. 30, pp. 845-848, 2005.

[21] R. Kepler, "Piezoelectricity, pyroelectricity, and ferroelectricity in organic materials," *Annual Review of Physical Chemistry,* vol. 29, pp. 497-518, 1978.

[22] R. E. Newnham, *Properties of materials: anisotropy, symmetry, structure*: Oxford University Press on Demand, 2005.

[23] K. C. Kao, *Dielectric phenomena in solids*: Academic press, 2004.

[24] M. R. Stuart, "Dielectric constant of quartz as a function of frequency and temperature," *Journal of Applied Physics,* vol. 26, pp. 1399-1404, 1955.

[25] E. Sun, S. Zhang, J. Luo, T. R. Shrout, and W. Cao, "Elastic, dielectric, and piezoelectric constants of Pb (In 1/2 Nb 1/2) O 3–Pb (Mg 1/3 Nb 2/3) O 3–PbTiO 3 single crystal poled along [011] c," *Applied physics letters,* vol. 97, p. 032902, 2010.

[26] G. Gautschi, "Piezoelectric Sensorics: force, strain, pressure, acceleration and acoustic emission sensors, materials and amplifiers. 2002," ed: Springer, 2002.

[27] E. Havinga, "The temperature dependence of dielectric constants," *Journal of Physics and Chemistry of Solids,* vol. 18, pp. 253-255, 1961.

[28] W. P. Mason, *Piezoelectric Crystals and Their Application to Ultrasonics*. New York, NY, USA: D. VAN NOSTRAND COMPANY, Inc., 1950.

[29] J. Zhao, J. Winey, and Y. Gupta, "First-principles calculations of second-and third-order elastic constants for single crystals of arbitrary symmetry," *Physical Review B,* vol. 75, p. 094105, 2007.

[30] T. Shao, B. Wen, R. Melnik, S. Yao, Y. Kawazoe, and Y. Tian, "Temperature dependent elastic constants for crystals with arbitrary symmetry: Combined first principles and continuum elasticity theory," *Journal of Applied Physics,* vol. 111, p. 083525, 2012.

[31] A. J. Moulson and J. M. Herbert, *Electroceramics: materials, properties, applications*: John Wiley & Sons, 2003.

[32] S.-E. Park and T. R. Shrout, "Characteristics of relaxor-based piezoelectric single crystals for ultrasonic transducers," *IEEE Transactions on Ultrasonics, Ferroelectrics, and Frequency Control,* vol. 44, pp. 1140-1147, 1997.

[33] R. T. Smith and F. S. Welsh, "Temperature Dependence of the Elastic, Piezoelectric, and Dielectric Constants of Lithium Tantalate and Lithium Niobate," *Journal of Applied Physics,* vol. 42, pp. 2219-2230, 1971.

[34] F. Yu, S. Zhang, X. Zhao, D. Yuan, L. Qin, Q. M. Wang, *et al.*, "Dielectric and electromechanical properties of rare earth calcium oxyborate piezoelectric crystals at high temperatures," *IEEE Trans Ultrason Ferroelectr Freq Control,* vol. 58, pp. 868-73, Apr 2011.

[35] W. Mason and H. Jaffe, "Methods for measuring piezoelectric, elastic, and dielectric coefficients of crystals and ceramics," *Proceedings of the IRE,* vol. 42, pp. 921-930, 1954.

[36] W. P. Mason, *Electromechanical transducers and wave filters*: D. Van Nostrand Co., 1948.

[37] M. Redwood and J. Lamb, "On the measurement of attenuation in ultrasonic delay lines," *Proceedings of the IEE-Part B: Radio and Electronic Engineering,* vol. 103, pp. 773-780, 1956.

[38] A. Caronti, R. Carotenuto, and M. Pappalardo, "Electromechanical coupling factor of capacitive micromachined ultrasonic transducers," *The Journal of the Acoustical Society of America,* vol. 113, pp. 279-288, 2003.

[39] N. Lamberti, A. Iula, and M. Pappalardo, "The electromechanical coupling factor in static and dynamic conditions," *Acta Acustica united with Acustica,* vol. 85, pp. 39-46, 1999.

[40] S.-E. Park and T. R. Shrout, "Ultrahigh strain and piezoelectric behavior in relaxor based ferroelectric single crystals," *Journal of Applied Physics,* vol. 82, pp. 1804-1811, 1997.

[41] S. Zhang and T. R. Shrout, "Relaxor-PT single crystals: observations and developments," *IEEE transactions on ultrasonics, ferroelectrics, and frequency control,* vol. 57, 2010.

[42] J. H. Harlow, *Electric power transformer engineering*: CRC press, 2012.

[43] B. Ellis, "Electronic circuits, fundamentals and applications," *Soldering & Surface Mount Technology,* vol. 18, 2006.

[44] C. T.-C. Nguyen, "MEMS technology for timing and frequency control," *IEEE transactions on ultrasonics, ferroelectrics, and frequency control,* vol. 54, 2007.

[45] D. T. Nguyen, C. Baker, W. Hease, S. Sejil, P. Senellart, A. Lemaitre, *et al.*, "Ultrahigh Q-frequency product for optomechanical disk resonators with a mechanical shield," *Applied Physics Letters,* vol. 103, p. 241112, 2013.

[46] L. B. Silva and E. J. Santos, "Modeling quality factor in AT-cut quartz-crystal resonators," in *Microelectronics Technology and Devices (SBMicro), 2013 Symposium on*, 2013, pp. 1-4.

[47] J. Soejima and K. Nagata, "PbNb2O6 ceramics with tungsten bronze structure for low Qm piezoelectric material," *Japanese Journal of Applied Physics,* vol. 40, p. 5747, 2001.

[48] R. Holland and E. P. EerNisse, "Accurate measurement of coefficients in a ferroelectric ceramic," *IEEE Transactions on Sonics and Ultrasonics,* vol. 16, pp. 173-181, 1969.

[49] X.-H. Du, Q.-M. Wang, and K. Uchino, "Accurate Determination of Complex Materials Coefficients of Piezoelectric Resonators," *IEEE Trans Ultrason Ferroelectr Freq Control,* vol. 50, pp. 312-320, 2003.

[50] X.-H. Du, Q.-M. Wang, and K. Uchino, "An Accurate Method for the Determination of Complex Coefficients of Single Crystal Piezoelectric Resonators I: Theory," *IEEE Trans Ultrason Ferroelectr Freq Control,* vol. 51, pp. 227-237, 2004.

[51] H. Le Chatelier, "Sur la dilatation du quartz," *Comptes Rendus,* vol. 108, p. 1046, 1889.

[52] R. K. Cook and P. G. Weissler, "Piezoelectric constants of alpha-and beta-quartz at various temperatures," *Physical Review,* vol. 80, p. 712, 1950.

[53] A. Walker, "Hydrothermal synthesis of quartz crystals," *Journal of the American Ceramic Society,* vol. 36, pp. 250-256, 1953.

[54] J. F. Bertone, J. Cizeron, R. K. Wahi, J. K. Bosworth, and V. L. Colvin, "Hydrothermal synthesis of quartz nanocrystals," *Nano Letters,* vol. 3, pp. 655-659, 2003.

[55] R. Bechmann, "Elastic and piezoelectric constants of alpha-quartz," *Physical review,* vol. 110, p. 1060, 1958.

[56] A. J. Mullen, "Temperature variation of the piezoelectric constant of quartz," *Journal of Applied Physics,* vol. 40, pp. 1693-1696, 1969.

[57] A. De and K. Rao, "Dielectric properties of synthetic quartz crystals," *Journal of materials science,* vol. 23, pp. 661-664, 1988.

[58] H. Tiersten, "The Redetermination of the Elastic, Piezoelectric and Dielectric Constants of Quartz and Their Variation with Temperature," DTIC Document1989.

[59] P. Heyliger, H. Ledbetter, and S. Kim, "Elastic constants of natural quartz," *The Journal of the Acoustical Society of America,* vol. 114, pp. 644-650, 2003.

[60] C. Lam, C. Y. Wang, and S. Wang, "A review of the recent development of temperature stable cuts of quartz for SAW applications," in *Proceedings of the Fourth International Symposium on Acoustic Wave Devices for Future Mobile Communication Systems, Chiba, Japan*, 2010, pp. 3-5.

[61] F. C. Hawthorne and D. J. Henry, "Classification of the minerals of the tourmaline group," *EUROPEAN JOURNAL OF MINERALOGY-STUTTGART-*, vol. 11, pp. 201-216, 1999.

[62] D. J. Henry, M. Novák, F. C. Hawthorne, A. Ertl, B. L. Dutrow, P. Uher, *et al.*, "Nomenclature of the tourmaline-supergroup minerals," *American Mineralogist,* vol. 96, pp. 895-913, 2011.

[63] F. C. Hawthorne and D. M. Dirlam, "Tourmaline the indicator mineral: From atomic arrangement to Viking navigation," *Elements,* vol. 7, pp. 307-312, 2011.

[64] C. Frondel and R. Collette, "Synthesis of tourmaline by reaction of mineral grains with NaCl-H3BO3 solution, and its implications in rock metamorphism," *American Mineralogist,* vol. 42, pp. 754-758, 1957.

[65] T. Setkova, Y. Shapovalov, and V. Balitsky, "Growth of tourmaline single crystals containing transition metal elements in hydrothermal solutions," *Journal of Crystal Growth,* vol. 318, pp. 904-907, 2011.

[66] T. V. Setkova and V. S. Balitskiy, "Epitaxial growth of Ga-rich tourmaline on natural elbaite seed in boric hydrothermal solutions," in *Proc. 17th Int. Conf. Cryst. Growth Epitaxy (ICCGE'17)*, 2013, pp. 1-4.

[67] C. Shekhar Pandey, S. Jodlauk, and J. Schreuer, "Correlation between dielectric properties and chemical composition of the tourmaline single crystals," *Applied Physics Letters,* vol. 99, p. 142906, 2011.

[68] C. Shekhar Pandey and J. Schreuer, "Elastic and piezoelectric constants of tourmaline single crystals at non-ambient temperatures determined by resonant ultrasound spectroscopy," *Journal of Applied Physics,* vol. 111, p. 013516, 2012.

[69] K. D. Hawkins, I. D. Mackinnon, and H. Schneeberger, "Influence of chemistry on the pyroelectric effect in tourmaline," *American Mineralogist,* vol. 80, pp. 491-501, 1995.

[70] T. Volk and M. Wöhlecke, *Lithium niobate: defects, photorefraction and ferroelectric switching* vol. 115: Springer Science & Business Media, 2008.

[71] K. Nassau, H. Levinstein, and G. Loiacono, "Ferroelectric lithium niobate. 1. Growth, domain structure, dislocations and etching," *Journal of Physics and Chemistry of Solids,* vol. 27, pp. 983-988, 1966.

[72] V. Kurlov and B. Red'kin, "Growth of shaped lithium tantalate crystals," *Journal of Crystal Growth,* vol. 104, pp. 80-83, 1990.

[73] T. Shiosaki, M. Adachi, and A. Kawabata, "Growth and properties of piezoelectric lithium tetraborate crystal for BAW and SAW devices," in *Applications of Ferroelectrics. 1986 Sixth IEEE International Symposium on,* 1986, pp. 455-464.

[74] K. Uchino, *Advanced piezoelectric materials: Science and technology*: Elsevier, 2010.

[75] S.-J. Fan, "Properties, production and application of new piezoelectric crystal lithium tetraborate Li/sub 2/B/sub 4/O/sub 7," in *Frequency Control Symposium, 1993. 47th., Proceedings of the 1993 IEEE International,* 1993, pp. 353-358.

[76] A. Weidenfelder, J. Shi, P. Fielitz, G. Borchardt, K. Becker, and H. Fritze, "Electrical and electromechanical properties of stoichiometric lithium niobate at high-temperatures," *Solid State Ionics,* vol. 225, pp. 26-29, 2012.

[77] E. Philippot, D. Palmier, M. Pintard, and A. Goiffon, "A general survey of quartz and quartz-like materials: packing distortions, temperature, and pressure effects," *Journal of Solid State Chemistry,* vol. 123, pp. 1-13, 1996.

[78] J. H. Sherman, "Quartz analogues," in *40th Annual Symposium on Frequency Control. 1986,* 1986, pp. 91-95.

[79] E. Philippot, A. Goiffon, A. Ibanez, and M. Pintard, "Structure deformations and existence of the α-β transition in MXO4 quartz-like materials," *Journal of Solid State Chemistry,* vol. 110, pp. 356-362, 1994.

[80] C. Glidewell, "Some chemical and structural consequences of non-bonded interactions," *Inorganica Chimica Acta,* vol. 12, pp. 219-227, 1975.

[81] H. Grimm and B. Dorner, "On the mechanism of the α-β phase transformation of quartz," *Journal of Physics and Chemistry of Solids,* vol. 36, pp. 407-413, 1975.

[82] O. Cambon, P. Yot, D. Balitsky, A. Goiffon, E. Philippot, B. Capelle, *et al.*, "Crystal growth of GaPO4, a very promising material for manufacturing BAW devices," in *Annales de Chimie Science des Matériaux,* 2001, pp. 79-84.

[83] G. Xu, H. Cui, J. Li, and J. Wang, "Investigation of single crystal growth of GaPO by the flux method," *Crystallography Reports,* vol. 58, 2013.

[84] P. Worsch, "GaPO4 crystals for sensor applications, sensors 2002," *Proceedings of IEEE,* vol. 1, pp. 12-14, 2002.

[85] J. Haines, O. Cambon, N. Prudhomme, G. Fraysse, D. Keen, L. Chapon, *et al.,* "High-temperature, structural disorder, phase transitions, and piezoelectric properties of Ga P O 4," *Physical Review B,* vol. 73, p. 014103, 2006.

[86] F. Krispel, C. Reiter, J. Neubig, F. Lenzenhuber, P. Krempl, W. Wallnofer, *et al.,* "Properties and applications of singly rotated GaPO/sub 4/resonators," in *Frequency Control Symposium and PDA Exhibition Jointly with the 17th European Frequency and Time Forum, 2003. Proceedings of the 2003 IEEE International*, 2003, pp. 668-673.

[87] C. Reiter, P. W. Krempl, H. Thanner, W. Wallnöfer, and P. M. Worsch, "Material properties of GaPO4 and their relevance for applications," in *Annales de chimie science des matériaux,* 2001, pp. 91-94.

[88] B. Mill, A. Butashin, A. Ellern, and A. Maier, "Formation de phases dans le system CaO–Ga 2 O 3–GeO 2," *Izvest. Akad. Nauk Sssr Neorg. Mater.,* vol. 17, pp. 1648-1653, 1981.

[89] B. Mill, "Formation of phases with the Ca 3 Ga 2 Ge 4 O 14 structure in the AO-TeO 3-Ga 2 O 3-XO 2 (A= Pb, Ba, Sr; X= Si, Ge) and PbO-TeO 3-MO-GeO 2 (M= Zn, Co) systems," *Russian Journal of Inorganic Chemistry,* vol. 55, pp. 1611-1616, 2010.

[90] A. Dudka and V. Simonov, "Structural conditionality of the piezoelectric properties of langasite family crystals," *Crystallography Reports,* vol. 56, pp. 980-985, 2011.

[91] I. Andreev, "Single crystals of the langasite family: An intriguing combination of properties promising for acoustoelectronics," *Technical physics,* vol. 51, pp. 758-764, 2006.

[92] B. V. Mill and Y. V. Pisarevsky, "Langasite-type materials: from discovery to present state," in *Frequency Control Symposium and Exhibition, 2000. Proceedings of the 2000 IEEE/EIA International*, 2000, pp. 133-144.

[93] H. Takeda, J.-i. Yamaura, T. Hoshina, and T. Tsusrumi, "Growth, structure and electrical properties of aluminum substituted langasite family crystals," in *IOP Conference Series: Materials Science and Engineering*, 2011, p. 092020.

[94] H. Yoshida, O. Eguchi, Y. Ohashi, and J. Kushibiki, "Applications of langasite family crystals to piezoelectric devices," in *Proc. Symp. Ultrason. Electron*, 2012, pp. 347-348.

[95] T. Fukuda, P. Takeda, K. Shimamura, H. Kawanaka, M. Kumatoriya, S. Murakami, *et al.,* "Growth of new langasite single crystals for piezoelectric applications," in *Applications of Ferroelectrics, 1998. ISAF 98. Proceedings of the Eleventh IEEE International Symposium on*, 1998, pp. 315-319.

[96] S. Georgescu, A. Voiculescu, C. Matei, O. Toma, L. Gheorghe, and A. Achim, "Reflectance measurements on Europium-doped Langasite, Langanite and Langatate powders," *Romanian Reports in Physics,* vol. 62, pp. 128-133, 2010.

[97] F. Yu, X. Zhao, L. Pan, F. Li, D. Yuan, and S. Zhang, "Investigation of zero temperature compensated cuts in langasite-type piezocrystals for high temperature applications," *Journal of Physics D: Applied Physics,* vol. 43, p. 165402, 2010.

[98] B. Chai, H. Qiu, Y. Ji, and J. Lefaucheur, "Growth of high quality single domain crystals of langasite family compounds," in *Frequency and Time Forum, 1999 and the IEEE International Frequency Control Symposium, 1999., Proceedings of the 1999 Joint Meeting of the European,* 1999, pp. 821-828.

[99] M. Adachi, Y. Sawada, T. Funakawa, and T. Karaki, "Growth of langasite family compounds for bulk and saw applications," *Ferroelectrics,* vol. 273, pp. 89-94, 2002.

[100] A. Wu, "Bridgman growth of langasite‐type piezoelectric crystals," *Crystal Research and Technology,* vol. 42, pp. 862-866, 2007.

[101] M. Adachi, T. Funakawa, and T. Karaki, "Growth of substituted langasite-type Ca 3 NbGa 3 Si 2 O 14 single crystals, and their dielectric, elastic and piezoelectric properties," *Ferroelectrics,* vol. 286, pp. 43-48, 2003.

[102] T. Kuze, H. Takeda, T. Nishida, K. Uchiyama, and T. Shiosaki, "Synthesis and Electric Properties of Alminum Substituted Langasite-type La 3 Nb 0.5 Ga 5.5 O 14 Single Crystals," in *Applications of Ferroelectrics, 2007. ISAF 2007. Sixteenth IEEE International Symposium on,* 2007, pp. 594-595.

[103] M. Kumatoriya, H. Sato, J. Nakanishi, T. Fujii, M. Kadota, and Y. Sakabe, "Crystal growth and electromechanical properties of Al substituted langasite (La 3 Ga 5− x Al x SiO 14)," *Journal of crystal growth,* vol. 229, pp. 289-293, 2001.

[104] B. Chai, A. Bustamante, and M. Chou, "A new class of ordered langasite structure compounds," in *Frequency Control Symposium and Exhibition, 2000. Proceedings of the 2000 IEEE/EIA International,* 2000, pp. 163-168.

[105] H. Zu, H. Wu, Y. Wang, S. Zhang, T. R. Shrout, and Q.-M. Wang, "Properties of single crystal piezoelectric Ca 3 TaGa 3 Si 2 O 14 and YCa 4 O (BO 3) 3 resonators at high-temperature and vacuum conditions," *Sensors and Actuators A: Physical,* vol. 216, pp. 167-175, 2014.

[106] Z. Wang, D. Yuan, Z. Cheng, X. Duan, H. Sun, X. Shi, *et al.,* "Growth of a new ordered langasite structure compound Ca 3 TaGa 3 Si 2 O 14 single crystal," *Journal of crystal growth,* vol. 253, pp. 398-403, 2003.

[107] H. Ohsato, T. Iwatak, and H. Morikoshi, "Mechanism of piezoelectricity for langasite based on the framework crystal structure," *Transactions on Electrical and Electronic Materials,* vol. 13, pp. 51-59, 2012.

[108] E. Domoroshchina, "Growth and neutron diffraction investigation of Ca 3 NbGa 3 Si 2 O 14 and La 3 Ga 5.5 Nb 0.5 O 14 crystals," *Journal of Materials*, vol. 2013, 2013.

[109] J. Xin, Y. Zheng, H. Kong, H. Chen, X. Tu, and E. Shi, "Growth of a new ordered langasite structure crystal Ca3TaAl3Si2O14," *Crystal Growth and Design*, vol. 8, pp. 2617-2619, 2008.

[110] R. Norrestam, M. Nygren, and J.-O. Bovin, "Structural investigations of new calcium-rare earth (R) oxyborates with the composition $Ca_4RO(BO_3)_3$," *Chemistry of Materials*, vol. 4, pp. 737-743, 1992.

[111] F. Yu, S. Zhang, X. Zhao, S. Guo, X. Duan, and D. Yuan, "Investigation of the dielectric and piezoelectric properties of $ReCa_4O(BO_3)_3$ crystals," *Journal of Physics D: Applied Physics*, vol. 44, p. 135405(6pp), 2011.

[112] Y. Fei, B. H. Chai, C. Ebbers, Z. Liao, K. I. Schaffers, and P. Thelin, "Large-aperture YCOB crystal growth for frequency conversion in the high average power laser system," *Journal of crystal growth*, vol. 290, pp. 301-306, 2006.

[113] R. Arun Kumar, "Borate crystals for nonlinear optical and laser applications: a review," *Journal of Chemistry*, vol. 2013, 2012.

[114] M. Iwai, T. Kobayashi, H. Furuya, Y. Mori, and T. Sasaki, "Crystal Growth and Optical Characterization of Rare-Earth (Re) Calcium Oxyborate ReCa 4O (BO 3) 3 (Re= Y or Gd) as New Nonlinear Optical Material," *Japanese journal of applied physics*, vol. 36, p. L276, 1997.

[115] Y. Zheng, X. Tu, J. Chen, P. Gao, and E. Shi, "Piezoelectric acceleration sensors based on LGX and ReCOB crystals for application above 645ºC," in *European Frequency and Time Forum & International Frequency Control Symposium (EFTF/IFC), 2013 Joint*, 2013, pp. 977-979.

[116] C. Chen, T. Sasaki, R. Li, Y. Wu, Z. Lin, Y. Mori, *et al.*, *Nonlinear optical borate crystals: Principals and applications*: John Wiley & Sons, 2012.

[117] S. Zhang, F. Yu, R. Xia, Y. Fei, E. Frantz, X. Zhao, *et al.*, "High temperature ReCOB piezocrystals: Recent developments," *Journal of Crystal Growth*, vol. 318, pp. 884-889, 2011.

[118] S. Zhang, E. Frantz, R. Xia, W. Everson, J. Randi, D. W. Snyder, *et al.*, "Gadolinium calcium oxyborate piezoelectric single crystals for ultrahigh temperature (>1000 °C) applications," *Journal of Applied Physics*, vol. 104, p. 084103, 2008.

[119] S. Zhang, Y. Fei, E. Frantz, D. W. Snyder, B. H. Chai, and T. R. Shrout, "High-temperature piezoelectric single crystal ReCa(4)O(BO(3))(3) for sensor applications," *IEEE Trans Ultrason Ferroelectr Freq Control*, vol. 55, pp. 2703-8, Dec 2008.

[120] F. Yu, S. Hou, X. Zhao, and S. Zhang, "High-temperature piezoelectric crystals ReCa4O(BO3)3: a review," *IEEE Trans Ultrason Ferroelectr Freq Control,* vol. 61, pp. 1344-56, Aug 2014.

[121] A. V. Virkar, T. B. Jackson, and R. A. Cutler, "Thermodynamic and kinetic effects of oxygen removal on the thermal conductivity of aluminum nitride," *Journal of the American ceramic society,* vol. 72, pp. 2031-2042, 1989.

[122] Y. Kurokawa, K. Utsumi, and H. Takamizawa, "Development and Microstructural Characterization of High - Thermal - Conductivity Aluminum Nitride Ceramics," *Journal of the American Ceramic Society,* vol. 71, pp. 588-594, 1988.

[123] G. A. Slack, R. A. Tanzilli, R. Pohl, and J. Vandersande, "The intrinsic thermal conductivity of AIN," *Journal of Physics and Chemistry of Solids,* vol. 48, pp. 641-647, 1987.

[124] T. Aubert, O. Elmazria, B. Assouar, E. Blampain, A. Hamdan, D. Genève, *et al.*, "Investigations on AlN/sapphire piezoelectric bilayer structure for high-temperature SAW applications," *IEEE transactions on ultrasonics, ferroelectrics, and frequency control,* vol. 59, pp. 999-1005, 2012.

[125] L. I. Berger, *Semiconductor materials*: CRC press, 1996.

[126] R. Schlesser, R. Dalmau, and Z. Sitar, "Seeded growth of AlN bulk single crystals by sublimation," *Journal of Crystal Growth,* vol. 241, pp. 416-420, 2002.

[127] D. Zhuang, Z. Herro, R. Schlesser, and Z. Sitar, "Seeded growth of AlN single crystals by physical vapor transport," *Journal of crystal growth,* vol. 287, pp. 372-375, 2006.

[128] I. SATOH, S. ARAKAWA, K. TANIZAKI, M. MIYANAGA, T. SAKURADA, Y. YAMAMOTO, *et al.*, "Development of aluminum nitride single-crystal substrates," *SEI Tech. Rev.,* vol. 79, pp. 78-82, 2010.

[129] M.-A. Dubois and P. Muralt, "Properties of aluminum nitride thin films for piezoelectric transducers and microwave filter applications," *Applied Physics Letters,* vol. 74, pp. 3032-3034, 1999.

[130] Z.-W. Yin, H.-S. Luo, P.-C. Wang, and G.-S. Xu, "Growth, characterization and properties of relaxor ferroelectric PMN-PT single crystals," *Ferroelectrics,* vol. 229, pp. 207-216, 1999.

[131] T. R. Shrout, Z. P. Chang, N. Kim, and S. Markgraf, "Dielectric behavior of single crystals near the (1− X) Pb (Mg1/3Nb2/3) O3-(x) PbTiO3 morphotropic phase boundary," *Ferroelectrics Letters Section,* vol. 12, pp. 63-69, 1990.

[132] H. Luo, G. Xu, P. Wang, and Z. Yin, "Growth and characterization of relaxor ferroelectric PMNT single crystals," *Ferroelectrics,* vol. 231, pp. 97-102, 1999.

[133] X. Jiang, K. Kim, S. Zhang, J. Johnson, and G. Salazar, "High-temperature piezoelectric sensing," *Sensors*, vol. 14, pp. 144-169, 2013.

[134] L. Rayleigh, "On waves propagated along the plane surface of an elastic solid," *Proceedings of the London Mathematical Society*, vol. 1, pp. 4-11, 1885.

[135] R. White and F. Voltmer, "Direct piezoelectric coupling to surface elastic waves," *Applied physics letters*, vol. 7, pp. 314-316, 1965.

[136] M. Hoummady, A. Campitelli, and W. Wlodarski, "Acoustic wave sensors: design, sensing mechanisms and applications," *Smart materials and structures*, vol. 6, p. 647, 1997.

[137] M. F. Hribšek, D. V. Tošić, and M. R. Radosavljević, "Surface acoustic wave sensors in mechanical engineering," *FME transactions*, vol. 38, pp. 11-18, 2010.

[138] E. Benes, M. Groschl, F. Seifert, and A. Pohl, "Comparison between BAW and SAW sensor principles," *IEEE transactions on ultrasonics, ferroelectrics, and frequency control*, vol. 45, pp. 1314-1330, 1998.

[139] E. Benes, M. Gröschl, W. Burger, and M. Schmid, "Sensors based on piezoelectric resonators," *Sensors and Actuators A: Physical*, vol. 48, pp. 1-21, 1995.

[140] M. Zakaria, U. Hashim, and M. M. Amin, "Design and fabrication of IDT saw by using conventional lithography technique," *Middle-East Journal of Scientific Research*, vol. 18, pp. 1281-1285, 2013.

[141] A. Pohl, "A review of wireless SAW sensors," *IEEE transactions on ultrasonics, ferroelectrics, and frequency control*, vol. 47, pp. 317-332, 2000.

[142] J. Hornsteiner, E. Born, G. Fischerauer, and E. Riha, "Surface acoustic wave sensors for high-temperature applications," in *Frequency Control Symposium, 1998. Proceedings of the 1998 IEEE International*, 1998, pp. 615-620.

[143] W.-E. Bulst, G. Fischerauer, and L. Reindl, "State of the art in wireless sensing with surface acoustic waves," *IEEE Transactions on Industrial Electronics*, vol. 48, pp. 265-271, 2001.

[144] R. Hauser, L. Reindl, and J. Biniasch, "High-temperature stability of LiNbO/sub 3/based SAW devices," in *Ultrasonics, 2003 IEEE Symposium on*, 2003, pp. 192-195.

[145] M. N. Hamidon, V. Skarda, N. White, F. Krispel, P. Krempl, M. Binhack, *et al.*, "Fabrication of high temperature surface acoustic wave devices for sensor applications," *Sensors and Actuators A: Physical*, vol. 123, pp. 403-407, 2005.

[146] M. N. Hamidon, V. Skarda, N. M. White, F. Krispel, P. Krempl, M. Binhack, *et al.*, "High-temperature 434 MHz surface acoustic wave devices based on GaPO/sub 4," *IEEE*

transactions on ultrasonics, ferroelectrics, and frequency control, vol. 53, pp. 2465-2470, 2006.

[147] M. P. Da Cunha, R. Lad, T. Moonlight, G. Bernhardt, and D. Frankel, "High temperature stability of langasite surface acoustic wave devices," in *Ultrasonics Symposium, 2008. IUS 2008. IEEE*, 2008, pp. 205-208.

[148] J. Thiele and M. P. Da Cunha, "High temperature LGS SAW gas sensor," *Sensors and Actuators B: Chemical*, vol. 113, pp. 816-822, 2006.

[149] B. Drafts, "Acoustic wave technology sensors," *IEEE Transactions on Microwave Theory and Techniques*, vol. 49, pp. 795-802, 2001.

[150] P. Hauptmann, R. Lucklum, and J. Schroder, "Recent trends in bulk acoustic wave resonator sensors," in *Ultrasonics, 2003 IEEE Symposium on*, 2003, pp. 56-65.

[151] K. MARX, "AA useful tool for studying thin polymer films and complex biomolecular systems at the solution-surface interface," *Biomacromolecules*, vol. 4, pp. 1-009, 2003.

[152] R. Lucklum and P. Hauptmann, "The quartz crystal microbalance: mass sensitivity, viscoelasticity and acoustic amplification," *Sensors and Actuators B: Chemical*, vol. 70, pp. 30-36, 2000.

[153] E. Uttenthaler, M. Schräml, J. Mandel, and S. Drost, "Ultrasensitive quartz crystal microbalance sensors for detection of M13-Phages in liquids," *Biosensors and Bioelectronics*, vol. 16, pp. 735-743, 2001.

[154] M.-A. Dubois and C. Muller, "Thin-Film Bulk Acoustic Wave Resonators," in *MEMS-based Circuits and Systems for Wireless Communication*, ed: Springer, 2013, pp. 3-28.

[155] G. Sauerbrey, "Verwendung von Schwingquarzen zur Wägung dünner Schichten und zur Mikrowägung," *Zeitschrift für Physik A Hadrons and Nuclei*, vol. 155, pp. 206-222, 1959.

[156] H. Seh, T. Hyodo, and H. L. Tuller, "Bulk acoustic wave resonator as a sensing platform for NO x at high temperatures," *Sensors and Actuators B: Chemical*, vol. 108, pp. 547-552, 2005.

[157] H. Thanner, P. Krempl, R. Selic, W. Wallnöfer, and P. Worsch, "GaPO4 high temperature crystal microbalance demonstration up to 720 C," *Journal of thermal analysis and calorimetry*, vol. 71, pp. 53-59, 2003.

[158] H. Seh, H. L. Tuller, and H. Fritze, "Langasite for high-temperature acoustic wave gas sensors," *Sensors and Actuators B: Chemical*, vol. 93, pp. 169-174, 2003.

[159] H. Seh, H. L. Tuller, and H. Fritze, "Defect properties of langasite and effects on BAW gas sensor performance at high temperatures," *Journal of the European Ceramic Society*, vol. 24, pp. 1425-1429, 2004.

[160] C. Dejous, I. Esteban, D. Rebiere, J. Pistre, and R. Planade, "Temperature-compensated SH-APM sensors: New theoretical and experimental results," in *Frequency Control Symposium, 1997., Proceedings of the 1997 IEEE International*, 1997, pp. 163-168.

[161] C. Déjous, M. Savart, D. Rebière, and J. Pistré, "A shear-horizontal acoustic plate mode (SH-APM) sensor for biological media," *Sensors and Actuators B: Chemical*, vol. 27, pp. 452-456, 1995.

[162] R. Karabalin, M. Matheny, X. Feng, E. Defaÿ, G. Le Rhun, C. Marcoux, *et al.*, "Piezoelectric nanoelectromechanical resonators based on aluminum nitride thin films," *Applied Physics Letters*, vol. 95, p. 103111, 2009.

[163] T. Y. Lee and J. T. Song, "Detection of carcinoembryonic antigen using AlN FBAR," *Thin Solid Films*, vol. 518, pp. 6630-6633, 2010.

[164] C.-M. Yang, K. Uehara, S.-K. Kim, S. Kameda, H. Nakase, and K. Tsubouchi, "Highly c-axis-oriented AlN film using MOCVD for 5GHz-band FBAR filter," in *Ultrasonics, 2003 IEEE Symposium on*, 2003, pp. 170-173.

[165] Z. Yan, X. Zhou, G. Pang, T. Zhang, W. Liu, J. Cheng, *et al.*, "ZnO-based film bulk acoustic resonator for high sensitivity biosensor applications," *Applied physics letters*, vol. 90, p. 143503, 2007.

[166] Q.-X. Su, P. Kirby, E. Komuro, M. Imura, Q. Zhang, and R. Whatmore, "Thin-film bulk acoustic resonators and filters using ZnO and lead-zirconium-titanate thin films," *IEEE Transactions on Microwave Theory and Techniques*, vol. 49, pp. 769-778, 2001.

[167] W. Xu, X. Zhang, S. Choi, and J. Chae, "A high-quality-factor film bulk acoustic resonator in liquid for biosensing applications," *Journal of Microelectromechanical Systems*, vol. 20, pp. 213-220, 2011.

[168] Y. Osugi, T. Yoshino, K. Suzuki, and T. Hirai, "Single crystal FBAR with LiNbO3 and LiTaO3 piezoelectric substance layers," in *Microwave Symposium, 2007. IEEE/MTT-S International*, 2007, pp. 873-876.

[169] O. Boubai, "Knock detection in automobile engines," *IEEE instrumentation & measurement magazine*, vol. 3, pp. 24-28, 2000.

[170] S. Szwaja, K. Bhandary, and J. Naber, "Comparisons of hydrogen and gasoline combustion knock in a spark ignition engine," *International Journal of Hydrogen Energy*, vol. 32, pp. 5076-5087, 2007.

[171] W. Tian, S. Wu, Z. Zhou, S. Qu, Y. Bai, and J. Luo, "High resolution space quartz-flexure accelerometer based on capacitive sensing and electrostatic control technology," *Review of Scientific Instruments*, vol. 83, p. 095002, 2012.

[172] S. Zhang, X. Jiang, M. Lapsley, P. Moses, and T. R. Shrout, "Piezoelectric accelerometers for ultrahigh temperature application," *Applied Physics Letters,* vol. 96, p. 013506, 2010.

[173] L. Zhou, J. Sun, X. Zheng, S. Deng, J. Zhao, S. Peng, *et al.*, "A model for the energy harvesting performance of shear mode piezoelectric cantilever," *Sensors and Actuators A: Physical,* vol. 179, pp. 185-192, 2012.

[174] G. Tang, J.-Q. Liu, B. Yang, J.-B. Luo, H.-S. Liu, Y.-G. Li, *et al.*, "Piezoelectric MEMS low-level vibration energy harvester with PMN-PT single crystal cantilever," *Electronics letters,* vol. 48, pp. 784-786, 2012.

[175] C. Xu, B. Ren, W. Di, Z. Liang, J. Jiao, L. Li, *et al.*, "Cantilever driving low frequency piezoelectric energy harvester using single crystal material 0.71 Pb (Mg1/3Nb2/3) O3-0.29 PbTiO3," *Applied Physics Letters,* vol. 101, p. 033502, 2012.

[176] S. Hur, S. Lee, and H. Choi, "Fabrication and characterization of PMN-PT single crystal cantilever array for cochlear-like acoustic sensor," *Journal of mechanical science and technology,* vol. 24, pp. 181-184, 2010.

[177] O. Bilgen, M. A. Karami, D. J. Inman, and M. I. Friswell, "The actuation characterization of cantilevered unimorph beams with single crystalpiezoelectric materials," *Smart Materials and Structures,* vol. 20, p. 055024, 2011.

[178] J. Zhang, Z. Wu, Y. Jia, J. Kan, and G. Cheng, "Piezoelectric bimorph cantilever for vibration-producing-hydrogen," *Sensors,* vol. 13, pp. 367-374, 2012.

[179] V. Giurgiutiu and A. Cuc, "Embedded non-destructive evaluation for structural health monitoring, damage detection, and failure prevention," *Shock and Vibration Digest,* vol. 37, p. 83, 2005.

[180] K. Kirk, C. Scheit, and N. Schmarje, "High-temperature acoustic emission tests using lithium niobate piezocomposite transducers," *Insight-Non-Destructive Testing and Condition Monitoring,* vol. 49, pp. 142-145, 2007.

[181] J. A. Johnson, K. Kim, S. Zhang, D. Wu, and X. Jiang, "High-temperature (> 1000° C) acoustic emission sensor," in *SPIE Smart Structures and Materials+ Nondestructive Evaluation and Health Monitoring*, 2013, pp. 869428-869428-12.

[182] J. A. Johnson, K. Kim, S. Zhang, and X. Jiang, "Crack propagation testing using a YCOB acoustic emission sensor," 2014, pp. 906307-906307-8.

[183] M. R. Werner and W. R. Fahrner, "Review on materials, microsensors, systems and devices for high-temperature and harsh-environment applications," *IEEE Transactions on Industrial Electronics,* vol. 48, pp. 249-257, 2001.

[184] J. Xu, G. Pickrell, X. Wang, W. Peng, K. Cooper, and A. Wang, "A novel temperature-insensitive optical fiber pressure sensor for harsh environments," *IEEE Photonics Technology Letters,* vol. 17, pp. 870-872, 2005.

[185] M. Mehregany and C. A. Zorman, "SiC MEMS: opportunities and challenges for applications in harsh environments," *Thin Solid Films,* vol. 355-356, pp. 518-524, 1999.

[186] N. F. Szabo, H. Du, S. A. Akbar, A. Soliman, and P. K. Dutta, "Microporous zeolite modified yttria stabilized zirconia (YSZ) sensors for nitric oxide (NO) determination in harsh environments," *Sensors and Actuators B: Chemical,* vol. 82, pp. 142-149, 2002.

[187] R. Holland, "Representation of dielectric, elastic, and piezoelectric losses by complex coefficients," *IEEE transactions on Sonics and Ultrasonics,* vol. 14, pp. 18-20, 1967.

[188] J. Smits, "Iterative method for accurate determination of the real and imaginary parts of the materials coefficients of piezoelectric ceramics," *IEEE Transactions on Sonics and Ultrasonics,* vol. 23, pp. 393-401, 1976.

[189] K. W. Kwok, H. L. W. Chan, and C. L. Choy, "Evaluation of the material parameters of piezoelectric materials by various methods," *IEEE transactions on ultrasonics, ferroelectrics, and frequency control,* vol. 44, pp. 733-742, 1997.

[190] X.-H. Du, Q.-M. Wang, and K. Uchino, "An Accurate Method for the Determination of Complex Coefficients of Single Crystal Piezoelectric Resonators II: Design of Measurement and Experiments," *IEEE Trans Ultrason Ferroelectr Freq Control,* vol. 51, pp. 238-248, 2004.

[191] X. Shi, D. Yuan, X. Yin, A. Wei, S. Guo, and F. Yu, "Crystal growth and dielectric, piezoelectric and elastic properties of Ca 3 TaGa 3 Si 2 O 14 single crystal," *Solid State Communications,* vol. 142, pp. 173-176, 2007.

[192] F. Yu, S. Zhang, X. Zhao, D. Yuan, L. Qin, Q.-m. Wang, *et al.*, "Investigation of Ca3TaGa3Si2O14 piezoelectric crystals for high temperature sensors," *Journal of applied physics,* vol. 109, p. 114103, 2011.

[193] J. Yang, H. Xue, H. Fang, Y. Hu, J. Wang, and L. Shen, "Effects of electrodes with varying thickness on energy trapping in thickness-shear quartz resonators," *IEEE Transactions on Ultrasonics, Ferroelectrics and Frequency Control,* vol. 54, pp. 892-895, 2007.

[194] K. Nakamura, "Elastic Wave Energy-Trapping and Its Application to Piezoelectric Devices," *Electronics and Communications in Japan,* vol. 79, pp. 30-39, 1996.

[195] W. Shockley, D. R. Curran, and D. J. Koneval, "ENERGY TRAPPING AND RELATED STUDIES OF MULTIPLE ELECTRODE FILTER CRYSTALS," presented at the 17th Annual Symposium on Frequency Control, 1963.

[196] H. Zu, H. Wu, and Q.-M. Wang, "High-Temperature Piezoelectric Crystals for Acoustic Wave Sensor Applications," *IEEE transactions on ultrasonics, ferroelectrics, and frequency control*, vol. 63, pp. 486-505, 2016.

[197] W. P. Mason, "Zero temperature coefficient quartz crystals for very high temperatures," *The Bell System Technical Journal*, vol. 30, pp. 366-380, 1951.

[198] W. P. Mason, "Low temperature coefficient quartz crystals," *The Bell System Technical Journal*, vol. 19, pp. 74-93, 1940.

[199] H. Shimizu, T. Nishida, H. Takeda, and T. Shiosaki, "Dielectric, elastic and piezoelectric properties of $RCa_4O(BO_3)_3$ (R=rare-earth elements) crystals with monoclinic structure of point group m," *Journal of Crystal Growth*, vol. 311, pp. 916-920, 2009.

[200] H. Takeda, H. Nakao, S. Izukawa, H. Shimizu, T. Nishida, S. Okamura, *et al.*, "Growth and piezoelectric properties of $R_3Ga_5SiO_{14}$ and $RCa_4O(BO_3)_3$ (R: rare-earth elements) single crystals," *Journal of Alloys and Compounds*, vol. 408-412, pp. 474-479, 2006.

[201] F. Yu, S. Hou, S. Zhang, Q. Lu, and X. Zhao, "Electro-elastic properties of YCa4O(BO3)3piezoelectric crystals," *physica status solidi (a)*, vol. 211, pp. 574-579, 2014.

[202] S. Zhang, Y. Fei, B. H. T. Chai, E. Frantz, D. W. Snyder, X. Jiang, *et al.*, "Characterization of piezoelectric single crystal YCa4O(BO3)3 for high temperature applications," *Applied Physics Letters*, vol. 92, p. 202905, 2008.

[203] K. Kim, S. Zhang, W. Huang, F. Yu, and X. Jiang, "YCa4O(BO3)3 (YCOB) high temperature vibration sensor," *Journal of Applied Physics*, vol. 109, p. 126103, 2011.

[204] K. Kim, S. Zhang, G. Salazar, and X. Jiang, "Design, fabrication and characterization of high temperature piezoelectric vibration sensor using YCOB crystals," *Sensors and Actuators A: Physical*, vol. 178, pp. 40-48, 2012.

[205] M. Born, "On the stability of crystal lattices. I," in *Mathematical Proceedings of the Cambridge Philosophical Society*, 1940, pp. 160-172.

[206] M. Born and K. Huang, *Dynamical theory of crystal lattices*: Clarendon press, 1954.

[207] F. I. Fedorov, *Theory of elastic waves in crystals*: Springer Science & Business Media, 2013.

[208] F. Mouhat and F.-X. Coudert, "Necessary and sufficient elastic stability conditions in various crystal systems," *Physical Review B*, vol. 90, p. 224104, 2014.

[209] J. J. McCallum, "Piezoelectric devices for mass and chemical measurements: an update. A review," *Analyst*, vol. 114, pp. 1173-1189, 1989.

[210] Y. Ying and Z. Da-Zhong, "AY type SAW mass sensor with metal array reflectors," *Sensors and Actuators B: Chemical,* vol. 109, pp. 244-248, 2005.

[211] R.-C. Lin, Y.-C. Chen, W.-T. Chang, C.-C. Cheng, and K.-S. Kao, "Highly sensitive mass sensor using film bulk acoustic resonator," *Sensors and Actuators A: Physical,* vol. 147, pp. 425-429, 2008.

[212] M. Voinova, M. Jonson, and B. Kasemo, "'Missing mass' effect in biosensor's QCM applications," *Biosensors and Bioelectronics,* vol. 17, pp. 835-841, 2002.

[213] M. Rodahl, F. Höök, A. Krozer, P. Brzezinski, and B. Kasemo, "Quartz crystal microbalance setup for frequency and Q‐factor measurements in gaseous and liquid environments," *Review of Scientific Instruments,* vol. 66, pp. 3924-3930, 1995.

[214] D. A. Buttry and M. D. Ward, "Measurement of interfacial processes at electrode surfaces with the electrochemical quartz crystal microbalance," *Chemical Reviews,* vol. 92, pp. 1355-1379, 1992.

[215] A. Coats and J. Redfern, "Thermogravimetric analysis. A review," *Analyst,* vol. 88, pp. 906-924, 1963.

[216] E. Tang, G. Cheng, and X. Ma, "Preparation of nano-ZnO/PMMA composite particles via grafting of the copolymer onto the surface of zinc oxide nanoparticles," *Powder Technology,* vol. 161, pp. 209-214, 2006.

[217] D. Bom, R. Andrews, D. Jacques, J. Anthony, B. Chen, M. S. Meier, *et al.*, "Thermogravimetric analysis of the oxidation of multiwalled carbon nanotubes: evidence for the role of defect sites in carbon nanotube chemistry," *Nano Letters,* vol. 2, pp. 615-619, 2002.

[218] E. Mansfield, A. Kar, T. P. Quinn, and S. A. Hooker, "Quartz crystal microbalances for microscale thermogravimetric analysis," *Analytical chemistry,* vol. 82, pp. 9977-9982, 2010.

[219] D. Ballantine Jr, R. M. White, S. J. Martin, A. J. Ricco, E. Zellers, G. Frye, *et al.*, *Acoustic wave sensors: theory, design and physico-chemical applications*: Academic press, 1996.

[220] J. Gagnepain and R. Besson, "Nonlinear effects in piezoelectric quartz crystals," *Physical Acoustics,* vol. 11, pp. 245-288, 1975.

[221] S. Li, W. Cao, and L. Cross, "The extrinsic nature of nonlinear behavior observed in lead zirconate titanate ferroelectric ceramic," *Journal of applied physics,* vol. 69, pp. 7219-7224, 1991.

[222] D. Hall, "Review nonlinearity in piezoelectric ceramics," *Journal of materials science,* vol. 36, pp. 4575-4601, 2001.

[223] W. Ren, S.-F. Liu, and B. K. Mukherjee, "Nonlinear behavior of piezoelectric lead zinc niobate–lead titanate single crystals under ac electric fields and dc bias," *Applied physics letters,* vol. 83, pp. 5268-5270, 2003.

[224] W. Ren, A. Masys, G. Yang, and B. Mukherjee, "Nonlinear strain and DC bias induced piezoelectric behaviour of electrostrictive lead magnesium niobate-lead titanate ceramics under high electric fields," *Journal of Physics D: Applied Physics,* vol. 35, p. 1550, 2002.

[225] Q.-M. Wang, T. Zhang, Q. Chen, and X.-H. Du, "Effect of DC bias field on the complex materials coefficients of piezoelectric resonators," *Sensors and Actuators A: Physical,* vol. 109, pp. 149-155, 2003.

[226] V. Bottom, "Note on the anomalous thermal effect in quartz oscillator plates," vol. 32, ed: MINERALOGICAL SOC AMER 1015 EIGHTEENTH ST, NW SUITE 601, WASHINGTON, DC 20036, 1947, pp. 590-591.

[227] V. E. Bottom, "Final report," Contract DA-36-39-SC-5485, Feb. 29 1952.

[228] A. Ballato, "Effects of initial stress on quartz plates vibrating in thickness modes," in *14th Annual Symposium on Frequency Control. 1960*, 1960, pp. 89-114.

[229] A. Ballato and R. Bechmann, "Effect of initial stress in vibrating quartz plates," *PROCEEDINGS OF THE INSTITUTE OF RADIO ENGINEERS,* vol. 48, pp. 261-262, 1960.

[230] C. R. Mingins, "Report No. 17," Contract DA-28-043, AMC-01240(E), July 1965.

[231] J. M. Ratajski, "The force sensitivity of AT-cut quartz crystals," in *20th Annual Symposium on Frequency Control. 1966*, 1966, pp. 33-49.

[232] J. Ratajski, "Force-frequency coefficient of singly rotated vibrating quartz crystals," *IBM Journal of Research and Development,* vol. 12, pp. 92-99, 1968.

[233] W. Miller, "Experimental Feasibility Study of an Analog Electrical-to-Fluidic Transducer," *IEEE Transactions on Industrial Electronics and Control Instrumentation,* pp. 50-58, 1969.

[234] H. E. Karrer and J. Leach, "A quartz resonator pressure transducer," *IEEE Transactions on Industrial Electronics and Control Instrumentation,* pp. 44-50, 1969.

[235] Y.-G. Dong, J.-S. Wang, G.-P. Feng, and X.-H. Wang, "Self-temperature-testing of the quartz resonant force sensor," *IEEE Transactions on Instrumentation and Measurement,* vol. 48, pp. 1038-1040, 1999.

[236] M. S. Patel and B. K. Sinha, "Force-frequency effect on the Q-factor of thickness-shear mode quartz and Langasite resonator at high temperatures," in *Ultrasonics Symposium (IUS), 2011 IEEE International*, 2011, pp. 316-319.

[237] J. Chen, Y.-k. Yong, R. Kubena, D. Kirby, and D. Chang, "On the acceleration sensitivity and its active reduction by edge electrodes in at-cut Quartz resonators," *IEEE transactions on ultrasonics, ferroelectrics, and frequency control,* vol. 62, pp. 1104-1113, 2015.

[238] H. Zhang, J. A. Turner, and J. A. Kosinski, "Experimental measurements of the force-frequency effect of thickness-mode langasite resonators," *IEEE transactions on ultrasonics, ferroelectrics, and frequency control,* vol. 60, pp. 1475-1478, 2013.

[239] Y. Kim and A. Ballato, "Force-frequency effect of Y-cut langanite and Y-cut langatate," *IEEE transactions on ultrasonics, ferroelectrics, and frequency control,* vol. 50, pp. 1678-1682, 2003.

[240] Q. M. Zhang and J. Zhao, "Electromechanical properties of lead zirconate titanate piezoceramics under the influence of mechanical stresses," *IEEE transactions on ultrasonics, ferroelectrics, and frequency control,* vol. 46, pp. 1518-1526, 1999.

[241] P. Lee, Y. Wang, and X. Markenscoff, "High− frequency vibrations of crystal plates under initial stresses," *The Journal of the Acoustical Society of America,* vol. 57, pp. 95-105, 1975.

[242] A. Green, R. Rivlin, and R. Shield, "General theory of small elastic deformations superposed on finite elastic deformations," in *Proceedings of the Royal Society of London A: Mathematical, Physical and Engineering Sciences*, 1952, pp. 128-154.

[243] M. A. Biot and J. E. Romain, "Mechanics of incremental deformations: Theory of elasticity and viscoelasticity of initially stressed solids and fluids," ed: AIP, 1965.

[244] M. Hayes and R. S. Rivlin, "Surface waves in deformed elastic materials," *Archive for Rational Mechanics and Analysis,* vol. 8, pp. 358-380, 1961.

[245] R. Thurston and K. Brugger, "Third-order elastic constants and the velocity of small amplitude elastic waves in homogeneously stressed media," *Physical Review,* vol. 133, p. A1604, 1964.

[246] P. Lee, Y. Wang, and X. Markenscoff, "Nonlinear effects of initial bending on the vibrations of crystal plates," *The Journal of the Acoustical Society of America,* vol. 59, pp. 90-96, 1976.

[247] P. Lee and Y. Yong, "Temperature derivatives of elastic stiffness derived from the frequency‐temperature behavior of quartz plates," *Journal of Applied Physics,* vol. 56, pp. 1514-1521, 1984.

[248] P. Lee and K. M. Wu, "In‐plane accelerations and forces on frequency changes in doubly rotated quartz plates," *The Journal of the Acoustical Society of America,* vol. 75, pp. 1105-1117, 1984.